UNIVERSITA' DEGLI STUDI DI CAGLIARI

DOTTORATO DI RICERCA IN FISICA

FIS/03 FISICA DELLA MATERIA

XXVI CICLO

Ultrafast Optical Spectroscopy Techniques applied to colloidal nanocrystals.

Supervisor: PhD Student:

Dr. Michele Saba   Aresti Mauro

Anno accademico:

2012-2013

Contents

I

Introduction

In this thesis I will describe my experimental work based on ultrafast optical spectroscopy techniques applied to colloidal nanocrystals.

Colloidal semiconductor nanocrystals in recent years have attracted a lot of attention in particular in optoelectronic applications, because they present unique optical, electronic and charge carrier transport properties that can be easily modified via colloidal chemical synthesis.

In the first chapter of this thesis, I will introduce the basic concepts of nanocrystals and their optical properties, I will consider some simple models to explain the physical properties of semiconductor nanocrystals. I will briefly describe the colloidal chemical synthesis of these nanocrystals and how we can change the optical properties by simply acting on the colloidal chemical synthesis.

In the second chapter I will describe the basic concepts of ultra fast optical spectroscopy techniques used in my experimental work. I will describe the basic principles and the experimental set-up of the two main techniques that I used: time-resolved photoluminescence spectroscopy (TR-PL) and transient absorption spectroscopy or also called *Pump Probe*. These two techniques allow to investigate in a very precise way the main optical properties and

dynamics of charge carriers in nanocrystals.

In the third chapter I will describe my experimental work based on time-resolved photoluminescence spectroscopy applied to $CdSe/CdS$ $core/shell$ nanocrystals. These nanocrystals are a reference nanocrystals and their optical properties are extensively investigated, however, some aspects are not fully understood, for example, the instability or blinking of the light emission under constant illumination in these nanocrystals is still an unsolved problem that limits the real applications. The particular spectroscopic technique that I have used $variable$ $pulse$ $rate$ $photoluminescence$ $spectroscopy$ revealed the causes of this issue, and will give us a solution to resolve it.

In the fourth chapter I will discuss novel nanostructures of $CdSe/CdS$ multi branched shape, in this case $octapod$ shaped nanocrystals consist of eight arms made of CdS grown on a CdSe core, these present a large cross-section for light absorption and efficient charge separation ideally suited for applications of photocatalysis. The optical spectroscopy technique used to investigate the properties of these nanocrystals are the $transient$ $absorption$ $spectroscopy.$

In the fifth chapter I will discuss experimental work on Bi_2S_3 semiconductor nanocrystals and I will describe related optical techniques used to study the optical and electronic properties. This nanocrystal has excellent properties of optical absorption of solar radiation and can be used for the realization of solar cells. Another important property of Bi_2S_3 is its non-toxicity that will allow in the future to achieve efficient solar cells and easy disposal and simultaneously not damaging to the environment.

Chapter 1

Colloidal Nanocrystals

Colloidal semiconductor nanocrystals can be the material of choice for a wide variety of optical applications because their tunable properties, such as optical absorption and emission, size and shape, and charge carrier transport. Nanocrystals can be used as light absorbers and emitters in optoelectronic devices such as light emitting diodes, photodetectors, solar cells and other similar optoelectronics devices.

1.1   Semiconductor Nanocrystals

A semiconductor nanocrystal is a single crystalline entity constituted by a given number of atoms, a particular geometric shape and size and a specific crystallographic structure, these properties are dependent on physical and chemical conditions present during the process of crystal growth.

Nanocrystals generally show properties that differ from bulk material properties. The correlation between properties and particle size has been

known since the nineteenth century when M. Faraday demonstrate that the color of colloidal gold particles can be modified and proposed that the effect was related to particle size [1]; however, an effective control over synthesis and properties was achieved only in the last two decades of twentieth century. In a bulk of semiconductor the energy band gap between the valence band
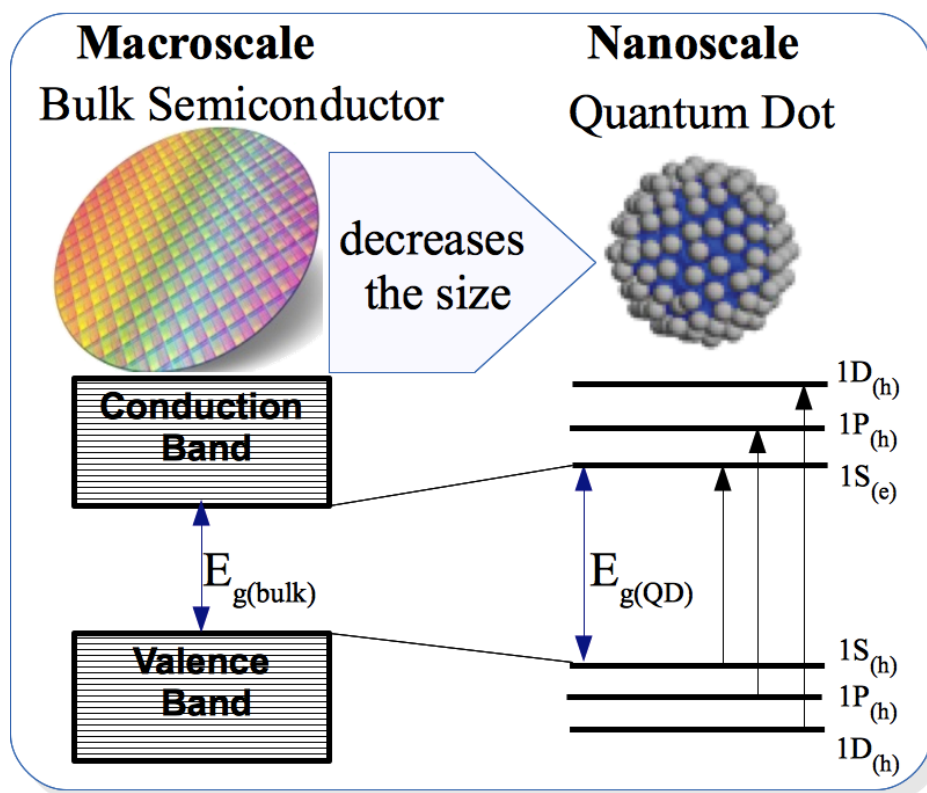
Figure 1.1: *Nanocrystals: from macroscale to nanoscale. Electronic energy levels for a bulk of semiconductor and a quantum dot of the same material.*

and conduction band are intrinsic physical property that depends solely on the type of semiconductor. But more than twenty years ago it has been understood that if we pass from macroscale to nanoscale dimensions the

energy band gap is no longer a fixed parameter which depends only on the material. The property of a material is usually substantially modified in 1-10nm size. If we consider a semiconductor particle with size of about $\sim 10\ nm$ which corresponds to about $\sim 10^4$ atoms, electronic excitations are affected by the boundary conditions, that is we are in a state of quantum confinement. In these conditions the particle size directly affects the energy of band gap. This phenomenon is known as *quantum size effect* and the particles that are affected are called *Quantum Dots* or *QD* briefly. Reducing the size of the particles we obtain that the energy band gap increases and consequently also change the optical and electronic properties of the nanocrystals.

Now if we imagine to be able to fine tune the size of these particles, we could control the optical and electronic properties of these nanocrystals in according to our needs, this control would mean a big advantage in opto-electronics applications. The size of the particles can be easily controlled by means colloidal chemical synthesis.

1.1.1   A simple model, quantum box.

The phenomenon of quantum size effect can be explained by a simple quantum model: the quantum box, in fact, if we imagine a particle enclosed in a three-dimensional potential well, performing the calculations we find that energy of the particle depends on the size of the potential well. This model can be applied to the quantum dot. If we consider a spherical particle of radius R with reference figure 1.1 the increase of E_g^{QD} with respect to E_g^{bulk}

is given by the equation 1.1.

$$E_g^{QD} \approx E_g^{bulk} + \frac{\hbar^2 \pi^2}{2 m_{eh} R^2} \tag{1.1}$$

Where m_{eh} is the reduced mass of the electron-hole pair in the quantum dot. We can see that the energy depends on the size of the particle as $1/R^2$. In addition to this effect of quantum confinement modifies the energy levels that are continuous in the bulk and become discrete in the QDs (see figure 1.1), making QDs similar to artificial atoms.

1.1.2   Optical properties of the nanocrystals

Semiconductor nanocrystals have different physical characteristics compared to bulk semiconductors. The optical absorption in these QDs reflects the nature of electronic levels.
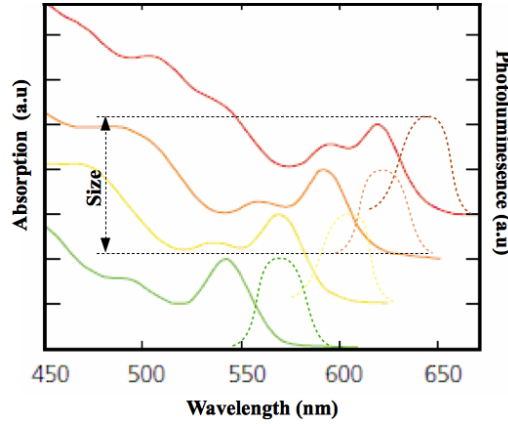
Figure 1.2: *Optical absorption (solid line) and photoluminescence (dashed line) for nanocrystals with four different sizes, the shift in wavelength is correlated with the different size of the nanocrystals.*

In a bulk of semiconductor optical absorption is a phenomenon determined by the energy separation between the valence band and conduction band; but in a nanocrystal semiconductor optical absorption is composed of different peaks corresponding to different energy levels, (S,P,D see fig 1.1) similar to what happens in an atom. These peaks have spread for reasons arising from the dispersion of size in colloidal synthesis procedure and temperature fluctuations. (fig 1.2).

In same way as it happens for the optical absorption also the optical emission is influenced by the size of the nanocrystals, shifting the optical emission toward blue with decreasing particle size, as you can see in the figure 1.3 the radius of the particles ranges from 1.5 nm to 5 nm and consequently the wavelength ranges from blue-green to orange-red.
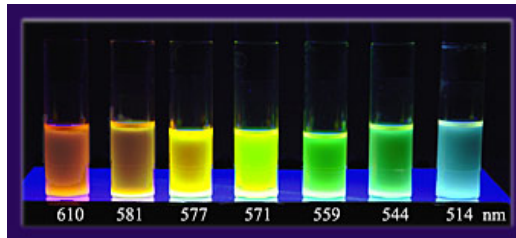
Figure 1.3: *Photoluminescence at different wavelengths resulting from the same material but with different size of the nanocrystals, with decreasing size it has a shift of the photoluminescence on blue.*

In addition, in these nanocrystals excitonic states are statistically favorites with respect to the bulk semiconductor, for example, the excitonic states, ie, electron and hole bound by Coulomb interaction have long lifetimes compared to the same excitonic state in the bulk. The fact that the lifetimes of the excited states are longer can be exploited to achieve an efficient charge

separation, ideal for photovoltaic applications. In these nanostructures, the relationship between volume and surface makes this last very important, in fact, surface phenomena as traps can drastically change the optical characteristics of the QDs, for this reasons the particles are passivated at the time of synthesis colloidal.

The enormous advantage of these nanocrystals is in the fact that we can change in according to our requirements the optical properties of absorption and emission.

1.2   Colloidal Chemical Synthesis

A colloidal solution is a dispersion of small particles in another material called solvent. A colloidal particle may be composed of a large number of atoms or molecules, but the total size does not exceed one hundred nanometers. We can distinguish the colloidal solutions in according to the particle interaction with the solvent into two distinct classes: lyophilic are solvent-attracting and lyophobic are solvent-repelling, if the solvent is water it are called hydrophilic and hydrophobic respectively. If into a colloidal solution each particle repels any other, the repulsive potential energy is predominant, and the colloidal solution appears transparent. From the opposite side if the attractive potential dominates the solution is cloudy with possible deposits. Colloidal solutions are thermodynamically unstable with respect to the bulk semiconductor, for these reasons different thermodynamic states can occur under different conditions of temperature, pressure and other.

Synthesis of colloidal nanocrystals is a complex operation, where the ther-

modynamics plays a fundamental role in the control of geometric shape, size, crystalline structure and surface defects.

To simplify the description of the colloidal synthesis, we can divide the process into five distinct phases [2], with reference to Figure 1.4
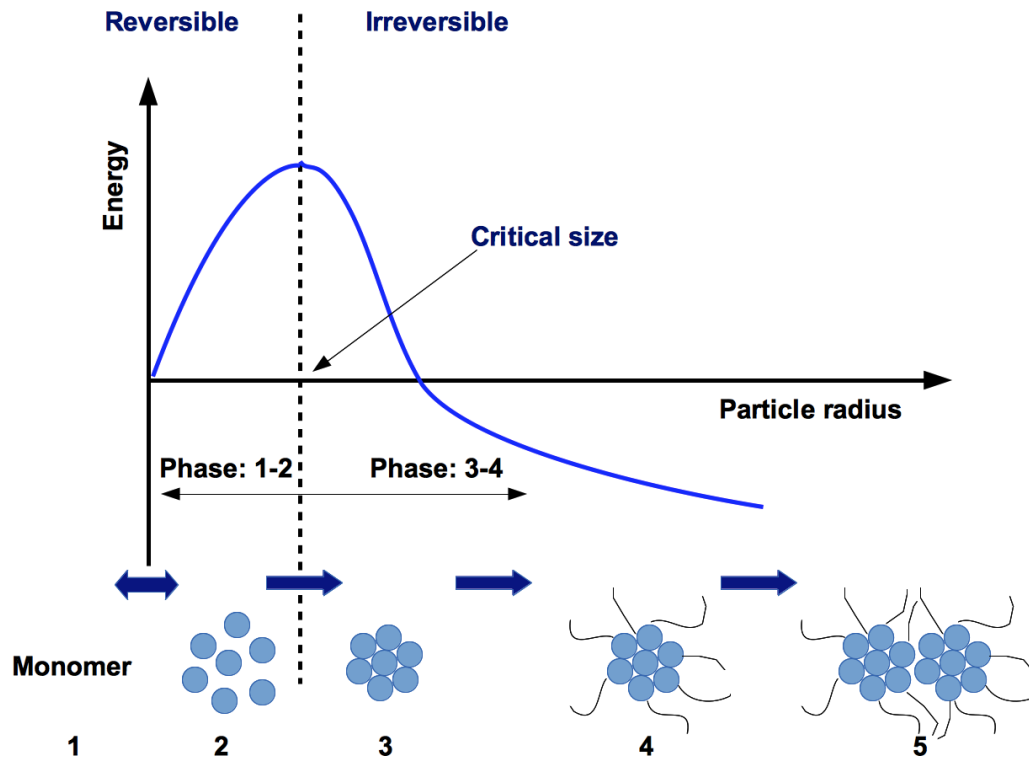
Figure 1.4: *Schematic representation of the nucleation and growth process showing the five steps composing the colloidal synthesis and the dependence of thermodynamic coordinate (energy) with the crystals size. Below the critical radius a reversible process occurs, above this critical radius the process becomes irreversible.*

In the first phase the precursors are injected into a hot coordinating solvent, in this way, the precursors react with each other and are created the monomers, i.e. the smallest entity (minimum cell), which possesses the char-

acteristics of the crystals.

In the second phase with increasing concentration of precursor, the monomers aggregate into clusters. At this stage begins the growth of the monomers, but until the size does not exceed a certain critical value, the process is completely reversible. This phase is called *nucleation*.

In the third phase as the concentration of precursors can exceed the critical size, and therefore the particle becomes thermodynamically stable, from this moment onwards can only grow, In fact the process becomes irreversible. This phase is called *growth*.

In the fourth phase the growth of the nanocrystal can be controlled with the help of stabilizers. In this phase also the geometric shape of growth around the seed can be controlled with stabilizers and solvents, favoring a particular thermodynamic state which facilitates a crystallographic growth rather than another.

In the fifth phase the particles created previously, can interact and create a large agglomerates or disordered assemblages of nanoparticles that possess an different crystal planes.

The ideal process would be to have all the phases separate and distinct, but unfortunately it does not happen, in reality the five stages are not distinct but overlapping; this is the main problem encountered in this colloidal synthesis. If the process of nucleation and growth were separated, the control of the size and the geometric shape would be more simple, in fact in the nucleation step we can control the number of particles that will be created and in the stage of growth we can control the shape and the size. But if these two phases have overlapped is difficult to control the concentration and size,

by this issue will result in a dispersion of the size of the nanoparticles.

The major efforts to improve the colloidal synthesis techniques trying to keep separate the two phases in order to have more control over the quality of the nanocrystals.

Chapter 2

Ultrafast Optical Spectroscopy Techniques

Ultra fast optical spectroscopy is an important tool of investigation of the optical and electronic properties of matter. With these techniques we can study optical and electronic phenomena that occur in a time frame of the order of hundreds of femtoseconds, that is, we can investigate very fast energy relaxation and charge transfer processes.

2.1 Ultrafast Optical Spectroscopy Technique

The common element among techniques of ultrafast optical spectroscopy is the source of light excitation. The excitation source has the task of supplying the energy to the system under study, so as to bring it from a electronic ground state to an excited state. After the system relaxes by emitting light radiation that will be detected by appropriate measuring instruments. To

study phenomena very fast whose order of magnitude is hundreds of femtoseconds, the excitation source must be a pulsed laser with a pulse width of the same order of magnitude of the phenomenon under study.

The laser source for the time-resolved photoluminescence setup was a Ti:Sapphire passively mode-locked femtosecond laser (Spectra Physics Tsunami, pumped by a diode-pumped, frequency-doubled Nd:YAG laser, Spectra Physics Millennia), emitting at 780 nm in wavelength, with a 80 MHz repetition rate and 100 fs pulse duration.

The laser source employed for transient absorption spectroscopy setup was a Ti:Sapphire regenerative amplifier (Quantronix Integra C) operating at a repetition rate of 1 kHz and emitting at 786 nm in wavelength with 150 fs in duration.

In the following two paragraphs describes two techniques of ultrafast spectroscopy used in this thesis work.

2.2   Time Resolved Photoluminescence spectroscopy

This technique uses a pulsed laser source to promote electrons from the ground state to an excited state. Immediately after the absorption of the laser pulse the system is in an excited state, after the system relaxes emitting optical radiation or photoluminescence. The photoluminescence signal provides a lot of information on the electronic and optical properties of the nanocrystal.

Part of the information is derived from the spectral analysis, the wavelength of optical emission is correlated with band gap and consequently with

the size of the nanocrystal also we can investigate the different excitonic states and trap states which correspond to significant shifts in wavelength.

Another part of the information is derived from the temporal analysis of the photoluminescence, in fact, the decay time of the light signal is different for different excitonic states and trap states, so we can investigate the dynamics of the charges processes.

2.2.1   The experimental setup

A train of laser pulses from laser source is sent by means of an optical system that allows an appropriate focussing on the sample in the study. Each pulse is absorbed in a very short time and provides energy and creates an excited state in the sample. Photoluminescence emitted by the sample between one pulse and the next is collected by an appropriate optical configuration and acquired by the detection system. The detection system is composed of a spectrometer coupled with a streak camera. The spectrometer spectrally resolves the optical signal while the streak camera temporally resolves the optical signal. As a final result is obtained a spectrogram with the spectral and temporal properties of nanocrystals under study.
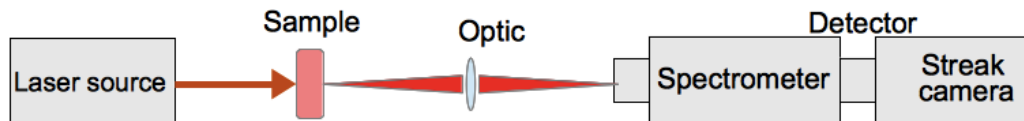
Figure 2.1: *Time resolved photoluminescence spectroscopy technique. Sketch of experimental setup.*

The experimental setup is shown schematically in figure 2.1

2.2.2   The Streak Camera

The Streak Camera [1] is a special detector that allows to resolve spatially and temporally an optical signal, figure 2.2 shows the operating principle. Let us consider a generic optical signal consisting of four optical pulses which vary slightly in terms of both time and space, and which have different optical intensities, are input through the slit, are focused and arrive at the photocathode. In photocathode optical pulses are converted by photoelec-
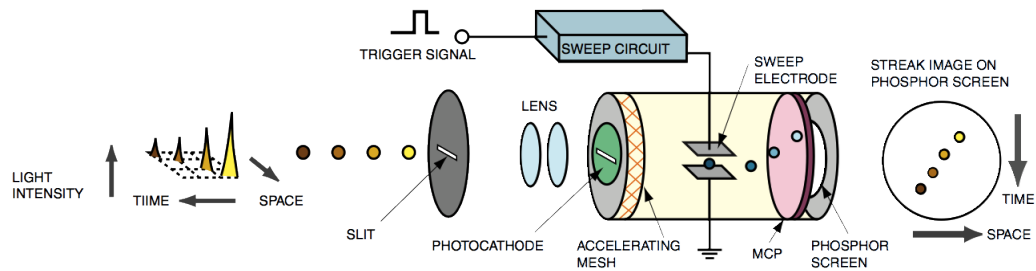
Figure 2.2: *Operating Principle of the Streak Tube. This image comes from the user's guide to streak camera produced by Hamamatsu.*

tric effect in a number of electrons proportional to the intensity of the optical pulse, following the electrons are accelerated towards a two sweep electrodes. Electrons pass between two sweep electrodes, high voltage is applied to these electrodes in synchronism with the optical signal, in the figure 2.3 is shown a diagram of the scanning of the voltage on the sweep electrodes. Electrons that arrive with different times are deflected vertically in a different way, in this way signals are temporally resolved.

---

[1]for more information see: `http://www.hamamatsu.com/resources/pdf/sys/e_streakh.pdf`
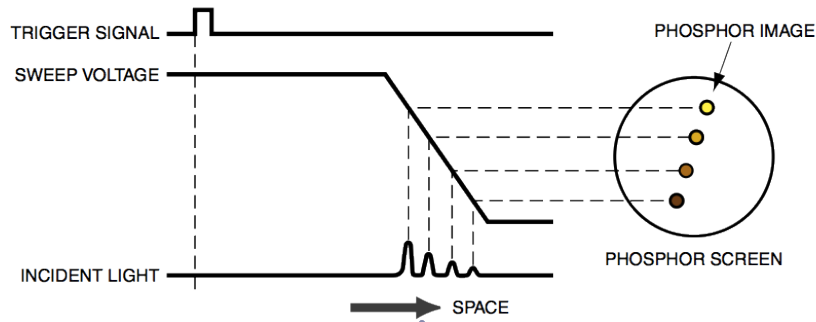
Figure 2.3: *Operation Timing at time of sweep voltage. This image comes from the user's guide to streak camera produced by Hamamatsu inc.*

Finally, electrons enter the micro-channel plate (MCP). Inside the MCP the electrons are multiplied several thousands of times, after which they impact against the phosphor screen, where they are converted again into light signal.

The image that is formed on the phosphor screen corresponds to light signal in input resolved both temporally and spatially, the intensity of each signal is proportional to the image brightness. The position in the horizontal direction of the phosphor image corresponds to the horizontal location of the incident light and the vertical direction on the phosphor screen serves as the time axis. A CCD camera allows to display and store the image of the phosphor screen. In this way, the streak camera can be used to convert changes in the temporal and spatial light intensity of the light being measured into an image showing the brightness distribution on CCD camera.

2.3   Transient Absorption Spectroscopy

Transient absorption spectroscopy is a technique of nonlinear ultrafast optical spectroscopy that can measure the changes in optical transmission in an excited sample arising from changes in the electronic population of the excited levels. In fact, while the sample relaxes energetically the absorption of photons is closely related to the number of occupied levels. This technique allows to investigate the change in the number of levels accessible to the system over time.

This technique typically uses two different laser pulses, the first called *pump* brings the sample in an excited state, the second is called *probe* because it measuring its transmittance through the sample at different time delays. From this comes the name of the pump-probe technique.

The transmission spectrum of the probe pulse at different delay times describes the dynamics of emptying of electronic levels and eventually of trap levels if present.

2.3.1   Principle of operation

The figure 2.4 shows the scheme of electronic levels for a generic semiconductor. In this technique we measure the differential transmission $\Delta T = T_{on} - T_{off}$ of the probe through the sample, where T_{on} (pump on) is the transmitted light in presence of the pump laser and T_{off} (pump off) is the transmitted light in absence of the pump laser. Actually we measure relative differential transmission that is:

$$\frac{\Delta T}{T} = \frac{T_{on} - T_{off}}{T_{off}} \approx \Delta A$$

where A is the transient absorption. The pump laser pulse promotes electrons
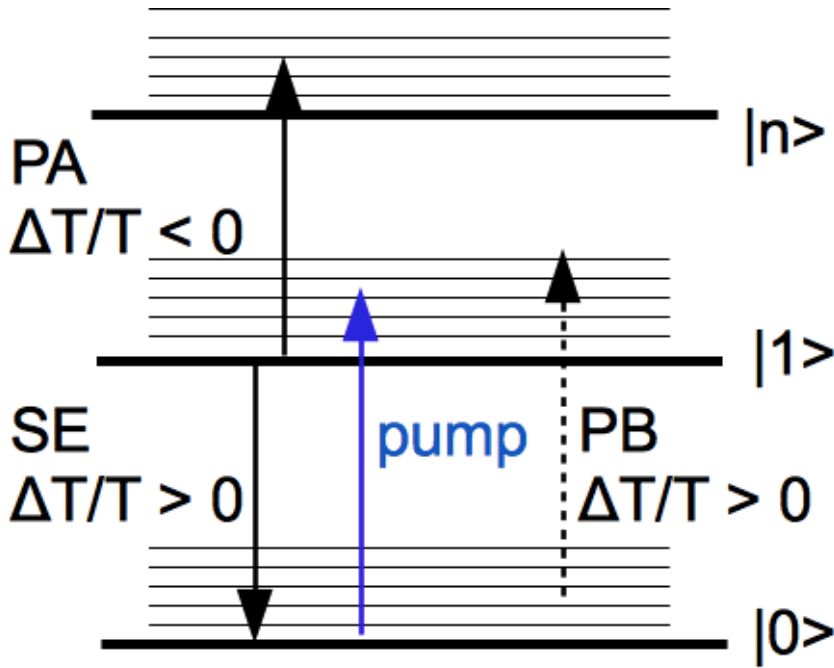
Figure 2.4: *Transient absorption spectroscopy: principle of operation and electronic levels.*

from the ground state to an excited level. Now if at a given time after the absorption of the pump pulse, we measure the transmission of the probe can be occur different situations depending on the population of the energy levels.

If the probe pulse is absorbed, means that there are free electronic levels then occur a photo absorption (PA), that is the transmission of the probe pulse decreases. In the opposite way if the probe pulse is not absorbed means that there are no free electronic levels, it has photo bleaching (PB) or in other words the transmission of the pulse probe increases. The transmission of the probe can also increase with the phenomenon of stimulated emission (SE),

where a photon with the correct wavelength can trigger emission of another photon from an excited state. By analysis of the transmission spectra we can understand the dynamics of depletion of energy levels and their live-time.

2.3.2   The experimental setup

The figure 2.5 shows the experimental setup. A train of pulses from the laser source Ti:Sapphire is divided into two parts by a beam splitter, the two beams are called respectively pump and probe. The pump laser pulse is
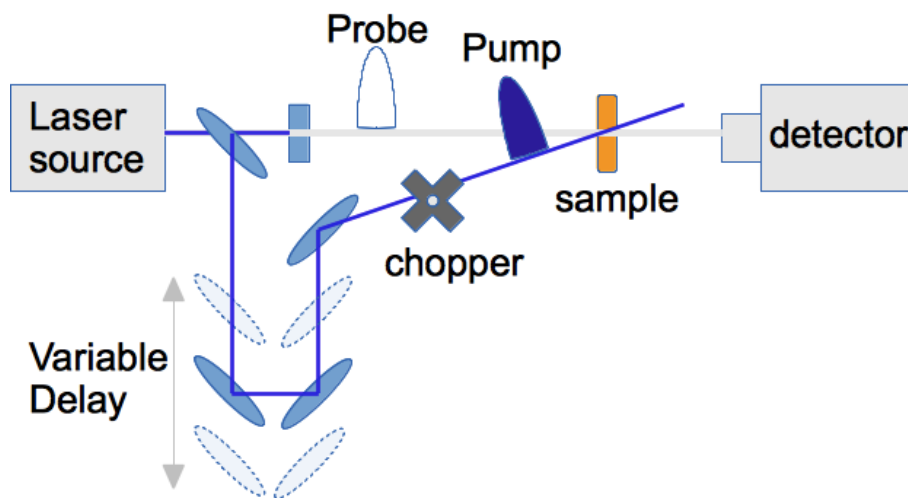
Figure 2.5: *Transient absorption spectroscopy technique: sketch of experimental setup.*

sent on a delay line and then focused on the sample. In this route the pulse passes through a chopper that is synchronized to the frequency of the pulsed laser source. The task of the chopper is to block half of the incident pulses alternatively, this is done by setting the chopper frequency equal to half of that of the laser source. In this way, half of the spectra obtained will not

be affected by the pump pulse (pump off), while the remaining half will be affected (pump on).

The task of the pump pulse is to excite the sample, therefore the angle of incidence is put out of the line of collecting of probe. The probe pulse can be of the same wavelength of the probe pulse or different, this in according to the experimental requirements, in this case we speak of a single color pump probe. The probe pulse may be constituted by a white-light continuum (range 450-700 nm in spectrum), generated by focusing the output of laser source in a sapphire plate, in this case we speak of white supercontinuum pump probe.

The probe pulse is sent and focused on the sample, spatially overlapped with pump pulse, the probe pulse after having interacted with the sample is collected into the detection system. The acquisition system is constituted by a spectrometer coupled to a CCD camera that allows the acquisition and recording of spectra accumulated.

For every single step of the delay line are acquired the differential transmission spectrum of the signal probe, which contains the spectral information for a given time delay. Building a spectrogram combining all spectrograms for each time steps of the delay line, we can derive the information on the temporal dynamics of the depletion of energy levels.

Chapter 3

CdSe/CdS core/shell nanocrystals

Colloidal semiconductor nanocrystals in recent years have attracted a considerable interest in photonic applications, due to their easy synthesis and their tunable optical gaps. In particular $CdSe/CdS$ core/shell nanocrystals have become a nanocrystals of reference, because they have been extensively studied and are known for high luminescence quantum yield and reduced blinking. In addition these nanocrystals can be synthesized with good reproducibility. Just because the basic photophysics of these nanocrystals is well understood, these are suitable for advanced studies of photophysics. In this chapter I will describe the experimental procedure to study the causes of instability of optical emission in these nanocrystals.

The work presented in this chapter has been published in the journal *ACS Nano* with the title: *Light-Induced Charged and Trap States in Colloidal Nanocrystals Detected by Variable Pulse Rate Photoluminescence Spectroscopy.* [3]

23

3.1   CdSe/CdS core/shell nanocrystals

CdSe/CdS core/shell nanocrystals have been prepared by seeded growth, starting from $3.6nm$ $CdSe$ cores, then covered with a CdS shell up to a total size of $8 - 10nm$. [4,5]
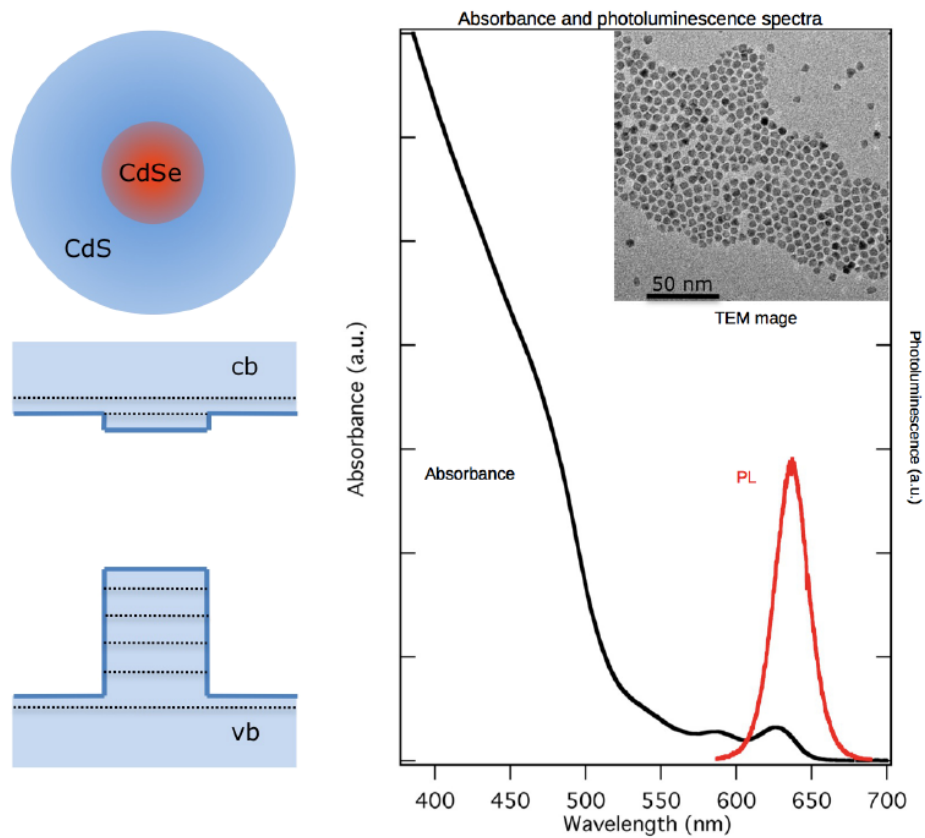
Figure 3.1: *Right: sketch of the CdSe/CdS nanocrystal composition and energy levels. Left: absorbance (black line) and photoluminescence (red line) spectra of nanocrystals. Inset: TEM image of nanocrystals.*

The nanocrystals, dispersed in toluene after purification and centrifu-

gation, are capped by a combination of stabilizing agents employed during growth, that is, trioctylphosphine oxide (TOPO), trioctylphosphine (TOP), and hexadecylamine (HDA), in figure 3.1 is shown a sketch of the nanocrystals and TEM image of nanoparticles. In the same figure 3.1 are shown absorbance and photoluminescence (PL) spectra of nanocrystals dispersed in toluene. Absorption spectra were acquired with a Perkin Elmer Lambda 950
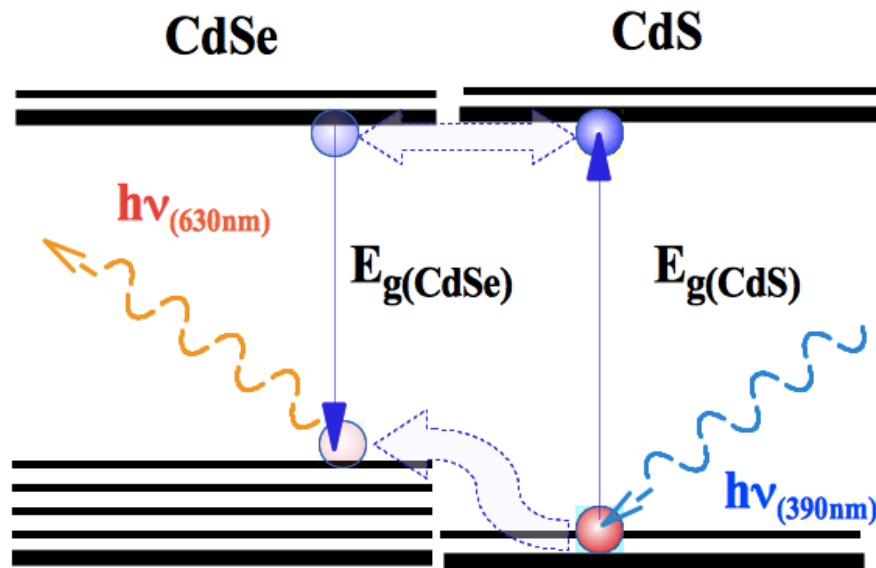
Figure 3.2: *Scheme of electronic alignment of CdSe/CdS core/shell nanocrystals, absorption and emission mechanism.*

spectrophotometer, all spectra were recorded on toluene-based suspensions in quartz cuvette with optical density less than 0.3, this condition ensures that absorption is not in saturation. The photoluminescence spectrum is centered around 630 nm in wavelength, corresponding to emission from the CdSe core, meaning that even though the optical absorption occurs mostly in the CdS shell, optical excitations relax to the lowest-energy states in the core before

emitting. Referring to Figure 3.2, exciting the nanocrystal with the second harmonic of laser source ($390nm$) we can provide enough energy to remove the electron from the valence band to the conduction band of CdS (shell), where the band gap is $E_{g(CdS)} = 2.42eV$ [6]. The alignment of the bands is such that electrons are delocalized throughout the whole nanocrystal, while the holes diffuse and remain localized in the core of CdSe, therefore, recombination occurs more likely in CdSe (emitting at $630nm$), where the band gap is large only $E_{g(CdSe)} = 1.74eV$ [6].

This mechanism of recombination between electrons and holes can be reduced or rendered slower if there are traps for electrons or holes. The study of photophysics in these nanocrystals is focused on understanding the mechanisms that turn on-off the photoluminescence emission (this phenomenon is also known as blinking), because the major applications in optoelectronics require high photo-conversion efficiencies in conditions of high rate operation.

3.2 Intensity instabilities under steady-state operation.

The optimal operating condition for many photonic applications is the single-excitation regime, with less than one excited electron-hole pair per nanocrystal at any given time, but a large repetition rate of emission events, possibly approaching the steady-state limit. [7–10] The fact that under steady-state operation the intensity of the light emitted from these nanocrystals tends to be unstable and randomly blinking over time, is a problem which limits its use in the larger part of the photonics applications.

This phenomenon has been observed for many years in molecular systems and nanostructures. [11–21] To overcome this problem it is necessary design nanostructures capable of emitting light with high efficiency and stability under working conditions. More stable emission has been recently achieved by a proper design of the overcoating inorganic shells in colloidal quantum dots [20–25]. The origin of the emission instabilities is still controversial in prototype nanostructured materials, such as colloidal quantum dots, and is currently subject of debate in the scientific community. A large part of the existing literature assumes that fluorescence intermittency is caused by charging and discharging of nanocrystals [21–23, 26–36], based on the well established experimental evidence that charged quantum dots are weak emitters owing to fast nonradiative Auger recombination of excitons [7–10,37]. Recent experimental results and new theoretical models indicate, however, that fluorescence intermittency may have a different origin, triggered by random activation of nonradiative exciton traps at the nanocrystal surface. [11–20,38–50] Whether or not these emission instabilities can be indirectly induced, or influenced by light, as recently suggested is still an open question. [9,20–25,43,51]

3.3 Variable pulse rate photoluminescence spectroscopy.

The experiment is designed to identify the fundamental mechanism of photoluminescence quenching, based on transient nonlinear photoluminescence spectroscopy applied to an ensemble of nanocrystal quantum dots. This spectroscopic tool represents a variation on the well-established approach to

the dynamics of multiple electron-hole pairs in the regime of high fluence excitation. [21–24, 27–36, 52].

The technique is developed to investigate basic emission quenching processes appearing at injection levels below one electron-hole pair per nanocrystal per excitation pulse. The key idea is to control the repetition rate and energy of the excitation laser pulses to induce the pile-up of long-lived, non-radiative states surviving in quantum dots from one pulse to the next one. Light-induced quenching processes are then monitored through detection of nonlinear transient photoluminescence. While the technique accesses a long-
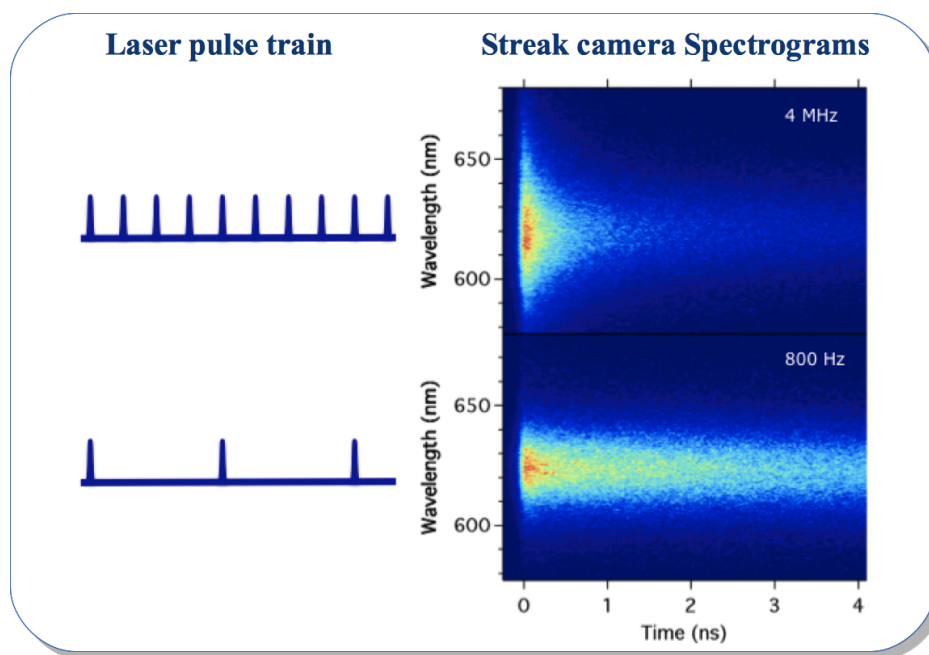

Figure 3.3: *Variable pulse rate photoluminescence spectroscopy, two spectrograms acquired under different conditions show the potential of the technique.*

lived state, a major advantage of variable repetition rate photoluminescence

is to retain the full picosecond temporal resolution of ultrafast photolumi-
nescence necessary to detect directly quenching phenomena. Variable pulse
rate photoluminescence spectroscopy is applied here to CdSe/CdS core/shell
nanocrystals, in order to control and investigate dark and weakly emitting
states in a model system, known for high luminescence quantum yield and
reduced blinking.

Figure 3.3 illustrates the potential of nonlinear photoluminescence spec-
troscopy to investigate emission quenching and to distin guish light emission
from neutral, positively, and negatively charged quantum dots. The two dif-
ferent spectrograms in the figure were taken on a nanocrystal film excited
with the same laser pulse energy (corresponding to an average number of
excitations per nanocrystal N = 0.16), but with two very different pulse
repetition rates (4 MHz and 800 Hz): while low repetition pulse train gener-
ated only exciton states, high repetition pulses caused pile-up of long-lived
charge-separated states, resulting in faster decaying emission from trions and
a wider photoluminescence spectrum.

This technique is capable to distinguish between contributions to the
emission dynamics due to excitons created in nanocrystals with charged cores
from those with active charge traps. We identify the spectroscopic features
of both negative and positive trions, their characteristic relaxation times,
and the photoinduced trapping kinetics of neutral excitons. We observe
that accumulation of charges and the population of trap centers saturate for
increasing light intensity in nanocrystal films.

3.3.1   Charged states and traps.

In figure 3.4 are shown the possible excited states contributing to optical emission. Excitons are created in neutral nanocrystals by the absorption of a laser photon, begin to occur even low energy excitations. Increasing the excitation energy and the pulse repetition frequency, the probability of formation of multi-excitonic states increases. Absorption of two photons from the same laser pulse may create a biexciton in the nanocrystal.
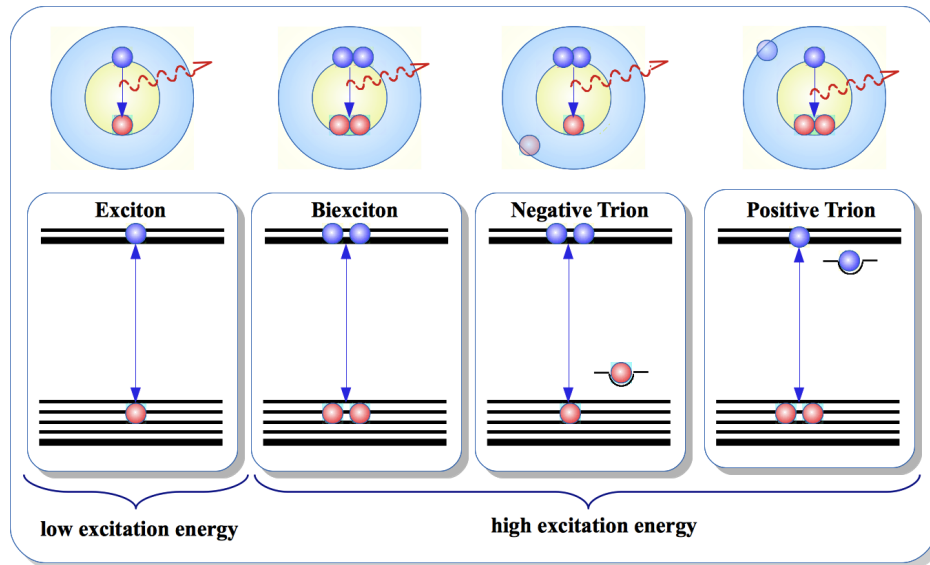
Figure 3.4: *Possible charged states and traps.*

Trions or charged excitons are created by optical absorption in a charged nanocrystal, that is, a nanocrystal left over by previous laser pulses in a long-lived, charge-separated state, with a positive or negative charge inside the core, while the opposite charge is trapped in a state on the surface or outside the nanocrystal.

Multiexciton states with multiplicity larger than two are not included in this analysis because they can be identified by their emission at photon energies substantially larger than the band gap and they decay into band edge states in a very short transient, on the order of 10 ps.

3.4 Expected effects of charged states and traps on photoluminescence.

Expected effects of charged states and traps on photoluminescence time traces are shown in Figure 3.5. In panel 3.5(a) are shown effects of charged

Figure 3.5: *Scheme of expected effects of charged states and traps on photoluminescence temporal traces and spectra.*

excitons, i.e. trions $(X_{-,+})$, cause an enhancement of the initial amplitude of the signal A_0 because of their shorter radiative time with respect to neutral excitons X, owing to the fact that statistics allow twice as many recombination paths for trions than for excitons [53]. Tr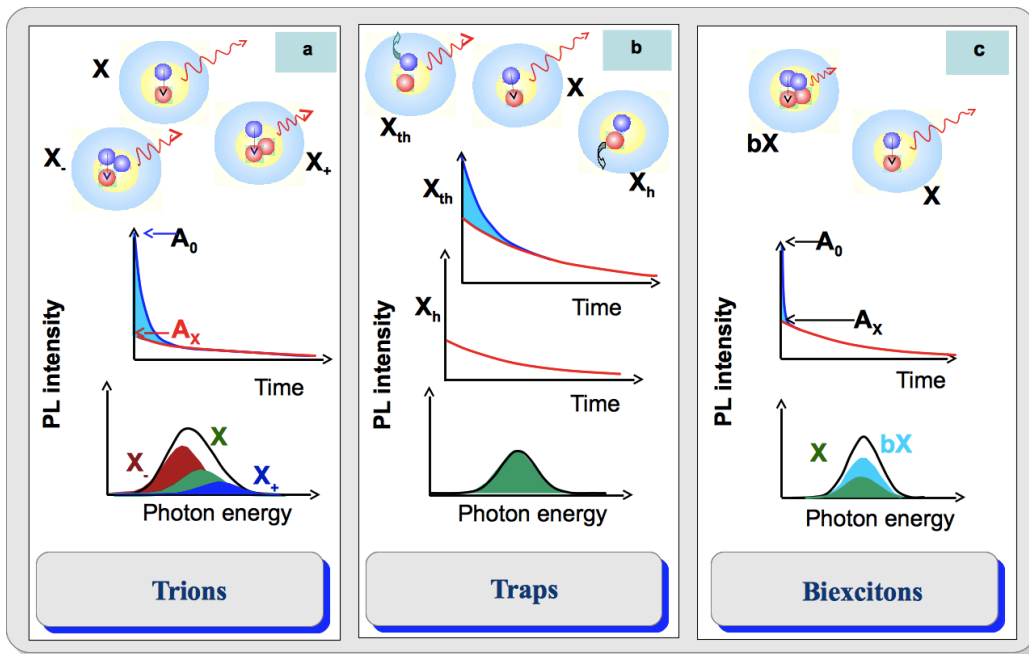ions are also subject to Auger recombination, leaving only the longer-living exciton component after decaying; the emission spectrum of charged and neutral excitons can be distinguished because of the energy shift induced by the exciton-charge interactions.

In panel 3.5(b) are shown effects of traps, activation of traps instead causes no enhancement of the initial photoluminescence amplitude A_0; thermal traps X_{th} capture excitons already relaxed to the band edge and therefore shorten the initial photoluminescence decay; hot traps X_h capture the exciton before they relax to the band edge and have the only effect of reducing the overall photoluminescence signal, while they leave the dynamics unaltered; as traps subtract excitons and do not emit light themselves, their presence cannot be inferred from the photoluminescence spectrum.

In panel 3.5(c) are shown effects of biexcitons bX, such a state has a 4 times larger radiative recombination rate with respect to excitons and therefore produces a larger initial photoluminescence amplitude A_0 but is also subject to fast nonradiative Auger recombination and therefore a lifetime typically much shorter than the exciton one. In our samples, biexcitons have zero binding energy and their optical emission cannot be distinguished in spectrum from the excitonic one.

3.5   The experimental set-up.
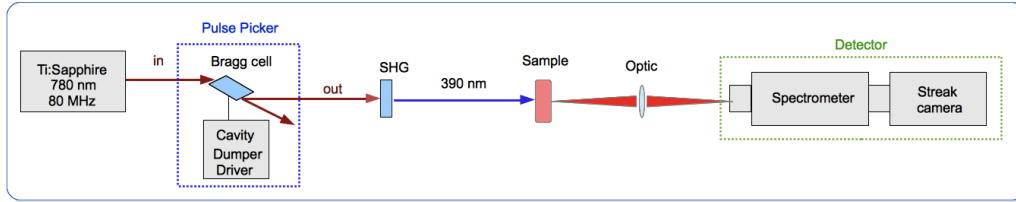
Figure 3.6: *Scheme of experimental set-up.*

We devise an experiment, variable pulse rate photoluminescence spectroscopy, to control the accumulation of charges and the activation of charge traps in colloidal nanocrystals. The dynamics of these states is studied, with pulse repetition frequencies ranging from a few hundred hertz to the megahertz regime, by monitoring photoluminescence spectrograms with picosecond temporal resolution. In figure 3.6 is shown a schematic of experimental set-up.

The laser source for the time-resolved photoluminescence setup is a titanium:Sapphire passively mode-locked femtosecond laser (Spectra Physics Tsunami, pumped by a diode, frequency-doubled Nd:YAG laser, Spectra Physics Millennia), emitting at 780 nm in wavelength, with a 80 MHz repetition rate, 100 fs pulse duration, and 10 nJ energy per pulse. The pulses are then sent to a home-made pulse picker, realized with a single-pass standing-wave acousto-optic crystal, able to extract selected pulses from the laser pulse train at a frequency variable from 400 Hz to 4 MHz, thereby dividing the laser repetition frequency by a factor ranging from 20 to 2×10^5. Laser pulses are then frequency-doubled to 390 nm in wavelength by focusing onto

a second-harmonic generation BBO crystal, 1 mm thick. Ultraviolet laser pulses are then directed and focused onto the sample with a quartz lens, down to a $150\mu m$ spot, to excite photoluminescence.

The excitation level of nanocrystals can be expressed as the average number N of excitons injected in each nanocrystal by a laser pulse, which can be in turn calculated by multiplying the photon fluence in each pulse by the absorption cross section of nanocrystals. The number of excitations in individual nanocrystals is distributed randomly according to Poisson statistics, so that both singly and doubly excited nanocrystals can emit under a specific excitation intensity. In order to check the accuracy of our determination of N, we compared the values obtained with the previous method with an alternate determination of the average number of excitations N, directly monitoring the very area of the excited sample from which light is detected: we employed the ratio between singly and doubly excited nanocrystals (the exciton to biexciton ratio); such measurement was performed at in the 'single-pulse' regime when contributions from charged states were negligible, as discussed in appendix A. Notably, such determination of N was in agreement with the one calculated by multiplying photon fluence and cross section, confirming the reliability of the estimation for the photon fluence impinging on the sample.

Collection optics focus photoluminescence into a 30 cm focal length spectrometer (Acton 2300i, equipped with a 150g/mm grating); time-resolved detection is performed with a streak camera (Hamamatsu model C5680) operating in single-shot mode, triggered by reference laser pulses. The temporal resolution of the setup is 10 ps with a 1 ns acquisition window, but degrades

to 50 ps with a 20 ns temporal range. The laser excitation spot, as focused on the entrance of the spectrometer, is much larger ($450\mu m$) than both the horizontal spectrometer slit aperture ($50\mu m$, determining spectral resolution) and the streak camera photocathode vertical slit ($50\mu m$, determining temporal resolution). Such aperture therefore acts as a pinhole in the image plane of the sample and ensures that only the very central part of the excited spot on the sample is actually measured.

3.6 Time resolved photoluminescence traces

Figure 3.7(a) shows the time-resolved photoluminescence traces from a nanocrystal toluene dispersion as a function of the laser repetition rate (ν), operating at fixed pulse energies; that is, in each panel, the number of photogenerated electron-hole pairs per dot per excitation pulse is kept constant (N = 0.0028, 0.09, 0.28, respectively); ν ranges from 400 Hz to 4 MHz.

At very low excitation fluences (N < 0.003, Figure 3.7(a)), the decay time of the emission signal is independent of pulse fluence and repetition rate, indicating that light emission comes from the radiative decay of single excitons, while the population of multiexcitons, trions, and photoactivated trap states is negligible.

For higher laser pulse fluence, namely, generating N = 0.09 excitons per nanocrystal (Figure 3.7(b)), a weak component with a fast decay is observed. However, repetition frequency does not affect transient emission, a clear indication that the short-lived signal is due to nanocrystals doubly excited by a single laser pulse (i.e., to biexcitons), while there is no accumulation of
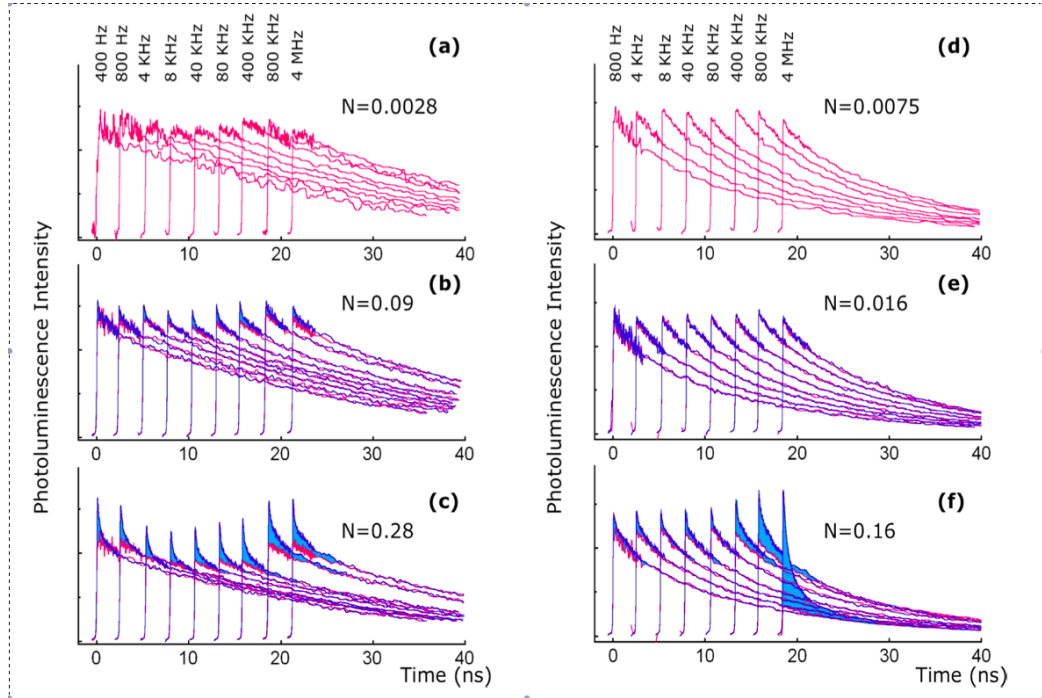
Figure 3.7: *Photoluminescence decays (blue lines) corresponding to nine excitation pulse rates for three pulse fluences. Emission decays from nanocrystal solutions are reported in panels (a-c), from nanocrystal films in panels (d-f). To better visualize all transient emission traces, decays are shifted to the right for increasing repetition frequency. Laser pulse fluence rises from top to bottom. Blue regions highlight the nonlinear emission signal, while red lines represent the excitonic contribution. At a fixed pulse fluence, this contribution was estimated by taking the emission signal recorded at very low excitation (solution: $N = 2.8 \times 10^{-3}$; film: $N = 7.5 \times 10^{-3}$), rescaled to match the higher excitation photoluminescence transient at time delays longer than 15 ns.*

charged states from pulse to pulse. At all excitation fluences and intensities, the photoluminescence decay rate of the single-exciton emission is recovered at long delays. This excitonic contribution for each transient photoluminescence is marked by a red trace with amplitude A_x and corresponds to the emission signal recorded in the single-exciton regime (N = 0.0028), rescaled to match the overall dot emission at the specific excitation fluence for time delays longer than 15 ns. The difference between the emission signal and the excitonic contribution, highlighted in cyan, provides a direct visualization of the short-lived nonlinear photoluminescence [NLPL(t)].

Figure 3.7(c) shows that frequency dependent quenching mechanisms manifest only at the highest fluences (N = 0.28) as a decrease of the emission signal for intermediate pulse repetition frequencies, $\nu = 800$ kHz. The reduction of the prompt photoluminescence, A_0, suggests that the laser pulse train induces the activation of trapping sites, which capture hot charged carriers before they can radiatively recombine. However, trap centers are not activated permanently, but are reversibly switched on and off in relation with the effective pulse fluence and repetition frequency.

Figure 3.7(d-f) highlights how charged states and traps depend on the environment surrounding nanocrystals. The figure panels report the photoluminescence emission decays obtained from a dropcast nanocrystal thin film; as for the liquid sample, the number of absorbed electron-hole pairs per dot per excitation pulse was kept constant for each series.

Figure 3.7(d,e) shows that the transient photoluminescence in the single-exciton regime, N = 0.0075-0.016, is frequency-independent. Only for excitation levels of N = 0.16, short-lived components are visible (Figure 3.7(f)).

In such conditions, the phenomenology appears different with respect to the liquid sample. At low frequencies, fast contributions show an amplitude and lifetime consistent with the presence of a small biexciton population. Quenching mechanisms become very effective at high pulse repetition rate, with a frequency threshold at 80 kHz. At the largest frequency, 4 MHz, the long-lived exciton contribution decreases down to 20% of the low-frequency signal, while the enhancement of the prompt emission signal is symptomatic of the formation of a charged exciton population.

3.6.1   Nonlinear photoluminescence response as a function of pulse fluence

The number of available pulse repetition frequencies above the threshold for emission quenching is limited by experimental constraints. To access a more detailed analysis of the quenching mechanisms, we therefore study the nonlinear response as a function of a complementary parameter controlling the accumulation of long-lived nanocrystal states, the pulse fluence, which we can finely tune. In analyzing results, one has however to account for the nonconstant contribution of multiexciton states to photoluminescence.

Figure 3.8 shows the prompt photoluminescence intensity and the contribution of single excitons extrapolated at time zero (A_0 and A_x, respectively) as a function of N for $\nu = 4$ MHz. Transient emission traces used to extract the amplitudes are reported in appendix A.

At low pulse fluences, the photoluminescence intensity grows linearly. At a threshold of about 0.05 exciton per nanocrystal, the long-lived emission starts saturating, while the prompt response shows a slightly superlinear
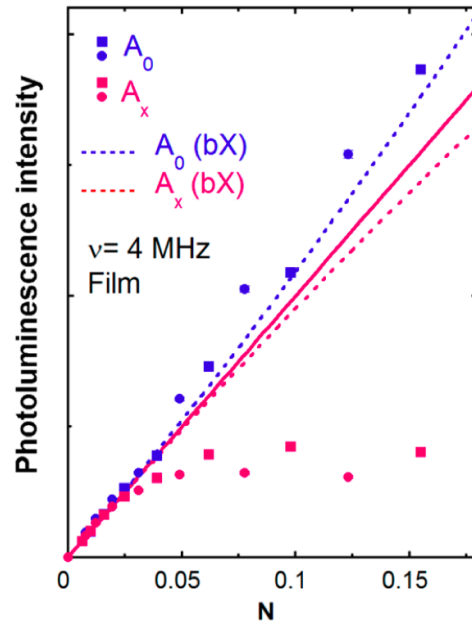
Figure 3.8: *Prompt photoluminescence signal(A_0,blue circles) and contribution to the experimental emission intensity originating from long-lived excitons (A_x, red circles) as a function of the average number of injected electron-hole pairs per dot (N). The tick red line represents a linear fit to $A_0(N)$ in the low excitation regime (N < 0.025). The two dashed lines represent the amplitudes expected for A_0 and A_x accounting only for biexciton effects, in the absence of trions and traps. Transient emissions were recorded in two different pulse energy scans. The second one was acquired 2 h later and is marked by squares.*

behavior. Remarkably, such saturation occurs for an average excitation N at least an order of magnitude lower than the standard saturation associated with state filling and is only observed at high laser pulse repetition rate; for $\nu = 800$ Hz, saturation effects up to N = 0.16 are negligible, as noticeable by a critical inspection of figure 3.7(f)). The two dashed lines represent the amplitudes expected for A_0 and A_x accounting only for biexciton effects, in the absence of trions and traps.

Experimental results in Figure 3.8 are representative of two different intensity scans, acquired with a 2 h delay between them, and identified respectively by round and square markers; for increasing number of electron-hole pairs injected per nanocrystal, experimental points belong alternatively to the first and second run. The two data sets show the degree of reversibility of photoinduced changes in the transient photoluminescence signal. In the delayed experiment, a higher long-lived excitonic emission is accompanied by a lower enhancement of the prompt signal. This correlation indicates that a prolonged illumination mainly reduces the efficiency of light-induced nanocrystal charging. [54, 55] Since the amplitudes of photoluminescence components related to traps show very little hysteresis effects when the laser fluence is scanned across the threshold for trap activation, we define trap activation as a reversible effect, apparently not entailing permanent modifications of nanocrystals or their surface ligands. Figure 3.8 demonstrates that quenching mechanisms for N = 0.15 are so efficient that about two over three excitons decay nonradiatively. If quenching were due to nanocrystal charging, two-thirds of the photoexcitations should be charged excitons, with faster radiative time than excitons, resulting in a large enhancement ($\sim 5/3$)

of the prompt emission signal with respect to the case in which only neutral excitons were created (red line in Figure 3.8). The weak enhancement of the prompt signal A_0 and the large reduction in the single-exciton contribution A_X therefore indicate that light-induced trap states also contribute to photoluminescence quenching. Experiments performed in different films showed similar results, even though the absolute and relative weight of charged states and trap centers to photoluminescence quenching are found to vary from film to film and with film aging.

3.7 Spectral analysis of the photoluminescence emission

Spectral analysis of the photoluminescence emission provided additional direct evidence of the contribution of trions to band edge photoluminescence. Figure 3.9 shows transient photoluminescence spectra extracted from streak camera spectrograms in a time gate of 0.1 ns close to 0.6 ns delay time, for both toluene dispersion figure 3.9(a) and drop-cast film figure 3.9(b) samples.

In solution, spectra at high and low excitation level are very similar, and only a slight red shift is observed at high excitation and high repetition rate. In the film instead, at high repetition rate and excitation level of 0.16 electron- hole pair injected per dot per pulse, the transient spectrum reveals a red-shifted emission with respect to the low-excitation spectrum; a weaker, blue-shifted component also appears. We attribute these two components respectively to negatively [56, 57] and positively [58, 59] charged nanocrystals. Concerning biexcitons, their emission spectrum, measured with the setup
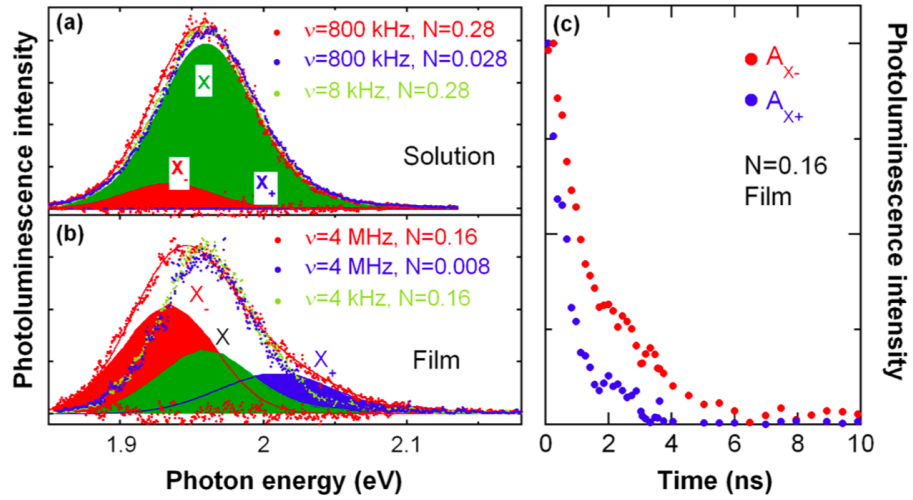
Figure   3.9:   *Photoluminescence   spectrum   (dots)   recorded   in   a   time window(Δt=0.1ns)centered   at   t=0.6ns,in   a   nanocrystal   (a)   solution   and   (b)   film. Red continuous lines are fits to emission spectra at the highest pulse fluence and repetition rates (film: ν= 4 MHz, N = 0.16; solution ν = 800 kHz, N = 0.28). Residuals from fits are also shown. X_-, X_+, and X represent emissions, as obtained from the fit analysis, due to positive and negative trions and excitons, respectively. (c) Decays of the trion amplitudes assessed from the fits as a function of time.*

for single-shot measurements described in appendix A, could not be distinguished from the excitonic one; therefore, spectral analysis does not provide information on biexcitons.

Analyzing spectra by deconvolving them as the sum of the low-fluence exciton emission line shape and two Gaussians for the positive and negative trions, respectively. A global fit of all transient spectra of nanocrystals in dispersion and in film gave trion binding energies of $(-25 \pm 5)meV$ and $(50 \pm 20)meV$, respectively, for negatively and positively charged excitons. Fitting the spectrum as a function of time and measuring the weight in the spectrum of the two lateral Gaussian curves, we are therefore able to track trion dynamics.

The result of the analysis is shown in Figure 3.9(c). At delays longer than the biexciton lifetime (τ_{bX}), the decay time of the photoluminescence signal can be safely ascribed to radiative recombination of neutral and charged excitons alone. The transient traces for $t > \tau_{bX}$ are then used to assess the lifetime of negative and positive trions. The accurate determination of τ_{bX} and the procedures used to determine the photoluminescence lifetimes for $t > \tau_{bX}$ are described in the appendix B. We obtain $\tau_{bX} = (0.40 \pm 0.03)ns$, $\tau_{X_-} = (2.3 \pm 0.2)ns$, and $\tau_{X+} = (1.1 \pm 0.2)ns$. The experimental values of the nonradiative decay times of trions and neutral biexciton (τ_{bX}) satisfy the relation $1/\tau_{bx} \sim 2/\tau_{X+} + 2/\tau_{X_-}$, as one could expect from statistics arguments and in excellent agreement with the pseudopotential theory of Auger lifetimes in colloidal quantum dots. [60]

3.7.1   Photoinduced traps and charge population

Thanks to spectral deconvolution of transient photoluminescence spectra, we determine the amplitude of the trion photoluminescence. Trion states are created with low fluence excitation, generating on average much less than one electron-hole pair per nanocrystal, only assuming that a fraction of nanocrystals are left charged by previous laser pulse excitation. We label
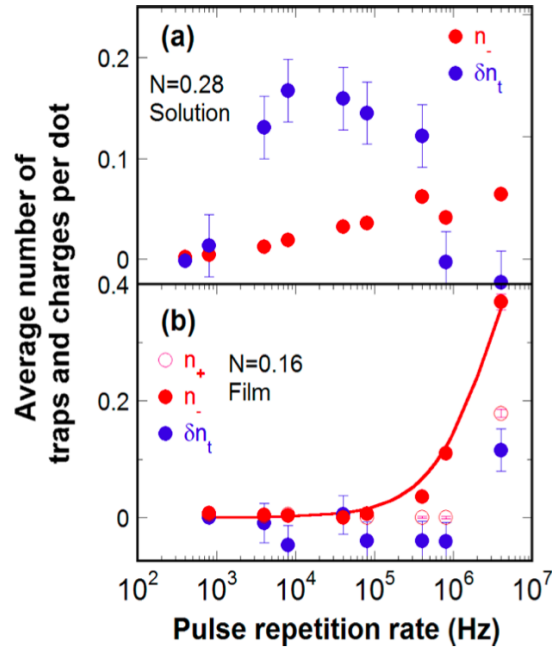
Figure 3.10: *Photoinduced traps and charges as a function of the pulse repetition frequency in nanocrystal solutions (a) and films (b). Fraction of nanocrystals with an additional negative (n_-) and positive (n_+) charge, and with a light-activated charge trap $\delta n_t(\nu) = n_t(\nu) - n_t(\nu_0)$. $\delta n_t(\nu)$ accounts for the photoinduced trap population with respect to the data taken at the reference frequency $\nu 0$ fixed to 400 and 800 Hz in solution and films, respectively. Red line in panel (b) is a curve for the negative charge population calculated according to eq 3.1, as explained in the text.*

n_- and n_+ the fraction of positively and negatively charged nanocrystals, whose excitation leads to X_- and X_+, respectively, in each nanocrystal. The fraction of negative and positive trions with respect to exciton population in turn is used to infer the steady-state population of charged nanocrystal states n_- and n_+, the precursor states that lead to trions upon optical excitation.

Analogously, we define n_h and n_{th} as the average number of hot charge (X_h) and thermal charge (X_{th}) traps per nanocrystal. Details on the procedures used to assess charge (n_-) and (n_+) and trap $(n_h$ and $n_{th})$ populations are reported in appendix B. Figure 3.10 shows the steady-state population of the charged nanocrystal state as a function of excitation conditions, resulting from the analysis of both film and dispersion. By measuring the amplitude A_x of the single-exciton component surviving for a long time after excitation, we also measure the yield for generation of single excitons and therefore extract the number of light-activated traps. We call the total population of trap states $n_t = n_h + n_{th}$ the sum of hot charge (n_h) and thermal charge (n_{th}) traps. In principle, n_t could include a background population of static traps, which are independent of pulse fluence and repetition frequency.

Figure 3.10 therefore reports the quantity $\delta n_t(\nu) = n_t(\nu) - n_t(\nu_0)$, which accounts for the photoinduced trap population with respect to the data taken at the reference frequency ν_0 fixed to 400 Hz. Finally, from the experimental values of A_X and A_0, we evaluate the photoinduced population of hot charge traps, $\delta n_h(\nu) = n_h(\nu) - n_h(\nu_0)$. We obtain that $\delta n_h \sim \delta n_t$, within the experimental uncertainty.

In the liquid dispersion (Figure 3.10(a)), we observe only emission from negatively charged excitons, whose contribution grows gently as a function of

laser repetition frequency, ν, following a logarithmic frequency dependence, with no evident saturation threshold for charge accumulation. In other words, we find no specific time scale associated with the creation of charged states in a liquid environment. Light-activated traps are found to contribute only in a range between 4 and 800 kHz, with values around 0.15 traps per dot.

On the other hand, in the film (Figure 3.10b()), the number of charged nanocrystals developing trions instead of excitons is negligible until laser repetition frequency reaches 800 kHz; at such frequency, the contribution of charged states kicks in and grows rapidly as a function of repetition frequency, with more than 35% of nanocrystals ending up negatively charged for $\nu = 4$ MHz. Positive trions are only observed at the highest repetition frequency, where the fraction of quantum dots with a photoinduced extra hole is $\sim 20\%$. Consequently, more than half of the nanocrystals are charged at this repetition frequency. Concerning traps, we find a sizable trap population, $\delta n_t = 0.1$, only at $\nu = 4$ MHz.

3.7.2 Photoinduced traps and charges as a function of laser fluence,

Figure 3.11 reports the analysis of photoluminescence data as a function of laser fluence, at the fixed frequency of 4 MHz. The average number of traps and charges per dot has been calculated according to the protocol for data analysis used for nanocrystal solutions. At the highest energy per pulse, figure 3.11 shows that most of quantum dots are weak emitters (gray states), due to a large photoinduced population of active traps ($n_{th} > n_h$) and the accumulation of a significant charge in the core of nanocrystals.
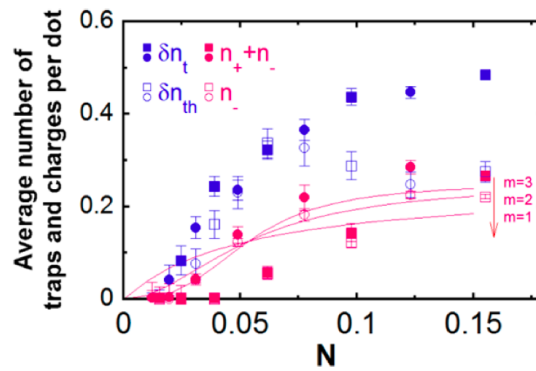
Figure 3.11: *Photoinduced traps and charges as a function of injected electron-hole pairs per dot in nanocrystal films. Fraction of nanocrystals with an extra charge in the core (n_- + n_+), an additional negative charge (n_-), light-activated charge traps (δn_t), and light-activated traps intercepting thermal charges (δn_{th}). Red lines are representative satura-tion curves for the charge population assuming a characteristic recombination time τ_-. Parameters are chosen to best reproduce the population of negative charges in non-photo-treated films (first scan in Figure 3.8); m is the power law index (see main text for definitions). Error bars correspond to one standard deviation.*

In a photocharging process, one electron (hole) is ejected outside the nanocrystals or trapped at the external surface, leaving the core with an unbalanced charge. Such process can start after photoexcitation of a single exciton because of trapping of one of the two charges composing the exciton, or following Auger recombination of a multiexciton state, when one exciton disappears and its energy is conferred to a single charge. In the simplest scenario, called a relaxation time model, split charges recombine with a characteristic lifetime $\tau_{+,-}$. Quasi-steady-state population of trap states can be assumed when $\nu\tau_{+,-} \gg 1$, meaning that n_- and n_+ at the arrival of the laser pulse are constant from one pulse to the next. In such condition, the charge population reads

$$n_{-,+} = \frac{N^m \nu \alpha \tau_{-,+}}{N^m \nu \alpha \tau_{-,+} + 1} n_{sat-,+} \tag{3.1}$$

where α is the probability that the excited state relaxes through nanocrystal ionization, while m is the order of the multiexciton state (mX) at the origin of photocharging (N is the average number of excitons per dot per pulse). At very low excitation intensities, the population scales as $N^m \nu \alpha \tau_{-,+}$. Charge saturation can be induced both by varying pulse repetition frequency ν but fixed N or by varying the pulse fluence, and therefore N, but keeping the repetition frequency ν constant. In the former case, $n_{-,+}$ grows linearly with the pulse repetition frequency ν, as long as $N^m \nu \alpha \tau_{-,+} \ll 1$, and eventually saturates at the value $n_{sat-,+}$ at high excitation frequencies, when $N^m \nu \alpha \tau_{-,+} \gg 1$. This same saturation value can be obtained raising the excitation fluence.

The sharp rise of n_- in nanocrystal films is well accounted for by eq 3.1

(Figure 3.10(b)). In experiments with fixed laser repetition frequency, but varying pulse fluence, one can expect to infer the origin of charged states from the dependence of $n_{-,+}$ on the mean excitation level, N, in the case of charge splitting in single exciton states, m = 1 and $n_{-,+}$ grows linearly with the mean excitation power, as $N\nu$; if, on the other hand, charge ejection is triggered by Auger processes, $n_{-,+}$ should scale at least quadratically, as $N^m\nu$ (with $m \geq 2$).

Figure 3.11 shows that the simple relaxation time model describes satisfactorily the saturation behavior observed experimentally, demonstrating that generation of negative charges in nanocrystal films is triggered by Auger recombination ($m \sim 2$).

The saturation pulse fluence, $N_{sat,-}$, defined as the number of injected electron-hole pairs at which $n_- = n_{sat,-}/2(N_{sat,-}^2 \nu\alpha\tau) = 1$ extracted from the saturation value in Figure 3.11 and turns out to be 0.05. The value $\alpha \times 10^{-4}$ is determined independently in single pulse experiments, that is, in the absence of charge accumulation between pulses, by fitting the amplitude of the trion emission as a function of the pulse fluence (see appendix A for a detailed description of the procedure). The knowledge of $N_{sat,-}$ and α leads to the determination of the characteristic relaxation time for negative charges, $\tau_- = 6 \times 10^{-2s}$. The time scale of τ_- is in excellent agreement with estimates obtained in single-nanocrystal experiments. [27, 40] In films previously exposed to irradiation, we observe a similar behavior except that the pulse fluence necessary to achieve charge saturation increases owing to photobrightening effects.

In nanocrystal toluene dispersions, contrary to the film samples, photo-

luminescence experiments show a slow increase of the fraction of negatively charged nanocrystals as a function of ν, with no evidence of saturation (Figure 3.10(a)). The stark contrast between charge accumulation behavior in nanocrystal solutions and films points to the key role played by the environment.

In solutions, the dependence of n_- on the excitation intensity $N\nu$ strongly deviates from the behavior foreseen by invoking a recombination time $\tau_{-,+}$, as explicitly assumed in eq 3.1. These findings suggest that the dynamics of the ejected charges could be strongly influenced by stochastic interactions with solvating molecules, resulting in a kinetics that is not characterized by a specific time scale. The importance of interaction with the surrounding medium may stem from the fact that ligands are not covalently anchored to the surface; their surface coverage should instead be seen as the result of the dynamical equilibrium between adsorption and desorption processes. [39,61] One possible explanation for the activation of trap states is changes in the local configuration of surface atoms and passivating ligands, with jumps between minima of the surface free energy possibly triggered by light. Two possible mechanisms can be envisioned: (i) following optical excitation, the excess photon energy and the annihilation energy of multiexciton states are quickly released to phonons and ligand vibrations, providing in this way the required energy to modify the local surface configuration; (ii) alternatively, or in addition to the previous mechanism, surface rearrangement could be triggered by interactions with charges created in photo ionization processes. The reversibility of the photoinduced activation of trap states suggests that surface atoms and ligands can relax to the original equilibrium configuration

in a relatively short time τ_t. Assuming a quasi-steady-state excitation ($\nu\tau \gg$ 1), the dynamics of trap states should be then described by an equation similar to eq 3.1.

Connecting the observed trap and charge dynamics with nanocrystal blinking is beyond the scope of this work. However, a link may be established considering that (i) neutral nanocrystals are bright emitters; (ii) charged excitons are weakly emitting and can be referred to as gray states; (iii) an exciton in the presence of hot charge traps does not fluorescence and therefore behaves as a dark state; finally, (iv) an exciton generated in dots with thermal charge traps decays radiatively with a quantum yield depending on the electron trapping rates. Light emission instabilities at the level of the single nanocrystal are thus expected to result from the transition of the dot from one to another of these states, a change that may be triggered by random interactions with the environment or induced by photon absorption.

3.8   Conclusion

To conclude the chapter I will briefly summarize the results obtained. We have introduced variable pulse rate photoluminescence as an experimental technique to investigate long-lived states in colloidal nanocrystals.

We measure lifetimes of single charges in nanocrystals and highlight different trap dynamics in liquid and film environments.

We demonstrate that dark and weakly emitting states, originating both from charges or traps, can be reversibly turned on and off by light. In the case of carrier traps, we suppose that light can indirectly induce a reversible local

reorganization of capping molecules on the nanocrystal surface. It has to be noted that the mechanisms of light-induced emission quenching revealed in the present experiments show up at injection levels corresponding to the single-exciton regime and repetition rates approaching the continuous wave excitation.

The design and engineering of novel colloidal nanocrystals for several photonic applications, such as quantum communications, bioimaging, super-resolution optical microscopy, light detection, and low threshold lasers, will benefit from a deeper knowledge of the class of quenching processes peculiar of quasi-continuous wave excitation regimes and their relationship with surface properties.

Chapter 4

CdSe/CdS Octapod nanocrystals

In the previous chapter I described experiment that was designed to investigate the mechanism of photoluminescence quenching in CdSe/CdS core/shell nanocrystals. In this chapter I will describe experiment which is designed to investigate the efficiency of charge separation in a different nanostructure: CdSe/CdS octapod shape nanocristals. The specific and unique optical and electronic properties of this nanocrystal make it particularly suitable to be used in applications of photocatalysis.

The work presented in this chapter has been published in the journal *Nanoscale* with the title: *Charge separation in Pt-decorated CdSe/CdS octapod nanocrystals.* [62]

4.1   Colloidal nanocrystals in applications of solar photocatalysis.

Colloidal nanocrystals represent a promising platform for scalable, low-cost exploitation of solar energy through the realization of solution-processable solar cells and photocatalytic reactors. [63–65] Photoconversion functionalities with colloidal nanoparticles require a specific design of the interfaces: defects, dangling bonds and potential barriers hinder the extraction of photoexcitations and their energy from nanocrystals. [66] A viable strategy to overcome limitations relies on the growth of colloidal nanostructures with junctions between domains of different materials, realizing the device functionality at the nanometric scale. [10, 67–69] Such strategy may prove especially valuable for solar water splitting, an application where several interfaces and vectorial charge transport are usually required. [63, 66, 70–73] The choice of semiconductor materials for solar water splitting is subject to the fulfillment of thermodynamic requirements: the bandgap has to exceed the minimum 1.23 eV value, corresponding to the net free energy in the water splitting reaction, with the correct offset with respect to vacuum level.

CdS-based nanocrystals have the right level alignment and have been particularly amenable to the realization of complex shapes and heterostructures, like branched nanocrystals. [74, 75] Multipod nanocrystals appear well suited for realization of complex optoelectronic functions needed in photocatalysis, as their topology may favor multiple step relaxation pathways for optical excitations. Recent advances in nanocrystal fabrication have managed to produce CdSe/CdS nanocrystals with up to 8 separate pods, realizing highly

branched yet well defined nanostructures. [76–78] The fact that the water splitting reaction is energetically favorable does not imply it will actually occur under solar illumination, due to the presence of activation barriers and kinetics bottlenecks. Catalysts are typically required for efficient photoconversion reactions and noble metals are the most widely used materials. Photocatalytic water splitting has been pursued with CdSe/CdS-based elongated nanocrystals decorated at the surface with noble metal domains, employing a variety of methods for nanocrystal decoration and resulting in different sizes, shapes and locations of the metal domains, both with selective noble metal deposition on the nanorod tips and a non-selective coverage of the nanocrystal surface. [79–92] In figure 4.1 is shown the alignment of the electronic levels in the case of CdSe/CdS nanocrystals decorated with platinum. A corresponding variety of electron transfer rates have been reported,
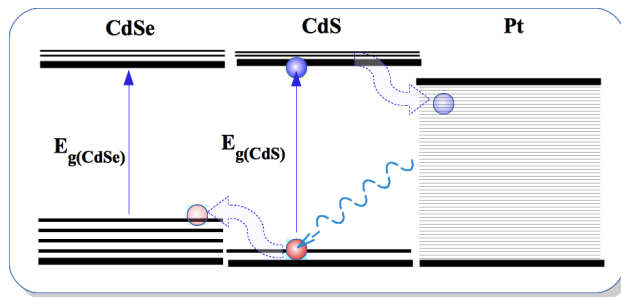

Figure 4.1: *Sketch of the electronic levels in CdSe/CdS nanocrystals decorated with Pt.*

but it is unclear whether complete surface coverage or selective tipping with noble metal domains is the most promising nanocrystal architecture because of a lack of direct comparison between heterostructures with equal composition and size obtained by the same synthetic route, highlighting a correlation

between microscopic structure and optoelectronic function.

4.2   CdSe/CdS Octapod nanocrystals.

CdSe/CdS octapod nanocrystals are grown [1] in the wurzite structure through colloidal route from a sphalerite CdSe core obtained by cation exchange of a $Cu_{2-x}Se$ seed. [77] In figure 4.2 is shown a geometrical represen-
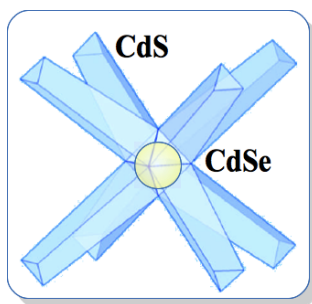

Figure 4.2: *Geometric representation of CdSe/CdS octapod shape nanocrystal.*

tation of the nanocrystal. TEM observations, as shown in Fig.4.3, indicate that the octapods tend to lay on the substrate sitting on four arms and are homogeneous in shape and size, with average pod length and diameter of 48 nm and 12 nm, respectively. As shown by previous investigation, the octapod arms grow along the c axis due to the faster growth of the high-energy (0001) facet of the wurzite structure.

---

[1]Synthesis of nanocrystals was realized by the Italian Institute of Technology (IIT) by Mee Rahn Kim and Liberato Manna.
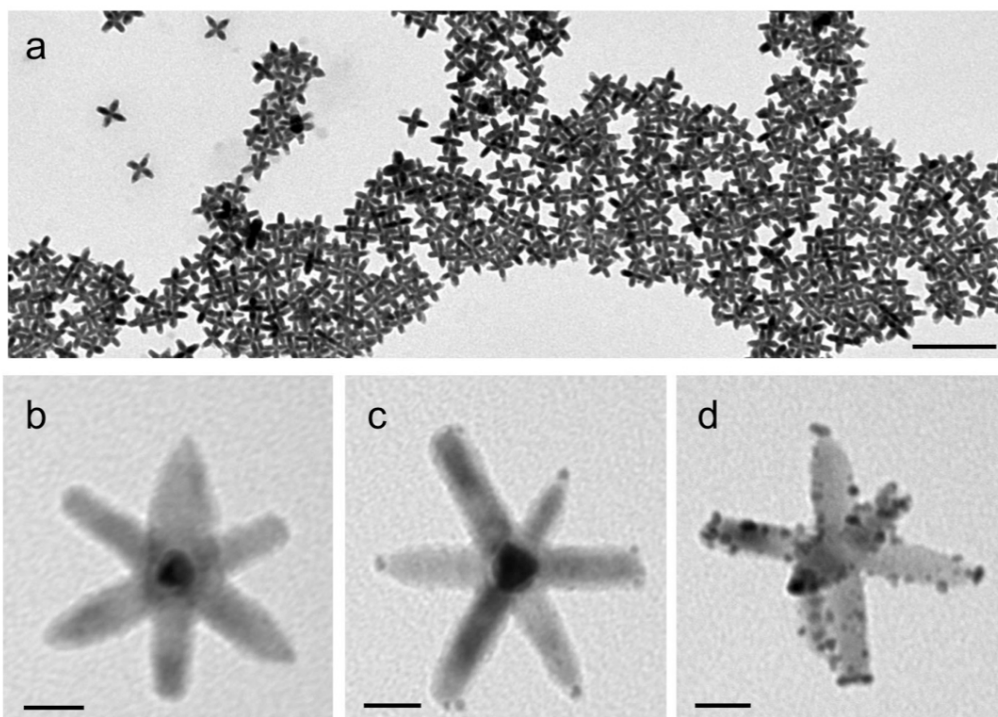
Figure 4.3: a) TEM image of an ensemble of CdSe/CdS octapod nanocrystals, highlighting the homogeneity in shape and size in the batch; the scale bar is 200 nm. Representative images of (b) a single Pt-free octapod nanocrystal, (c) a single Pt-tipped octapod nanocrystal and (d) a Pt-covered octapod nanocrystal. Scale bars in (b), (c) and (d) are 20nm.

4.2.1   Nanocrystal decoration

The metal-semiconductor interface is realized in a second step by decorating the octapod surface with Pt domains.[2] The synthesis are set so that the dimensions of Pt nanoparticles do not depend on the concentration of precursors. The aim of the decoration procedure is to control the geometry of the attachment of Pt to the CdS surface, without varying the morphology of octapod nanocrystals nor that of Pt domains. The degree of Pt coverage of the CdS surface is controlled by the amount of Pt precursors in solution: low Pt concentrations result in a selective deposition of Pt only on the most reactive surfaces, i.e. on the pod tips (Fig. 4.3(c)); on the other hand, a five-fold increase in Pt concentration results in a non-selective, extensive Pt coverage of the entire pod surface (Fig.4.3(d)). It should be pointed out that, as desired, in both Pt-tipped and Pt-covered CdSe/CdS heterostructures the size of the metal domains is around 3.5 nm.

4.2.2   Nanocrystal characterization.

X−ray diffraction data in Fig.4.4(a) reflect the occurrence of anisotropic hexagonal CdS phase and peak broadening provides size estimates in agreement with what inferred directly from TEM images, an indication that nanocrystals are mainly single crystalline domains. The main reflection of the Pt structure can be observed in the Pt-covered octapods, with average nanocrystal size 3.5 nm. Fig.4.4(b) shows the effects of Pt decoration on the

---

[2]Decoration of the nanocrystals was realized by Dipartimento di Scienze Chimiche e Geologiche and INSTM, Universita degli Studi di Cagliari, by Erika Conca, Maria Francesca Casula, Danilo Loche and Anna Corrias.
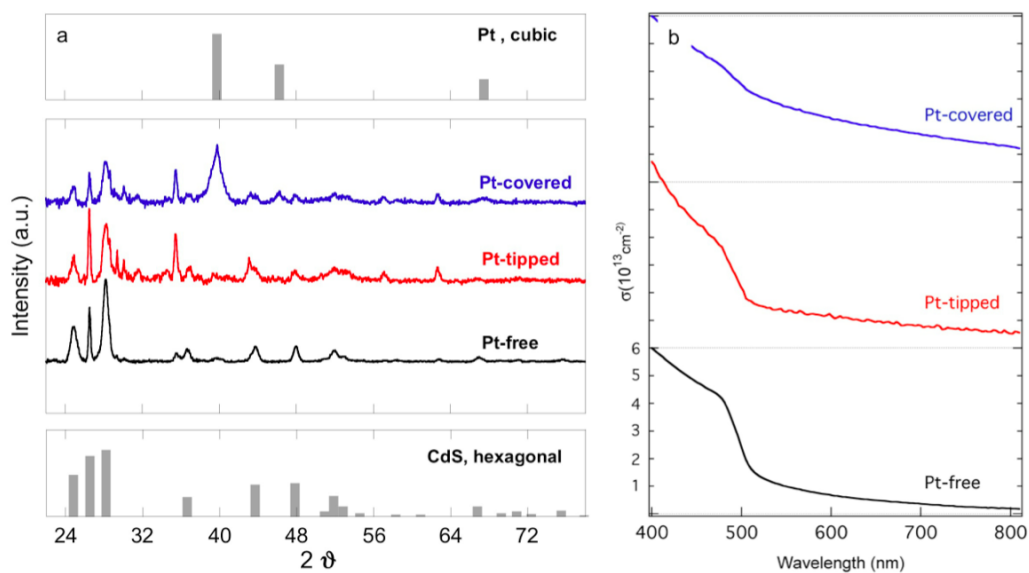
Figure 4.4: (a) X−ray diffraction patterns of the Pt−free, Pt−tipped, and Pt−covered octapod nanocrystals. The diffraction peak position of the bulk CdS hexagonal and Pt cubic structures are reported on the bottom and on top, respectively, as a reference. (b) UV-Vis absorbance measured in a toluene dispersion of Pt−free, Pt−tipped and Pt−covered octapod nanocrystals.

optical absorption: spectra for Pt-free octapods are characterized by a sharp absorption edge around 500 nm in wavelength, corresponding to the optical bandgap of CdS, followed by a Rayleigh diffusion tail; knowing the concentration of nanocrystals in dispersion, we determine the absorption cross section to be $\sim 6 \times 10^{-13} cm^2$ at 400 nm. When Pt is added, Rayleigh diffusion grows with the amount of Pt, as expected from plasmonic field enhancement effects. No clear plasmon resonance is however observed.

The absorption cross section does not appear to be significantly modified by the Pt decoration procedure; however, the limited quantities of Pt-decorated nanocrystals obtained after purification procedures have prevented an accurate determination of the concentration of nanocrystal dispersions and therefore uncertainties of the order of 30% need to be considered for the quantitative assessment of the absorption cross section.

4.3   Ultrafast optical spectroscopy

Producing large nanocrystals with a spatially controlled metal-semiconductor heterostructure represents a versatile playground for testing some of the photophysical processes relevant for solar photoconversion. CdSe/CdS heterostructured nanocrystals have a quasi-type II band alignment, with conduction bands almost aligned and the CdSe valence band higher in energy than the CdS one; [52, 93–98] the relaxation paths of photoexcited electrons and holes are also influenced by surface and interface morphology. [3, 31, 99–101] The photophysics of Pt-decorated nanocrystals is studied here with ultrafast optical spectroscopy, in particular femtosecond transient absorption, a

technique sensitive to the dynamics of the excited state. [102]

4.3.1 Transient absorption spectroscopy experimental setup.

The laser source employed for this experiments was a Ti:Sapphire regenerative amplifier (Quantronix Integra C) operating at a repetition rate of 1 kHz and emitting at 786 nm in wavelength. The absorption spectrum was probed with white-light continuum 150 fs-long laser pulses, 450-700 nm in spectrum, generated by focusing the output of the regenerative amplifier, attenuated to approximately $1\mu J$ energy per pulse, on a 1 mm sapphire plate. Probe pulses had a variable delay with respect to pump pulses (394 nm wavelength, 150 fs-long). Pump and probe beams were focused on a 1 mm quartz cuvette filled with nanocrystals dispersed in toluene.

The cumulative effect of spectral chirp and wavefront distortion of laser pulses resulted in a 200-fs time- delay resolution. The concentration of nanocrystals was chosen to keep the optical density of the whole cuvette around 0.3 at 400 nm in wavelength, guaranteeing the best compromise between uniformity of excitation and magnitude of the transient absorption signal. Optical spectra were recorded with a CCD camera (Andor Newton. 16 bit resolution, used in vertical binning) coupled to a grating spectrometer (Acton SP2300i, equipped with a grating 300 groves/mm). Sample transmission was measured by dividing the spectrum of white light pulses sent through the sample by the spectrum of similar pulses split before reaching the sample.

Differential transmission $\Delta T/T = (T_{on} - T_{off})/T_{off}$ was obtained by

recording sequential transmission spectra with (T_{on}) and without (T_{off}) pump pulses illuminating the sample. Typical sensitivity to differential transmission changes in our set-up was about 10^{-4} with few seconds acquisition time. Absorption and differential absorption spectra could be traced back through the relation linking absorption A and transmission T, when reflection and scattering are neglected: A=1-T.

4.3.2 Differential transmission measurements in the linear regime

The differential transmission signal induced by the pump laser pulses is almost exclusively attributed to photoexcited electrons, while holes do not contribute, due to the peculiar electronic level structure of CdSe and CdS nanocrystals, where hole states are closely spaced together and the states at the very top of the valence band are not coupled to optical transitions. [7] Care was taken to avoid nonlinear effects due to multiple excitation of each nanocrystal by each laser pulse; laser fluence for such measurements is 0.6 $\mu J/cm^2$, corresponding to an average of 0.7 excitations per nanocrystal per pulse.

In order to exclude that the Pt decoration procedure introduces surface trap states that can lead to similar photophysical signatures as electron capture by Pt domains, Pt-free nanocrystals are pre-treated in the same hot bath used for Pt decoration, without adding Pt precursors.

We measured time-resolved photoluminescence and transient absorption in octapod nanocrystals before and after the treatment at 200 °C simulating the decoration procedure. Figure 4.5 shows the comparison of the results
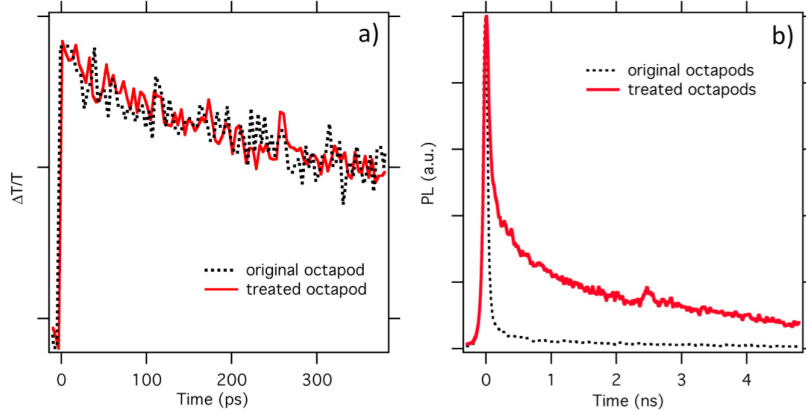
Figure 4.5: *(a) Comparison of differential transmission signals in Pt-free nanocrystals before and after the 200 °C treatment; the spectral integration window is 460-520 nm. (b) Comparison of time-resolved photoluminescence signals in Pt-free nanocrystals before and after the 200 °C treatment; the spectral integration window is 400-600 nm.*

obtained. The results show that differential transmission dynamics is not affected, meaning that no new traps for electrons are created. The shortening of the differential transmission decay in Pt-decorated nanocrystals, discussed can therefore be safely attributed to electron capture by Pt. On the other hand, the photoluminescence lifetime increases significantly following the treatment. Since we attribute the photoluminescence lifetime to hole trapping, we infer that the treatment alter the amount of surface traps for photoexcited holes and their depth. The differential transmission traces in Fig.4.6(a) are shown as a function of the pump-probe delay, so they reproduce the temporal dynamics of photoexcited electrons in the nanocrystals: Pt tipping accelerates the electron decay with respect to Pt-free nanocrystals, meaning that electrons can be trapped at the tips in a time scale of few
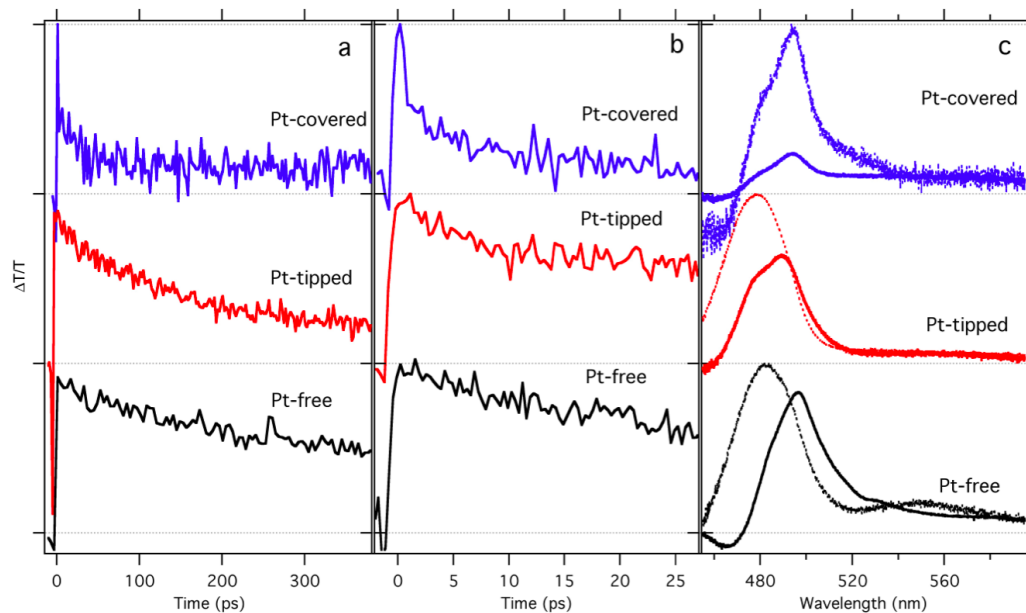
Figure 4.6: *(a) Decay of the spectrally-integrated differential transmission signal as a function of pump-probe delay for CdSe/CdS octapod nanocrystals with different Pt decorations; the spectral integration window is 460-520 nm; signal amplitudes are normalized and vertically displaced for clarity. (b) Zoom of the initial decay. (c) Corresponding differential transmission spectra; the dotted lines are the spectra at time delay equal zero (integrated over a 400 fs window), the continuous lines are the spectra integrated between 7 ps and 20 ps delay times.*

hundreds of ps; a fit to a single exponential decay without constant background gave characteristic times of $(630 \pm 50)ps$ for Pt-free nanocrystals and $(260 \pm 30)ps$ for Pt-tipped nanocrystals.

When the nanocrystals are entirely covered by Pt, however, the electron capture becomes much faster and is almost complete in a $1 \sim ps$ timescale, as shown in the zoom of the initial decay in Fig.4.6(b). Differential trasmission spectra, in Fig.4.6(c), reveal the photophysical processes. In Pt-free octapods and in tipped octapods the differential transmission spectra show similar dynamics: at time zero, just after excitation with the pump pulse, the bleaching is centered at 480 nm in wavelength, which has been associated by Scotognella and coworkers to the 1D electron state delocalized along the pod; [103,104] after a short transient of ~1-2 ps, the bleaching shifts towards the red and the corresponding peak moves to around 495 nm, a wavelength associated to the 0D electron state localized in the center of the nanocrystal.

Such dynamics is the signature of energy relaxation of photoexcited electrons from higher to lower energy states in the conduction band, accompanied by a spatial migration from the pods (1D states) toward the nanocrystal center (0D states). [103] 0D states are localized not by a band potential, but mainly by a geometric effect [103] ,as the nanocrystal cross section is larger in the core than in the pods and the corresponding confining energy is lower. Therefore 0D states would exist even in a nanocrystals with CdS core and extend well within the CdS arms. Such localization is shallow, as the difference in energy between 0D and 1D states is around 70 meV, the effective mass for electrons is just 0.1 and thermal energy $K_B T$ is at least 26 meV.

Relaxation is very similar in Pt-free and Pt-tipped nanocrystals because

electron capture in tipped nanocrystals is a much slower process than energy relaxation, which is completed in ∼1 ps. As a consequence, electron capture in Pt-tipped nanocrystals occurs from the 0D states, mostly localized in the center, which have little spatial overlap with the Pt domains located on the opposite side of the pods. As the localization of 0D states is mild, electron capture could be characterized as a tunneling through a shallow barrier. The photoinduced absorption band at 460 nm is attributed to Stark effect, i.e. the electric field created upon the excitation of electrons and holes that have not a perfect spatially overlap. The Stark signal is expected to scale as a combination of first and second derivative of the absorption spectrum and is therefore more pronounced in the samples where the absorption features are sharper, i.e., in Pt-free octapods.

In Pt-covered nanocrystals, relaxation from 1D to 0D states does not occur, as the bleaching of the 0D state always dominates over the one corresponding to the 1D state, even immediately after excitation. Furthermore, combining the differential transmission with the absorbance spectra in Fig. 2b, we can calculate the peak in transient absorption signal ($\Delta\alpha/\alpha_0$) to be about 4 times lower in Pt-covered nanocrystals than in Pt- free and Pt-tipped ones, where instead the values are about the same. We interpret the observation as an indication that bleaching in Pt-covered nanocrystals is only due to the fraction of electrons that after excitation directly relax into the 0D state, without transiting by the 1D states; on the other hand, we infer that electrons in the 1D states are captured by Pt domains before relaxation occurs, while they are still hot. In other words, electron capture in Pt-covered nanocrystals is fast enough to compete with energy relaxation. Since relax-

ation into the 1D states appears instantaneous in Pt-free nanocrystals, we also infer that electron capture in Pt-covered nanocrystals is faster even than the laser pump pulse duration.

Transient absorption tracks photoexcited electrons, but is mostly blind to photoexcited holes. To complete our photophysical investigation, we employ time-resolved photoluminescence, a technique that is sensitive to the simultaneous presence of electrons and holes.

4.3.3 Time-resolved photoluminescence experimental setup.

Samples were optically excited with the same laser used for transient absorption, frequency-doubled to 392 nm in wavelength and focused to a 150 μm spot. The optical emission was collimated using a 100-mm focal-length achromatic doublet. Transient emission measurements were performed using a 300-mm spectrometer (Acton SpectraPro 2300i equipped with a 50 grooves/mm grating) coupled to a picosecond streak camera (Hamamatsu C5680) providing $\sim$20 ps temporal resolution in operating conditions.

4.3.4 Time-resolved photoluminescence measurements.

CdSe/CdS octapod nanocrystals are known as inefficient emitters, contrary to other CdSe/CdS colloidal nanostructures, as spherical core/shell and dot/rods, as we have seen in the previous chapter.

The low photoluminescence quantum yield may be related to the peculiar synthesis technique, which involves cation exchange of the original Cu_2Se core to produce the CdSe seed for nucleation of the eight CdS arms, a procedure that may leave potential barriers and crystal defects at the CdSe/CdS
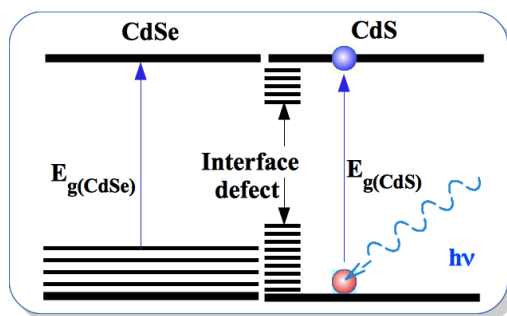
Figure 4.7: *Sketch of the alignment of electronic levels in CdSe / CdS octapod, probably interface defects that prevent electron-hole recombination in the CdSe core.*

interface, inhibiting the relaxation of holes into the CdSe core as shown in Fig.4.7. As a consequence the optical emission from octapod nanocrystals does not occur from the CdSe core, but from the CdS arm, and is centered in wavelength around 480 nm, as shown in Fig. 4.8(a). The emission spectrum is slightly blueshifted in Pt-tipped and Pt-covered nanocrystals.

The photoluminescence of Pt-free octapod nanocrystals decays in $\sim$100 ps, a value close to the resolution of our streak camera; since transient absorption indicates a longer lifetime for electrons, we attribute the photoluminescence decay to hole trapping at the CdS surface. The photoluminescence dynamics is different in Pt-tipped and Pt-covered nanocrystals, as the decay becomes longer. It has to be noted however that the longer photoluminescence decay is not accompanied by a higher quantum yield; on the contrary the quantum yield stays below 1% in all samples and is about 3 times lower in Pt-tipped and Pt-covered nanocrystals than in the Pt-free ones. This observation is consistent with transient absorption showing that the lifetime of electrons inside the nanocrystals is shortened by the addition
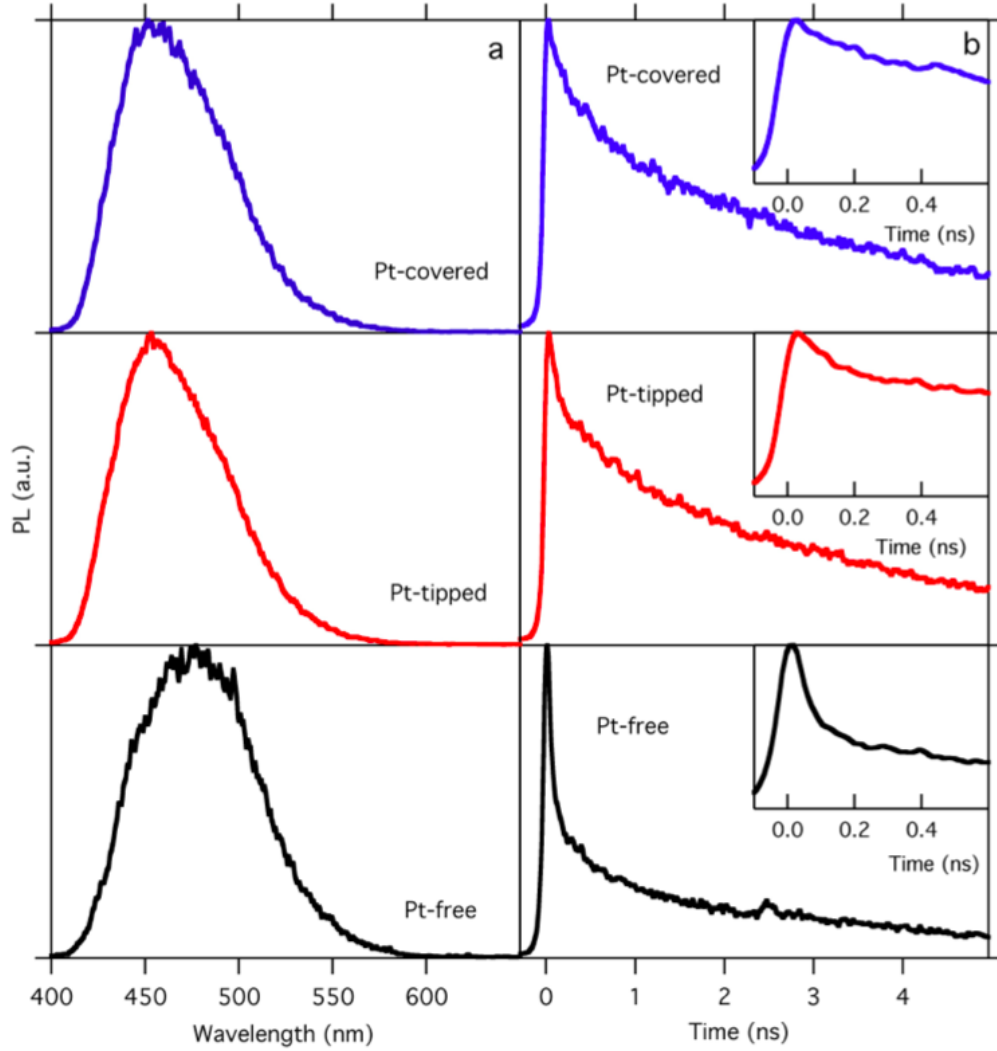
Figure 4.8: *(a) Photoluminescence spectra acquired with the streak camera for octapod nanocrystals. (b) Corresponding temporal decay of the normalized photoluminescence signal; spectral integration is done over the whole photoluminescence spectrum, 400-600 nm. Vertical displacements are for clarity. The insets show a magnification of the initial photoluminescence transient.*

of Pt. However, the timescales involving electron capture and photolumines-
cence decay are different by at least one order of magnitude, therefore we do
not quantitatively link the quantum yield value to the electron capture rate:
electron capture in Pt-tipped and Pt-covered nanocrystals may have different
rates, but after few hundred ps, the total number of electrons that have been
captured and therefore subtracted from photoluminescence may be similar,
resulting in a comparable PL quantum yield. We infer that the treatment
employed for Pt decoration affects the hole surface traps, probably saturating
the deepest ones and therefore slowing down the hole recombination

4.3.5   Differential transmission Measurements in the high-excitation regime

All ultrafast optical measurements presented up to now have been per-
formed in the linear regime, with the pump fluence low enough to ensure that
the transient absorption dynamics do not depend on the excitation level.
Fig. 4.9 instead compares the differential transmission signals in Pt-free,
Pt-tipped and Pt-covered nanocrystals as a function of the excitation flu-
ence in the high-excitation regime, where every single laser pulse is intense
enough to inject many photoexcitations in each nanocrystal (note that even
the lowest laser fluence in Fig. 4.9 is much higher than what employed in
the linear measurements in Fig. 4.6 and 4.8). In Pt-free nanocrystals (Fig.
4.9(a)), as the excitation fluence is increased, the bleaching signal blue-shifts,
as higher-energy transitions that are increasingly filled up with photoexci-
tations. Increasing the excitation level also produces a faster decay (Fig.
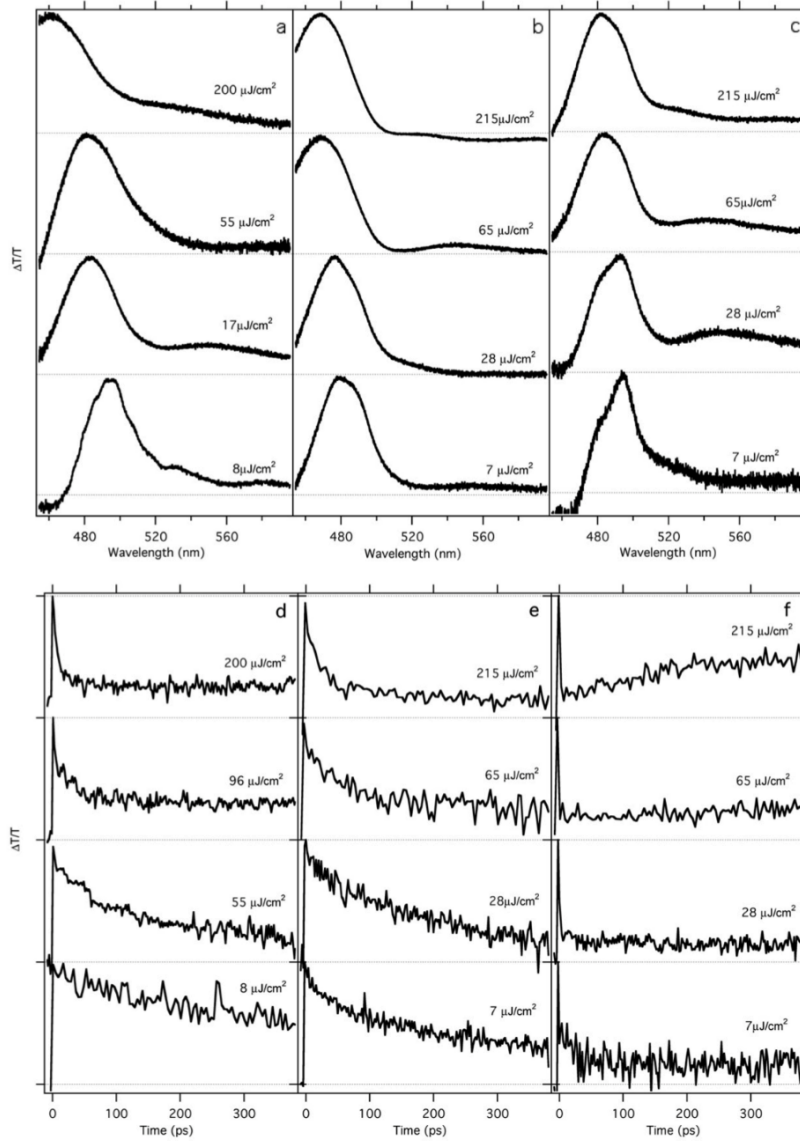4.9(d)), a signature of non-radiative Auger recombination occurring when

Figure 4.9: *(a)-(c) Differential transmission spectra as a function of laser fluence for CdSe/CdS octapod nanocrystals with a varying amount of Pt coverage: (a) Pt-free, (b) Pt-tipped, (c) Pt-covered; the spectra are integrated over a 2 ps window. (d)-(f) Corresponding dynamics of the differential transmission signals as a function of the delay time between pump and probe pulses: (d) Pt-free, (e) Pt-tipped, (f) Pt-covered. The spectral integration window is 450-520 nm. $10\mu J/cm^2$ in excitation fluence corresponds to an average of 11.8 excitations per nanocrystal per pulse for Pt-free nanocrystals. Vertical displacements are for clarity.*

many photoexcitations are confined inside the same nanocrystal. [37] The
Auger decay rate increases for increasing excitation levels, as the growing
number of excitations coexisting in the same nanocrystal enhances the rates
of scattering among carriers. State filling and blue-shift of bleaching for
increasing pump fluence are also apparent in the differential transmission
spectra of Pt-tipped nanocrystals, as shown in Fig. 4.9(b)), but they are less
pronounced than in Pt-free nanocrystals. We attribute such difference to
the fact that, even in the multiple excitation regime, a large fraction of the
photoexcited electrons are ejected from the nanocrystals due to the Pt dec-
oration. The temporal dynamics in Fig. 4.9(e)) confirms a shortening of the
differential transmission decay in tipped nanocrystals for growing excitation
levels, which can be linked to Auger recombination. However such shorten-
ing is modest in magnitude and, for the highest excitation levels we employ,
the differential trasmission decay turns out to be longer than in the corre-
sponding Pt-free nanocrystals. We infer that the Pt tips reduce the Auger
scattering rates, probably by promoting spatial charge separation even at
very early times after excitation, when photoexcited electrons are still inside
the nanocrystals.

In Pt-covered nanocrystals (Fig. 4.9(c) and 4.9(d)), the amplitude of the
differential transmission signal decays rapidly, even at low excitation intensi-
ties, not because of Auger recombination, but due to fast electron capture by
Pt domains. For growing pump fluences, the blueshift of differential trasmis-
sion signal shows that 1D states in the CdS pods are filled at comparably
much higher excitation levels with respect to Pt-tipped nanocrystals, which
we interpret as a confirmation of the fact that charges are separated and

photoexcited electrons extracted from the nanocrystals before contributing to the bleaching signal in the semiconductor. A spectrally-flat bleaching signal also appears at longer wavelengths and grows for growing pump fluences, which we attribute to excitation of plasmon modes in Pt domains. [7]

4.4 CdSe/CdS nanocrystals octapod applications in photocatalysis.

If the final goal of nanocrystal decoration with noble metal is to make them suitable for photocatalysis, Pt-decorated octapods appear very promising, Figure 4.10 shows an example of a possible application of these crystals decorated in photocatalysis. The shape of such nanocrystals offers several distinctive advantages for photocatalytic applications, namely controlled charge separation and large absorption coefficients.

Even more important, the absorption cross section is very high, as much as $5 \times 10^{-13} cm^2$ at 500 nm in wavelength, meaning that under AM 1.5 solar illumination photoexcitations in each nanocrystal can be created at rates equal to $10^5 s^{-1}$.

Future studies with nanocrystals in hydrogen-production conditions will have to establish what is the best condition to maximize water splitting efficiency: selective Pt tipping of nanocrystals provides control over the spatial separation between electrons and holes while minimizing the amount of noble metal employed; on the other hand, non-selective Pt coverage of the CdS surface leads to faster charge separation, but may be less efficient in catalyzing reactions or more prone to unwanted recombination paths leading to back
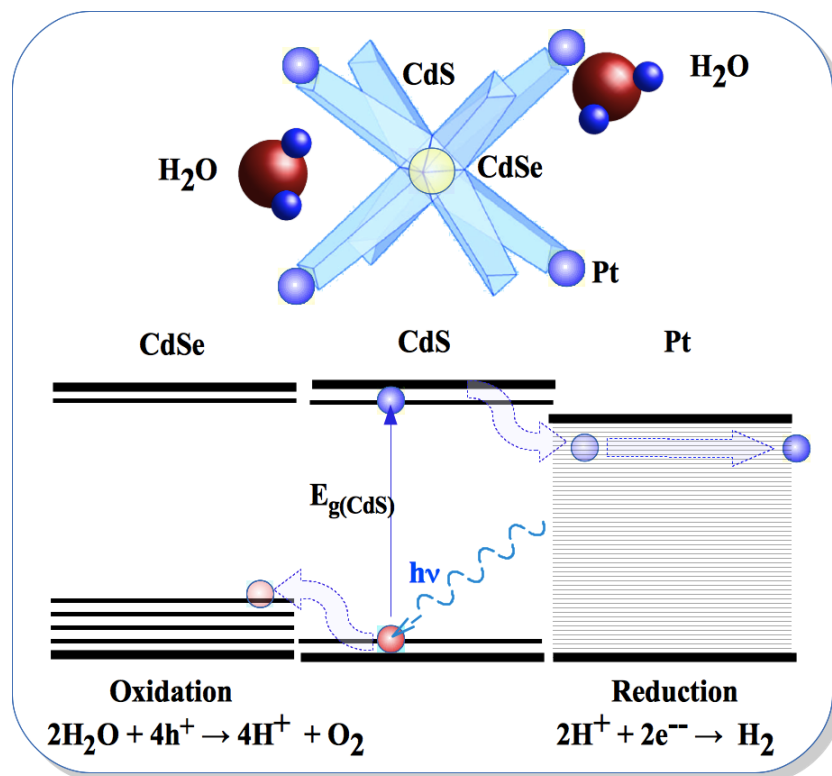
Figure 4.10: *Sketch showing octapod nanocrystal with selective decoration of platinum and their possible use in photocatalytic water splitting and the corresponding diagram of electronic levels.*

reactions.

4.5   Conclusion

In conclusion of this chapter I will summarize the results obtained in this study on CdSe/CdS octapod nanocrystals. Our measurements show that electron capture by Pt tips occurs in ∼200 ps, providing just a perturbation to the excited state dynamics, while in Pt-covered nanocrystals electron capture is much faster, ∼1ps, and competes with energy relaxation and Auger recombination, causing the capture of hot electrons. Injection of multiple excitons in each nanocrystals results in the simultaneous charge separation by Pt domains of tens of electrons available for chemical reactions.

Chapter 5

Bi$_2$S$_3$ nanocrystals

In the previous two chapters, I have described experimental work on different nanostructures of CdSe/CdS, a semiconductor extensively used and studied in various optoelectronics applications. In this chapter, I will describe experiment on Bi$_2$S$_3$ nanocrystals, a semiconductor still little studied, but that presents considerable advantages compared to previous CdSe/CdS nanocrystals from the point of view of environmental sustainability. In fact, in recent years in the field of optoelectronics properties such as non-toxicity, recyclability and sustainability are becoming increasingly important and determine the choices of new materials.

The work presented in this chapter has been published in the journal *Advanced Functional Materials* with the title: *Colloidal Bi$_2$S$_3$ Nanocrystals: Quantum Size Effects and Midgap States.*

5.1   Bi$_2$S$_3$ semiconductor nanocrystals

A wide variety of materials has been used to fabricate semiconductor nanocrystals, but most of them employs materials containing heavy metal elements as cations, such as Pb or Cd, which could pose health hazard if deployed on large scale. For this reason, environmentally benign nanocrystals are currently a very central topic in materials research for solar energy conversion. [105–111] Bismuth sulfide (Bi$_2$S$_3$) belongs to the class of non-toxic and earth-abundant semiconductor materials that can be synthesized in nanocrystalline form by cheap colloidal synthesis. [112] The large absorption cross-section and the direct band gap in the near infrared have further attracted significant interest. [113]

So far, research efforts have been addressed to the fabrication of solution-processed optoelectronic devices, including high-efficiency Vis-NIR photodetectors [114], inorganic [105] and hybrid [106,107,115] bulk nano-heterojunctions for solar energy conversion and sensitized mesoscopic solar cells. [116] Several synthesis approaches have been also proposed to improve the control of nanocrystal size and shape. [112,113,115,117–123]

This growing attention has not seen a parallel progress in understanding some key physical materials properties. Band gap tunability via the quantum size effect is a nanocrystal property that can be exploited to develop unique photovoltaic cell architectures for a more efficient solar light conversion. [66, 124–126] Nonetheless, the question concerning the extent to which the optical band gap can be tuned in Bi$_2$S$_3$ nanocrystals has not yet received an adequate quantitative answer. [113,123] Only recently, theoretical investigations have started addressing this issue in the framework of atomistic simulations, [127]

but a systematic experimental-theoretical comparison is still missing.

A distinguishing property of Bi$_2$S$_3$ is the strong anisotropic crystal structure, consisting of weakly interacting one-dimensional (1d) ribbons, made by tightly-bonded [Bi$_4$S$_6$] units in an herring-bone arrangement (see Figure 5.1). [128] Until now, the importance of this singular crystal structure for the band gap tunability and surface properties of nanocrystals has been neglected. A deep knowledge of electron and hole recombination mechanisms
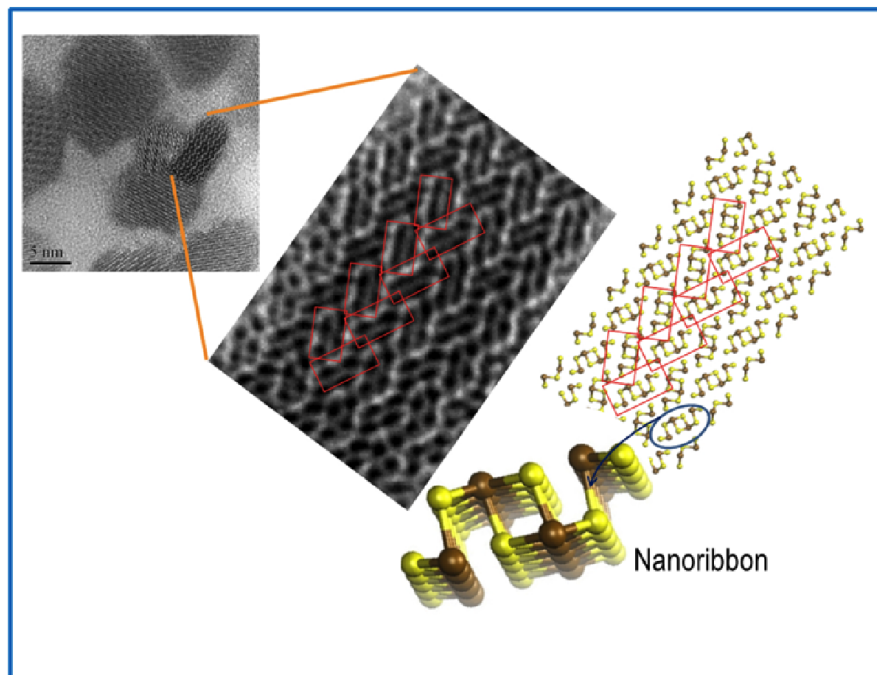
Figure 5.1: *HR-TEM image of Bi$_2$S$_3$ nanocrystals. The orthorhombic crystal structure is formed by the assembling of atomic ribbons. In the nanocrystal shown in the enlarged image, the nanoribbon axis is along the [001] crystallographic direction and perpendicular to the figure plane. Ribbons are arranged in a herring-bone motif, as highlighted by the red rectangles.*

at play in colloidal nanocrystals is also of crucial importance for successful exploitation of these materials in optoelectronic devices. [124] Photoexcited electrons and holes can quickly relax to the lowest and highest quantized levels of the conduction and valence bands, respectively. However, photo-carriers can be also captured by intragap trap levels, whose contribution to charge transport is quite limited. [66, 129]

Engineering of surface traps to control recombination rate is critical for the design of sensitive and fast photoconductive detectors, while suppression of nonradiative recombinations and charge trapping is of primary importance in solar cells. [64, 130, 131] There exists an extensive literature in semiconductor nanocrystals dedicated to the investigation of the relaxation dynamics of photoexcitations, to reveal the presence of carrier trap states, their energy and characteristic lifetimes, and their connection with surface properties. [3, 124, 129, 132–137]

Apart from an early report in Bi_2S_3 nanocrystals with band gap at 1.7 eV, [138] to the best of our knowledge, no systematic investigation of the excited-state dynamics in bismuth sulfide has been reported until now.

5.1.1 Synthesis of colloidal Bi2S3 nanocrystals

Bi_2S_3 colloidal nanocrystals were synthesized by an organometallic synthesis in the presence of oleic acid as capping agent.[1] [105, 130] The role of different synthesis parameters are extensively investigate, such as the injec-

---

[1]Synthesis of nanocrystals and morphological analysis was realized by Dipartimento di Scienze Chimiche e Geologiche, Universita degli Studi di Cagliari by R. Piras, C. Cannas, M. Mureddu, A. Ardu, G. Ennas and A. Musinu.

tion temperature of sulfur precursor, T_j, (from 50 to 170 °C) and the reaction time (by 30 min to 6 h). Nanocrystals were purified by successive dispersion/reprecipitation and centrifugation steps in toluene/methanol and finally dispersed in anhydrous toluene.

5.1.2   Nanocrystal characterization.

The XRD patterns of the most representative samples obtained under stoichiometric conditions at 6 h with different injection temperature are reported in Figure 5.2. Bragg reflections indicate the presence of Bi$_2$S$_3$ with
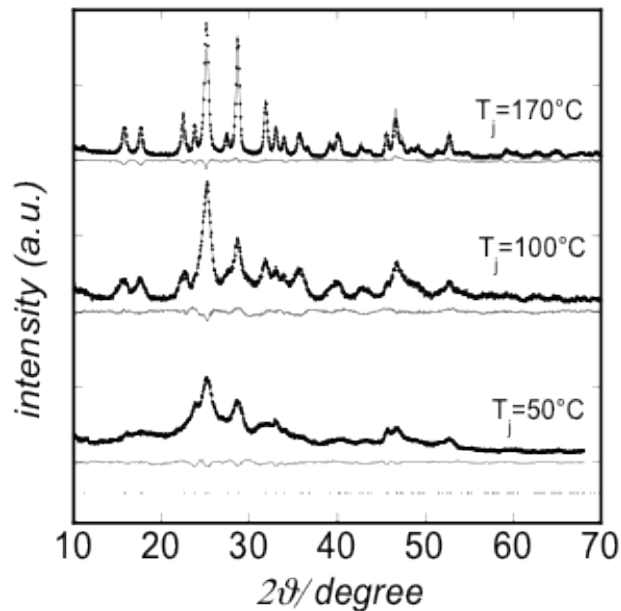
Figure 5.2: *XRD patterns of the samples obtained at 6 h for different injection temperatures (points) with Rietveld simulations (continuous) and residuals. Crystallographic reference data (ICSD n° 30775) at the bottom.*

orthorhombic structure as the unique phase in all patterns. The narrowing

of the peaks observed with increasing injection temperature, T_j, indicates an increase of the crystallite size. This trend is confirmed by Rietveld refinement of the XRD data.

Lattice parameters (a=1.114, b=1.129, c=0.3985 nm) are in good agreement with crystallographic data (ICSD n° 30775).

The fitted parameters ($<D>_{XRD}$) of the minor and major axes of nanocrystals), are reported in figure 5.3 together with the final R$_w$ (weighed pattern agreement index). In order to verify the effect of the reaction time, the re-

T_i (°C)	R_t (h)	$<D>_{XRD}$(nm)	$<D>_{XRD}$ (nm)	R_w (%)	$<D>_{TEM}$ (nm)	σ_{TEM} (%)	$<D>_{TEM}$ (nm)	σ_{TEM} (%)
Injection Temperature	Reaction Time	Major axis	Minor axis	Agreement index	Major axis		Minor axis	
170	½	26.4(5)	9.0(5)	13.2	25	(6)	13	(10)
170	6	26.1(5)	9.0(5)	8.8	25	(10)	13	(13)
100	6	-	8.7(5)	13.9	29	(14)	14	(19)
50	6	-	4.5(3)	7.5	7.5		3.6	

Figure 5.3: *Average crystallite size evaluated by Rietveld Analysis of XRD patterns with respective agreement index R_w% . Average particle size and polydispersity calculated by the size distributions reported in Fig. 5.4. For the sample obtained at T_j =50°C the $<D>_{TEM}$ values are calculated as an average around the first and second maxima of the double size distribution reported in Fig.5.4*

finement was also performed on the sample obtained after 1/2 h. The results show the formation of 9×26 nm anisometric single crystals (nanorods) both at 6 and 1/2 h, [139] indicating that the reaction time does not affect the nanocrystal size.

In table 5.3 (best fit in Figure 5.2) the evolution of the mean crystallite size with the injection temperature are also reported. The values obtained by the fit evidence that the decrease of the T$_j$ from 170 °C to 100 °C and 50

°C are in favor of the formation of an increasing number of isotropic single crystals. The reaction temperature represents therefore the key parameter in order to tune the Bi$_2$S$_3$ crystallite size. In order to better investigate the morphology and the crystallinity of the pure bismuthinite nanoparticles, TEM Bright and Dark Field images, and HRTEM images of the samples obtained at the different injection temperatures, together with particle size distributions calculated by Bright Field images, are reported in Figure 5.4. For all the samples, TEM images indicate that nanoparticles tend to self assemble in a monolayer on the TEM grid due to the presence of the capping agent (oleic acid) at nanoparticle surface, being the average nanoparticle distance of about 3 nm. It is necessary to take into account that the TEM Bright Field images give information about particle size and morphology, but the crystalline and/or amorphous/defective nature of the nanoparticles and of nanocrystal size have to be checked by Dark field mode and/or High resolution TEM.

TEM Bright and Dark Field images of the sample at T$_j$=170°C, reported in Figure 5.4(a), clearly show the formation of regular rod shaped nanoparticles of average length of 25 nm (10% polydispersity) and width of 13 nm (13% polydispersity) (figure 5.3). The brightness of the nanorods in the Dark Field image is clear evidence that most of them are single crystals, being the nanorod size equal in Bright and Dark Field mode, in good agreement with the average crystallite size values $<D>_{XRD}$ obtained by Rietveld analysis.

TEM Bright Field image of the sample at T$_j$=100°C (Figure 5.4(b) - 5.3) shows the presence of rod shaped particles with average sizes of 29 nm (14% polydispersity) and of 14 nm (19% polydispersity). The larger polydispersity
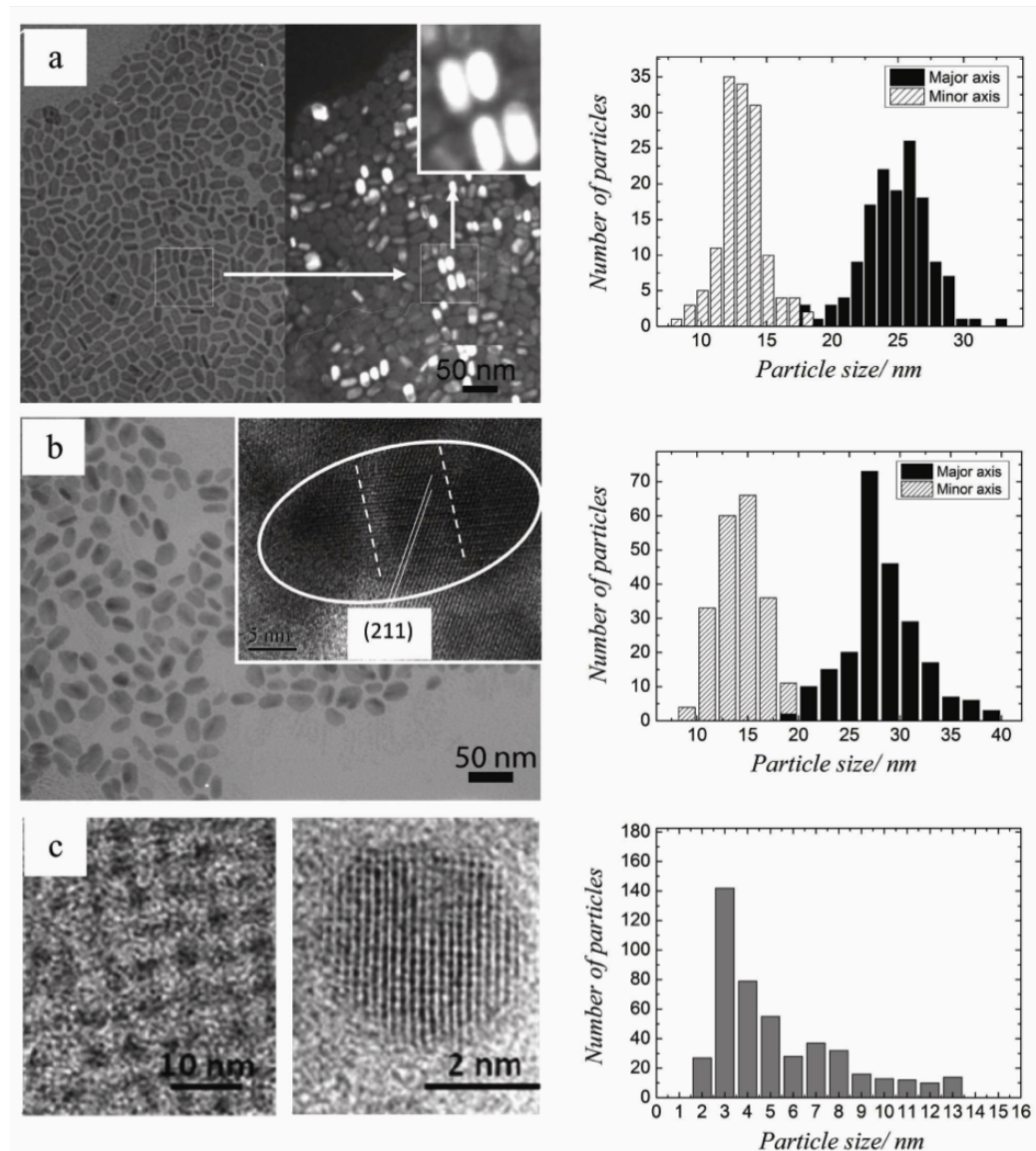
Figure 5.4: (a) TEM Bright and Dark Field images of $T_j = 170°C$ sample. (b) Bright Field image of $T_j = 100°C$ sample with HRTEM image (inset). (c) HRTEM images of the $T_j = 50°C$ sample. In the right side are reported the corresponding particle size distributions calculated by Bright Field images. For the $T_j=170$ and $100\,°C$ samples the size distribution of the minor and major axes of the nanorods are reported. For the $T_j = 50\,°C$ sample a double size distribution of quasi-spherical nanoparticles is calculated with two maxima centered at 3 and 7 nm respectively.

in comparison with the sample at T$_j$=170°C is consistent with a higher spread of nanoparticle sizes for samples obtained at lower injection temperature. The average particle size values obtained by TEM are similar at the two different injection temperatures.

However, for the sample at T$_j$=100°C they turn out to be three times larger in length than the average crystallite size values $<$D$>_{XRD}$ obtained by Rietveld analysis. This observation is confirmed by the HRTEM image in the inset of Figure 5.4(b) which shows in fact three nanocrystals assembling to form an iso-oriented nanorod.

HRTEM images of the sample at T$_j$=50°C indicate the presence of spherical nanoparticles with a double size distribution (Figure 5.4(c),5.3). The higher maximum indicates that most of them are small nanocrystals of about 3.6 nm, while the lower one indicate the presence of a low fraction of small nanorods of 7.5 nm in length. The average value calculated taking into account all the nanoparticles (4.8 nm) is in very good agreement with the values achieved by the Rietveld refinement of XRD data (4.5 nm).

5.2   Optical and electronic properties

According to spectroscopic data on single crystals of Bi$_2$S$_3$, the room temperature absorption spectrum near the optical gap is dominated by band-to-band transitions and a broad excitonic contribution. [139] The bandgap energy, E_g, was found to be at 1.443 eV and the exciton transition at 1.413 eV. The overall absorption spectra of Bi$_2$S$_3$ nanocrystals synthesized at T$_j$=50, 100 and 170 °C are reported in the inset of Figure 5.5.
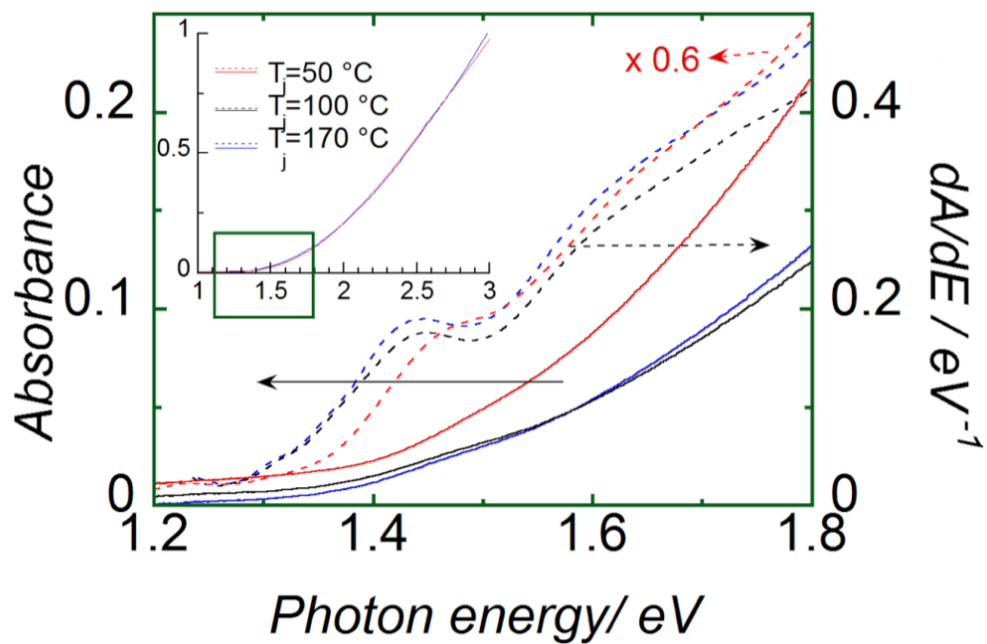
Figure 5.5: *Absorbance spectrum (continuous lines) and its first derivative (dashed lines) near the absorption edge of Bi$_2$S$_3$ nanocrystals in toluene dispersion synthesized at the injection temperatures, T_j= 50, 100 and 170 °C, respectively. The inset shows the whole UV-Vis-NIR spectra. For sake of comparison, spectra for Tj= 50, 100 °C are rescaled to the intensity of the spectrum for T_j= 170 °C.*

Linear optical absorption measurements were performed by means a Perkin Elmer Lambda 950 spectrophotometer, all spectra were recorded on toluene-based suspensions.

To investigate the effect of the nanocrystal size on the lowest energy electronic levels in more detail, the inset of Figure 5.5 reports a zoom near the edge of the absorption spectra together with their first derivatives; these latter can reveal weak optical contributions and minute differences in the spectra with enhanced sensitivity.

The shape of the absorbance near the optical threshold well reproduces the one reported for Bi$_2$S$_3$ single crystals, with a broad shoulder at 1.4-1.5 eV. The derivative spectrum shows that this shoulder is blue shifted by 30 meV in T$_j$= 50 °C nanocrystals. These spectroscopic data demonstrate that the quantum size effect is detectable but limited, despite the small dimension of the Bi$_2$S$_3$ nanocrystals. It is also worth comparing the observed shift with the confinement energies observed in nanocrystals with well-studied optical properties, such as CdSe, CdS or PbS and PbSe. For a particle size of   3.5 nm, the increase of the optical gap is several hundreds of meV, at least an order of magnitude higher than in Bi$_2$S$_3$. [140–143]

A theoretical quantitative assessment of the quantum confinement energies requires realistic models that take into account the atomistic nature of the nanocrystal. The size-dependence of the gap are investigated[2] by first-principles time-dependent density functional theory by focusing on the properties of the isolated ribbon and neglecting for simplicity the effect of

---

[2]Theoretical calculations were performed by CNR-IOM Cagliari, by Vasco Calzia and Alessandro Mattoni

the weak electronic interaction due to neighboring ribbons.

Undercoordinated sulfur and bismuth ions on the ribbon edges were saturated by H and OH groups, respectively. The calculated excitonic optical
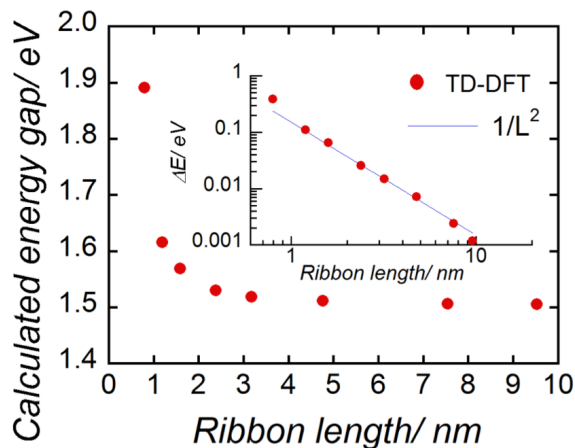

Figure 5.6: *Theoretical energy gap and energy gap shift (inset) of a single ribbon as a function of the ribbon length L. The lowest excitation energy was calculated through first principles methods in the framework of the time-dependent density functional formalism.*

gap of the ribbon is reported in Figure 5.6 as a function of its length L. The band edge saturates at 1.5 eV for long chains. The optical gap dependence on size follows a $1/L^2$ behavior. Theoretical data show that the gap tuning becomes perceptible only for ribbon length L around 3 nm. Blue shifts larger than one hundred of meV is achieved when L is smaller than 1 nm.

A few comments are required in order to compare the experimental and theoretical values of the band gap tuning in Bi$_2$S$_3$. We note that the lengths of ribbons forming a spherical nanocrystal of diameter D must be distributed in the range $0 < L < D$: the ribbon passing through the center of the nanoparticle has a maximal length L = D while peripheral ribbons must be

shorter. In other words, assuming an ensemble of spherical nanocrystals, all with the same diameter D, there exists an intrinsic distribution of ribbon lengths, as shown in the HR-TEM image of the spherical nanocrystal (T$_j$ = 50 °C) reported in Figure 5.7.

In a continuum model, the average value, <L>$_D$, can be easily shown to satisfy the equation <L>$_D$ = 2/3 d At the peak of the particle size distribution (3.5 nm), the average ribbon length is thus expected to be 2.3 nm. The expected shift of the absorption edge is calculated numerically in the continuum model from the knowledge of the dependence of the theoretical bandgap shift on L. In this size range, the calculated optical shift corresponds in good approximation with that calculated for a nanoribbon of length <L>$_D$. We find a blueshift of 30 meV, in good agreement with experiments. The possibility to achieve the challenging regime of strong confinement (<L>$_D$ ~ 1 nm, d ~ 1.5 nm) with useful energy shifts of several hundreds of meV is not, however, out of reach. According to previous experimental reports, spherical nanocrystals with diameters around 1.6 nm can be effectively synthesized by using a different synthesis approach; the observed experimental bandgap shift is consistent with the present theoretical model. [113]

In the following, we discuss the origin of the smaller Bi$_2$S$_3$ band gap shift with respect to other semiconductor nanocrystals, such as Cd and Pb chalcopyrites, of similar size. According to basic concepts of quantum mechanics, the energy shift of the lowest confined level in an infinite potential well is expected to scale with the well size (D) and the effective mass (m$_{eff}$) of the excitation, following the equation $\Delta E = Ch^2/(8m_{eff}D^2)$, where the constant C depends on the dimensionality of the confining potential. For a
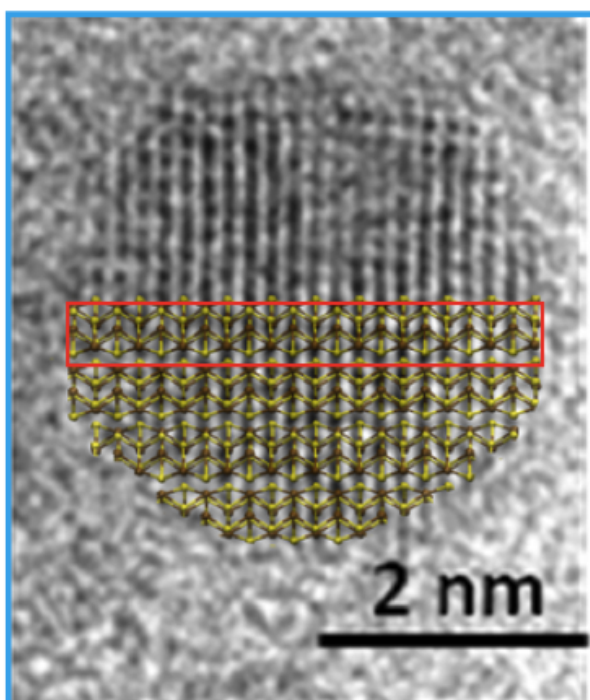
Figure 5.7: *HR-TEM image of a spherical nanocrystal (T_j=50 °C). The image shows that the Bi$_2$S$_3$ nanocrystal is made by the aggregation of nanoribbons of different lengths. The red rectangle highlights a single ribbon.*

1d-potential, suitable for Bi$_2$S$_3$ ribbons, C=1, while for a 3d-spherical well, which describes the case of most nanocrystals made by II-VI and III-V semi-conductors, C=4. [144, 145] This larger value accounts for the confinement energies along the three spatial dimensions (C=3 corresponds to the case of a particle in a 3d-square well). This analysis suggests two main reasons for the comparatively small band gap shift observed in Bi$_2$S$_3$ nanocrystals: (i) the 1d-character of the band-edge electronic states, and (ii) their heavy mass. [146, 147]

5.3   Transient absorption spectroscopy

Photoexcitation dynamics in Bi$_2$S$_3$ nanocrystals is monitored by using transient absorption spectroscopy, with the same set-up described in the previous chapter. [5, 52]

In this nonlinear technique, as described previously a laser pulse excites the sample to trigger the basic electronic processes taking place in optoelectronic devices following photon absorption. In a simple picture, the laser pulse promotes a hot electron above the minimum of the conduction band while leaving a hole in the valence band. Both charges relax to lower energy levels and eventually recombine. Transient populations of electronic levels and the strong interactions between photoexcited electron and hole pairs produce transitory modifications in the absorption spectrum, which can be monitored by measuring the transmission of a *white* probe pulse passing through the sample at variable delays. Differential transmission spectra are defined as $\Delta T/T = (T_{on} - T_{off})/T_{off}$, where T_{on} (T_{off}) is the transmitted

light in presence (absence) of the pump laser. $\Delta A = log(e)\Delta T/T$, where ΔA is the photoinduced variation of the nanocrystal absorbance.

5.3.1 Carrier relaxation and trapping in the 0.1 ps - 1 ns time scale

Nonlinear spectra are reported in Figure 5.8 as a function of pump-probe delays for T$_j$=170 °C nanocrystals. Similar nonlinear response was observed in samples grown at lower temperatures. At zero time, just after excitation, a photoinduced absorption band (PA; $\Delta T/T$<0, ΔA>0) is observed. This contribution disappears in about 300 ps leaving room to a broad bleaching band (PB; $\Delta T/T$>0, ΔA<0), i.e., a spectral region where the optical excitations created by the laser pulses give rise to an increase of light transmission.

The PB signal monotonically grows up within the experimental detection time window of 9 ns (Figure 5.9). The onset of both PA and PB occurs at the bandgap energy (arrow in Figure 5.8).

Photoinduced absorption: carrier-carrier interaction.

Following pump excitation, strong interactions between photoexcited electrons and holes induce a renormalization of the carrier energy levels. In bulk semiconductors, charge interaction leads to a redshift of the bandgap. [148] In absence of state-filling effects (t=0), i.e. before carrier relaxation to the band edge states, the interaction-induced differential transmission spectrum, $\Delta T/T$, is thus expected to be equal to -log(e) dA/dE ΔE_r, where ΔE_r is the energy level shift. The two spectra are shown in Figure 5.8. -log(e) dA/dE ΔE_r with $\Delta E_r = 18$ meV matches very well the transient PA spectrum in the
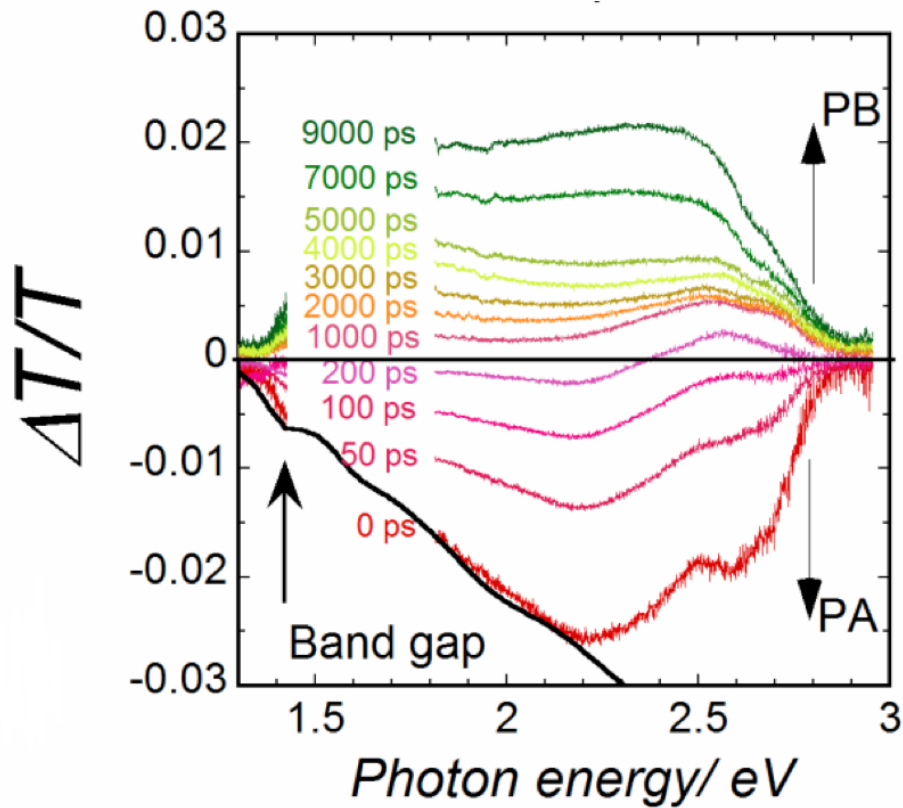
Figure 5.8: *Transient differential transmission spectra ($\Delta T/T$) of Bi$_2$S$_3$ nanocrystals (T_j = 170 °C) in toluene dispersion as a function of the delays between the excitation (hν= 3.16 eV) and probe laser pulses. Excitation pulse fluence: 0.17 mJ/cm^2. In the spectral range 1.4-1.8 eV, intensity instabilities of the white supercontinuum used as probe pulse do not allow measuring the transmission changes induced by the pump laser. Black curve: -log(e) dA/dE ΔE_r with ΔE_r = 18 meV.*
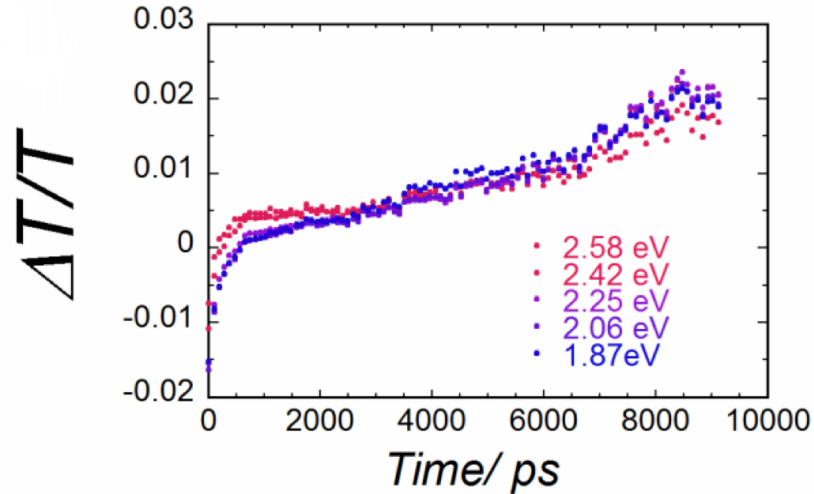
Figure 5.9: *Normalized transient Δ T signals at various photon energies versus pump-probe delay.*

1.3-2.2 eV spectral window, indicating that the redshift is the predominant interaction-induced effect up to 1 eV above the bandgap.

Photoinduced bleaching: free and trapped carriers.

Figure 5.10 illustrates the mechanisms of bleaching in a simple two-band model. Photoexcited electrons and holes relax to the bottom of the conduction band and top of the valence band, respectively. Each of these thermal relaxed populations inhibits optical transitions and contributes to make the nanocrystal transparent to light near the absorption edge. The transient PB signal at E_g thus monitors the buildup of the carrier population at the band edge. The unusually long rise time of PB observed in Bi$_2$S$_3$ nanocrystals provides evidence of a very slow energy relaxation of carriers, a process
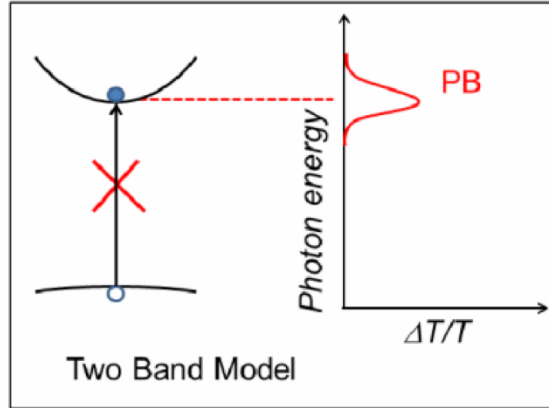
Figure 5.10: *Graphical representation of photobleaching in a band-to-band transition model. Crossed arrow stands for suppressed optical transitions due to empty (filled) electronic levels in the valence (conduction) band.*

that typically occurs in the ps-time scale. [38, 124] This slow process may be caused by an early relaxation of photoexcited carriers, e.g. electrons, into higher-energy conduction band minima, from which electrons eventually relax to the lowest energy minimum of the conduction band.

The complex topology of the Bi$_2$S$_3$ electronic band structure corroborates this hypothesis. [146] In the experiments reported in 5.8 and 5.9, Bi$_2$S$_3$ nanocrystals were excited by an average exciting pulse fluence of 0.17 mJ/cm^2. The photoinjected electron-hole pair density in the nanocrystals, n$_{eh}$, was assessed from the knowledge of the extinction coefficient per cation at the pump laser wavelength; [113] we found n$_{eh}$= 1.6 × 10^{20} cm^{-3}, corresponding to 0.020 excitations per Bi$_2$S$_3$ unit. The absence of any detectable photoluminescence signal, despite the fact that Bi$_2$S$_3$ is a direct semiconduc-

tor, [139] points out that only one type of carrier relaxes to the band edge states, while the other carrier is quickly trapped by intragap states.

The n-type photoconductive character of Bi$_2$S$_3$ indicates that holes were captured by traps, whose average number per nanocrystal, N$_t$, was comparable to or larger than the number of excited holes N$_h$. From the amplitude of the PB signal and pulse excitation fluence, we estimate that at least 30% of photoexcited electrons was thermalized in the lowest conduction band states (details are reported in appendix C).

In bulk, the n-type semiconducting properties of Bi$_2$S$_3$ are ascribed to the presence of sulphur vacancies. It was shown that bulk Bi$_2$S$_3$ exists with both sulphur excess and deficit. [106] For temperatures below 500 K, the upper trap density limit in the bulk results to be at least one order of magnitude smaller than the present estimate. It is therefore reasonable to conclude that the efficient hole trapping observed in Bi$_2$S$_3$ nanocrystals is mainly related to a partial passivation of surface states rather than to bulk sulphur vacancies. This deduction is supported by the observation of radiative emission in ligand-exchanged films, in which the improved surface passivation likely reduced trap density. [105] There exists a growing experimental evidence that the surfaces of metal-chalcogenide nanocrystals are metal-rich in presence of co-ordinating ligands bound covalently to cations, regardless the use of an excess of cations during synthesis. [149, 150]

For off-stoichiometric surfaces, the charge-orbital balance model provides a simple method to predict whether or not traps are formed. [137] In this framework, a nanocrystal has a clean optical gap if the number of overall available valence electrons is counterbalanced by the number of available va-

lence orbitals. Steric effects or an inappropriate coordination number of the
ligand can, however, prevent the ideal charge-orbital balance to be achieved,
leading to a high density of intragap states that are filled by the extra elec-
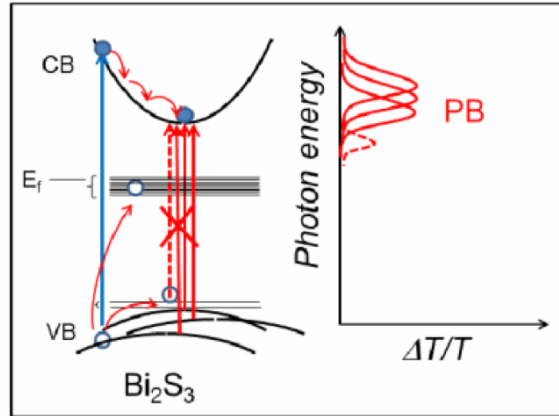trons supplied by unpassivated cations. [137] It is likely that this scenario

Figure 5.11: *Photobleaching dynamics in Bi$_2$S$_3$ nanocrystals. Intra-gap states are due to
deep and shallow traps. Following photoexcitation, almost all holes are quickly trapped,
while electrons relax to the bottom of the conduction band. E_f is the Fermi level, assumed
close to the top of the midgap band.*

also applies to Bi$_2$S$_3$ nanocrystals, in other words that nanocrystal surfaces
are Bi-rich with less than two oleic acid ligands per missing S anion. The
resulting energy level scheme is schematically reported in Figure 5.11.

The chemical potential is put close to the top of the midgap states, a
choice consistent with the charge-orbital balance model, the n-type photo-
conducting character of Bi$_2$S$_3$ and our spectroscopic data. The high number
of valence bands in Bi$_2$S$_3$ leads to the spectrally broad PB signal. [146] Under
the hypothesis that each trap level can capture two holes, $N_t \sim N_h/2$, and

all traps are located inside a 0.3 nm-thick shell at the nanocrystal surface, we provide a lower bound estimate of one midgap state every 16 surface Bi$_2$S$_3$ units, for a spherical nanocrystal whose size is fixed by matching the XRD nanocrystal volume (T$_j$=170 °C).

5.3.2 Carrier relaxation and trapping in the μs-s time scale

Trap lifetime is typically very long, often exceeding the nanosecond time-scale by several orders of magnitude. Our measurements of differential transmission with femtosecond laser pulses are limited in range to the longest optical delay we can introduce between pump and probe pulses, which is of the order of 10 ns.

Figure 5.12 shows the differential transmission spectrum $\Delta T/T$ using a continuous-wave probe that bypasses the time-range limitation.

In this experiment, the excitation laser are 0.4 μs-long pulses at 1 kHz repetition rate and 2.36 eV photon energy (second harmonic of a Nd:YLF laser B.M.I., 600). The cw-emission of a xenon lamp was used as a probe light source. Differential transmission ΔT was detected by a look-in amplifier (SRS, SR830 DSP) triggered by the output of the pump laser. The lifetime of the nonlinear signal was determined by measuring the temporal evolution of the differential transmitted signal of the cw-probe through an oscilloscope (Tektronix, TDS 3054 B) synchronized with the pump pulse train.

In contrast with the linear absorption spectrum, $\Delta T/T$ reveals intense narrow structures below and just above the gap, superimposed on a continuum extending up to $h\nu = 2$ eV.
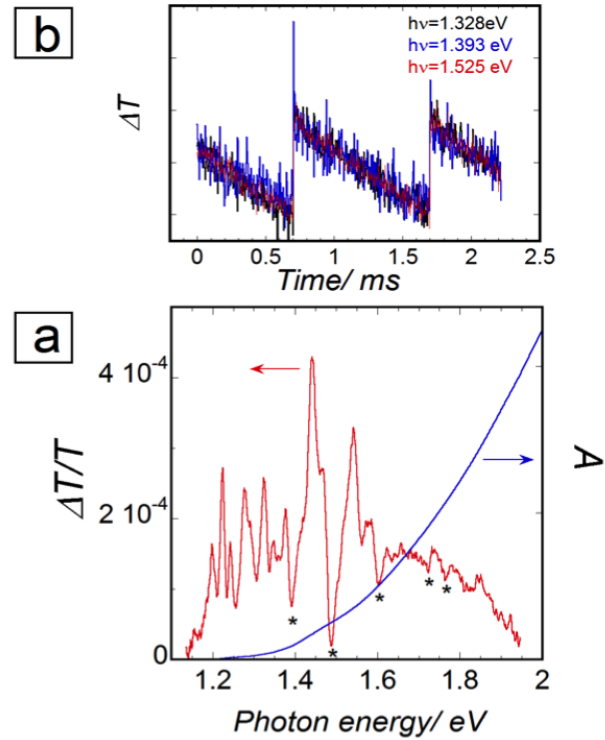
Figure 5.12: (a) Time-integrated differential transmission spectrum ($\Delta T/T$) in Bi2S3 nanocrystals (T=170 °C) in toluene dispersion induced by 1 kHz-pulse train (hν= 2.33 eV). Excitation pulse fluence: 0.16 mJ/cm^2. Stars denote a Fano-like interference pattern due to a coherent mixing between narrow-line transitions involving long-lived localized states and a continuum. Blue line: linear absorption spectrum. (b) Differential transmission transients versus pump-probe delays at three different photon energies.

The lifetime of the nonlinear signal was determined by measuring the temporal evolution of the differential transmitted signal of the cw-probe through an oscilloscope synchronized with pump pulse train (Figure 5.12(b)). The ΔT transient reveals a short component, which follows almost rigidly the laser pulse shape, and a contribution with a much longer lifetime, comparable with the time interval between two exciting pulses (1 ms). The ΔT kinetics is independent of the transition photon energy. The narrow lines observed in the $\Delta T/T$ spectrum reveal the existence of a set of long-lived shallow traps with energy up to 300 meV below the gap, as shown in Figure 5.11. The fact that these states are observed in the PB spectrum indicates that optical transitions from these states contribute to the tail absorption with a non-negligible oscillator strength.

These shallow states could be associated to ligands weakly bound to energetically unfavorable nanocrystal sites. According to atomistic simulations in metal-chalcogenides, these ligand-related states can have an appreciable oscillator strength and give rise to intragap states near the top of the valence band. [136] PB spectrum shows an unusual pattern: near and above the band gap narrow dips are observed. This behavior can be explained in the framework of Fano's theory of optical transition lineshape: coherent mixing of a narrow resonance with a continuum can result in various asymmetric resonance shapes, ranging from a Lorentzian peak on top of a weak background (Figure 5.12(a), photon energies below the gap), to an asymmetric s-shaped line and a spectral dip or anti-resonance behavior (Figure 5.12(a), photon energies near and above the band gap). Narrow peaks above Eg can be explained in terms of metastable, shallow excitons resulting from lower-energy

valence bands, consistently with the reported overcrowding of valence bands in Bi$_2$S$_3$. [146]

5.4   Conclusion

To conclude this chapter, I will briefly summarize the results obtained in the study of optical and electronic properties on Bi$_2$S$_3$ nanocrystals, a non-toxic and environmentally sustainable semiconductor with considerable interest of solar energy conversion.

We have shown that the intriguing small bandgap energy dependence on the nanocrystal size stems from the one-dimensional nature of the band-edge excitations and the weak band dispersion of Bi$_2$S$_3$. To achieve useful bandgap shifts, up to 0.5 eV, the ribbon lengths should be as short as 1 nm. As nanocrystals with a fixed size are formed by the aggregation of nanoribbons of different length, an average ribbon length of 1 nm corresponds to a spherical crystal size of 1.5 nm. Although challenging, this confinement regime is effectively accessible using suitable routes to Bi$_2$S$_3$ synthesis. [113]

We have demonstrated that a large fraction of photoexcited electrons are not trapped, while all holes are quickly captured by midgap states. Energy relaxation ends up with the excitation of shallow traps with μs to ms lifetimes. The overall carrier relaxation process is consistent with the assumption of a Bi-rich nanocrystal surface in which the passivation of dangling bonds by bulky oleic acid ligands is incomplete, leading to an intragap density of states in excess of 10^{20} cm^{-3}. Recent progress in the passivation of surface states in metal-chalcogen nanocrystals suggests there exist real margins for a

substantial reduction of trap density, [105] e.g., by developing a multi-ligand approach that better faces up to the complexity of nanocrystal surfaces. [151]

Chapter 6

Conclusion

Colloidal semiconductor nanocrystals are promising materials for applications in solution-processable optoelectronic devices including light-emitting diodes, photodetectors (see chapter 3), photocatalysts (see chapter 4) and photovoltaic cells (see chapter 5). Chemical synthesis enables refined control over dimension and shape of nanocrystals, allowing for unique functionalities and novel physical properties.

In this experimental work I investigated several optical and electronic properties of the nanocrystals, as a better understanding of these properties is of fundamental importance for the development of optoelectronic applications listed just above.

In the third chapter, variable pulse rate photoluminescence spectroscopy is applied to CdSe/CdS core/shell nanocrystals, in order to control and investigate dark and weakly emitting states in a model system, known for high luminescence quantum yield and reduced blinking. We identify contributions to the emission dynamics due to excitons created in nanocrystals with

charged cores and with active charge traps. We measure lifetimes of single charges in nanocrystals and highlight different trap dynamics. We demonstrate that dark and weakly emitting states, originating both from charges or traps, can be reversibly turned on and off by light. In the case of carrier traps, we speculate that light can indirectly induce a reversible local reorganization of capping molecules on the nanocrystal surface.

We think that this work is of fundamental support to understand and reduce the phenomena of instability of light emission from nanocrystals in all those applications that require a high density of excitation or under continuous illumination.

In the fourth chapter, ultrafast optical spectroscopy is applied to CdSe/CdS octapod nanocrystals decorated with platinum (Pt) nanoparticles, both a selective tipping and a non-selective surface coverage are investigated. In particular femtosecond transient absorption is employed to correlate the dynamics of optical excitations with the nanocrystal morphology. We investigate the consequences of different decorations on photophysical properties, focusing on capture of photoexcited electrons by Pt domains, the initial step of photocatalytic reactions. We find two regimes for capture of photoexcited electrons: a slow capture after energy relaxation in the semiconductor, occurring in tipped nanocrystals and resulting in large spatial separation of charges, and an ultrafast capture of hot electrons occurring in nanocrystals covered in Pt, where charge separation happens faster than energy relaxation and Auger recombination.

Besides the relevance for fundamental materials science and control at the nanoscale, our nanocrystals may be employed in solar photocatalysis.

In the fifth chapter, time-resolved differential transmission spectroscopy techniques are applied to bismuth sulfide (Bi_2S_3) nanocrystals, a promising compound semiconductor non-toxic and environmentally sustainable. The large absorption cross-section and the direct band gap in the near infrared make Bi_2S_3 nanocrystal a very promising n-type semiconductor for solar energy conversion. Optical properties were investigated combining linear transmission spectroscopy with time-resolved differential transmission in the 0.1 ps-1 s time range to reveal states with ultrafast and slow kinetics.

We find in agreement with the n-type character of Bi_2S_3 that optically excited electrons relax down to conduction band states. Trapping of holes occurs in the sub-picosecond time scale, inhibiting radiative recombination. Shallow traps with transition energies up to 300 meV below the bandgap are observed to survive for milliseconds. The overall trap density is estimated in excess of 10^{20} cm^{-3}. The comparison of the estimated trap density with the expected density of sulphur vacancies, a well-known defect in bulk Bi_2S_3 , points out to their surface origin, even in the largest investigated nanocrystals. The efficient trapping of holes is consistent with the assumption that long oleic acid ligands are not able to passivate all trap sites in a Bi-rich nanocrystal surface, presumably due to steric effects.

This analysis suggests that a lower density of intragap states could be achieved by using the combination of ligands with reduced steric hindrance and different chemical affinity.

Appendix A

Single shot measurements

As a reference for variable pulse rate photoluminescence spectroscopy, we devise an experiment for nanocrystals in toluene dispersion where every laser pulse excites a fresh portion of sample. Nanocrystal dispersion is flowed
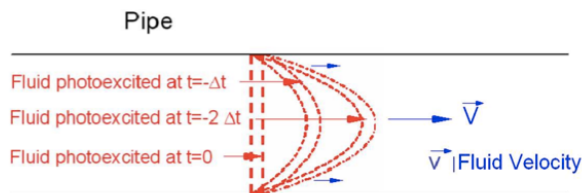
Figure A.1: *A scale cross-section of the cylindrical pipe used to flow the nanocrystal solution. The photoexcited region moves from left to right, ensuring that only a small fraction of nanocrystals, close to the walls of the tube, undergoes multi-pulse excitation;*

through a quartz cylindrical tube, 1 mm in diameter, by means of a peristaltic pump. The resulting flow regime is laminar, with Reynolds number ≈ 200 and mean drift velocity

$< v >= 130mm/s$. According to fluid mechanics, the nanocrystal motion

in the pipe has the parabolic velocity profile sketched in Fig. A.1. The solution in direct contact with the wall is still, while the maximum speed, $2 < v >$, is reached at the center of the tube. In this region, resulting fluid displacement between two consecutive laser pulses is four times the laser spot size, $\phi = 130\mu m$. We calculate that the regime of single pulse excitation is achieved in most (93%) of the photoexcited volume. Only 3, 1.5 and 0.08% of the dots undergo two-, three- and four-pulse excitation, respectively. Attenuation of the photoluminescence emitted from the thin layer close to pipe surfaces is provided by confocal light collection of the streak-camera through optical spatial filtering. Light emission properties of nanocrystals are investigated as a function of laser fluence. The average number of injected excitons per pulse in each nanocrystals, N, ranges from 0.01 to 500.

The transient luminescence signal emitted at the nanocrystal band edge is reported in Fig. A.2(a) for three values of laser intensity, corresponding to N=0.045, 0.45 and 89, representative of: i) the low excitation regime, achieved for $N \ll 0.1$, with the majority of nanocrystals in the ground state, and only a few excited with a single electron-hole pair; ii) the intermediate excitation regime, with the quantum dots in the ground, exciton or biexciton state, with a negligible probability of finding higher order multiexciton states; iii) the high excitation regime, in which $N \gg 1$ and almost all nanocrystals are multiply excited with average multiplicity N. For $N \ll 0.1$, photoluminescence decays exponentially, with a characteristic time of 21 ns, equal to the exciton lifetime τ_x. In the intermediate excitation regime, a sub-nanosecond decay emerges on top of the long-lived exciton signal. At higher injection
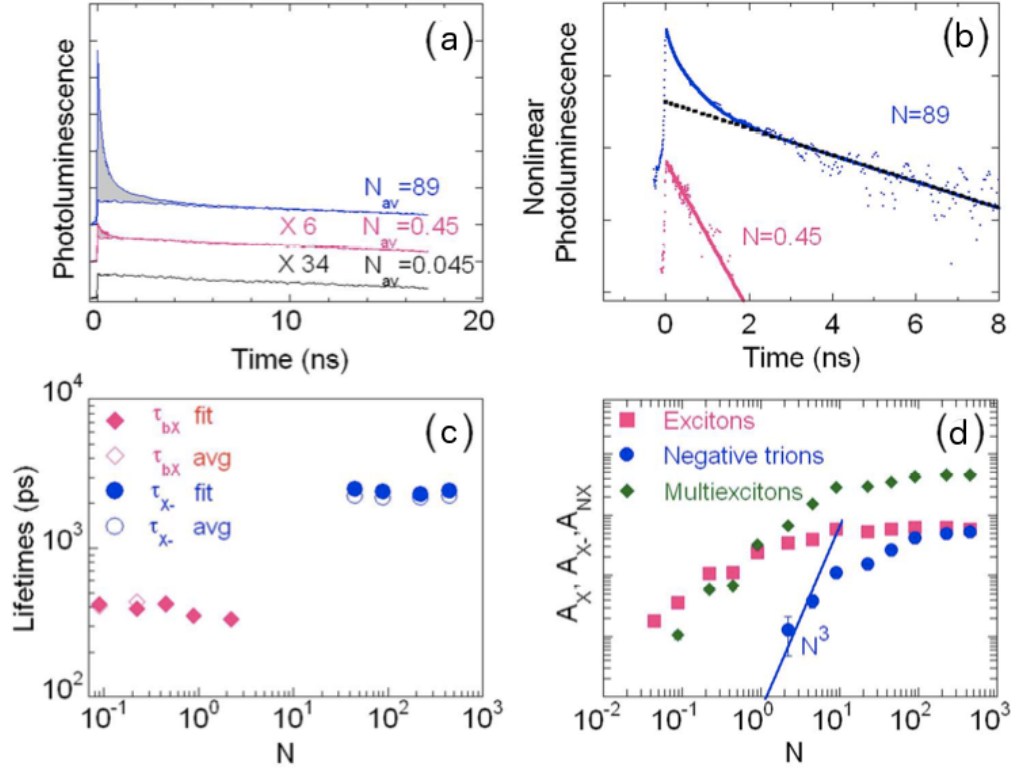
Figure A.2: *a) Transient photoluminescence signal for three different excitation levels. Gray regions between the photoluminescence curves and the decaying baseline highlight the nonlinear contribution arising from multiexcitons and charge-split states. The baseline is provided by the photoluminescence recorded at N =0.045, rescaled to match the long-time signal at the fixed excitation level. Panel b) shows the nonlinear transients (dots), i.e., the difference between the photoluminescence signal at a set N and the baseline, and the corresponding fitting curves (continuous lines). The slowly decaying contribution due to charge- split states is also reported. Panel c) shows the negative trion lifetime, τ_{X_-}, estimated through an exponential fit (full red squares) to the long time signal (T > 2 ns) in the high excitation regime (N > 10). τ_{X_-} is compared with the mean lifetime of the nonlinear signal (empty red squares), evaluated for delay times between 2 and 8 ns. τ_{bX} is biexciton lifetimes, estimated through an exponential fit of the nonlinear photoluminescence in the low and moderate excitation regime (full blue circles). τ_{bX} is compared with the mean lifetime of the nonlinear signal (empty blue circles), (T< 2 ns). Panel d) shows the contributions of negative trions and excitons to the nonlinear photoluminescence as a function of the laser fluence. The straight line represents a guide to the eye showing cubic power dependence.*

levels, the fast transient becomes the dominant contribution. In addition to this component, a further luminescence signal with a nanosecond decay transient appears.

Excitons, biexcitons and multiexcitons, including charged states, can radiatively decay emitting a photon at the optical gap, as a result of the optical transition from the lowest conduction energy level, $1S_e$, to the highest valence level, $1S_h$. Under impulsive excitation, the resulting band edge photoluminescence can be decomposed as the sum of the exciton signal plus the contribution from all other neutral and charged multiple exciton states.

The nonlinear photoluminescence (NLPL) is thus obtained by subtracting the single exciton decay curve, $A_x(t)$, from the overall PL intensity. The transient in the low excitation regime N=0.045 is taken as the reference function $A_x(t)$ up to a multiplicative constant, determined by matching the long-time behaviour of $A_x(t)$ and PL(t) for any fixed excitation level. This operation is justified by the fact that the exciton lifetime is at least one order of magnitude longer than the decay time of any other state involved.

The lifetime τ_{NLPL} of the NLPL in the medium excitation regime provides the most reliable estimate of the biexciton lifetime τ_{bX}. NLPL transients are fitted with a single exponential and the resulting values for $N < 4$ are reported in A.2(b). For $N > 0.5$, τ_{NLPL} decreases as the contribution of multiexciton states with shorter Auger lifetimes becomes more important. $\tau_{bX} = (0.41\pm0.03)ns$ is estimated as the average value of τ_{NLPL} for $N_{av} < 0.5$. The same approach is used to establish the lifetime of the long-lived contribution to the NLPL observed in the high excitation regime. The analysis is done for delays longer than 2 ns, when contributions from biexcitons and

multiexcitons are negligible.

The inset of A.2(c) reports the values of τ_{NLPL} estimated at the highest excitations featuring high signal-to-noise ratio. The long-lived state is assigned to states with reduced Auger recombination rates, negative trions. This attribution is consistent with the fact that the PL emission at these delay times is slightly shifted to the red, as expected for negative trions (see main text). $\tau_{X^-} = 2.4 \pm 0.1 ns$, about 6 times τ_{bX}, is estimated as the average value of τ_{NLPL}.

In the relaxation-time approximation, band edge photoluminescence following impulsive excitation can be decomposed as the sum, $\sum_i A_i e^{-t/\tau_i}$, of the emitted light intensity from all excited states. Contributions A_i to the PL signal from excitons (A_X) and trions (A_{X^-}) are reported in the inset of Fig. A.2(d) as a function of the mean number N of excitons injected into nanocrystals. At any laser fluence, A_X is taken equal to the rescaled exciton function $A_X(t = 0) = A_0$ shown in Fig. A.2(a). A least square fit to the NLPL with the sum of three exponentials measures the relative contributions of negative trions, biexcitons, and fast-decaying multiexcitons states of order $m > 2$.

Representative fit curves are reported in Fig. A.2(b). Lifetimes of biexcitons and trions are fixed to the experimental values τ_{bX} and τ_{X^-}, independently determined. The free parameters are A_{bX}, A_{mX} (introduced for accounting emission from multiexciton states with $m > 2$) and A_{X^-}. A lifetime of 100 ps is used for multiexciton states. Assessments of A_X and $A_{bX} + A_{MX}$ are unaffected by this latter choice. Reliability of fits is checked by analysing the noise pattern. Residuals of all fits to experimental data has

a root mean square fluctuations limited by the intrinsic noise of the nonlinear technique, in large part due to the fact that the nonlinear signal is obtained as difference between the overall photoluminescence signal and the excitonic contribution.

According to the discussion reported in the main text concerning the saturation behaviour of the charge population, nanocrystal photoionization is primarily triggered by Auger processes. We use the single-pulse experimental data, in which pulse-to-pulse charge accumulation is precluded, to extract the probability that the Auger nonradiative decay of a multiexciton state leads to the formation of a band-edge trion state. In order to observe photon emission from a trion state in a single-pulse experiment, we should at least consider a tri-exciton state ($m = 3$, τ_X). Auger relaxation of a biexciton state can in fact only lead to a non-radiative charged state with just a single electron (hole) in the nanocrystal core. The probability to excite a tri-exciton state is provided by the Poisson statistics $p(3, N) \sim N^3/6$. τ_{Xs} mainly relax through Auger processes; if η is the production yield of negative trions per Auger process, the photoluminescence emission intensity A_{X-} reads:

$$A_{x_-} = K_{sc} \frac{\tau_{rad,X}}{\tau_{rad,X_-}} \frac{N^3}{6} \eta \qquad (A.1)$$

where the scaling factor, k_{sc}, takes into account the exciton radiative decay rate and the detection sensitivity of the experimental set-up and satisfies the relation $A_X = k_{sc}N$; $\tau_{radX,}/\tau_{radX,}$ accounts for the different radiative decay times of excitons and trions. According to the statistical model of non-interacting electrons and holes, $\tau_{rad,X}/\tau_{rad,X-} = 2$. k_{sc} is measured by fitting the low-fluence photoluminescence intensity versus pulse fluence. $\eta = 1.4 \times 10^{-3}$ is obtained by fitting the dependence of A_{X-} on N, as reported

in Fig.A.2(c). At the pulse repetition frequency $\nu = 4MHz$, the population of negative trions is in a quasi-steady state, and well below saturation, n_- reads:

$$n_- \cong p(2,N)\nu\eta\tau_-n_{sat} \cong \frac{N^2}{2}\nu\eta\tau_-n_{sat} \tag{A.2}$$

For the parameter α, defined according to equation 3.1 reported in chapter3, we therefore obtain: $\alpha = \eta/2 = 7 \times 10^{-4}$.

Appendix B

Rate equation model used to quantitatively analyze variable pulse rate photoluminescence data.

In the following, we briefly outline the theoretical rate equation model used to quantitatively analyze variable pulse rate photoluminescence data. We assume that each laser pulse excites an ensemble of nanocrystals consisting of: neutral quantum dots in the electronic ground state, negatively or positively charged nanocrystals and nanocrystals with active surface states able to trap hot and thermal photoexcited charges. Populations of these quantum dot states, n_0, n_-, n_+, n_h, and n_{th}, respectively, satisfy the conservation rule $n_0 + n_- + n_+ + n_h + nt_h = 1$. Each n_i depends on the pulse fluence and repetition rate, and slowly varies with time. Absorption of one or more

photons from each laser pulse excites a transient population of excitons (n_X), trions (n_{X-} and n_{X+}), neutral and charged multi-excitons. Exciton states of higher multiplicity (m>2) quickly annihilate via fast Auger process to form band-edge two-exciton or charged exciton states. The resulting burst of band-edge photoluminescence is characterized by a prompt signal A_0, which is a linear combination of the populations of the initial nanocrystal states, n_i:

$$A_0 = k_{sc} \left\{ p(1, N)n_0 + p(1, N)n_{th} + \frac{\tau_{rad,X}}{\tau_{rad,X_-}} p(1, N)n_- + \frac{\tau_{rad,X}}{\tau_{rad,X_+}} p(1, N)n_+ + \right.$$
$$\left. + \sum_{m=2}^{\infty} p(m, N) \left[(n_0 + n_{th})\frac{\tau_{rad,X}}{\tau_{rad,bX}} + n_- \frac{\tau_{rad,X}}{\tau_{rad,bX_-}} + n_+ \frac{\tau_{rad,X}}{\tau_{rad,bX_+}} \right] \right\} \qquad \text{(B.1)}$$

The first term in equation B.1 gives the intensity of the light emitted from neutral, trap-free nanocrystals, which is proportional to the population n_0 and the probability p(1,N) to excite a single exciton, provided by the Poisson distribution p(m,N), where N is the average number of electron-hole pairs excited per quantum dot and m electron-hole pairs are excited in a single nanocrystal. The scaling factor, k_{sc}, takes into account the exciton radiative decay rate and the detection sensitivity of the experimental set-up.

Similarly, the second term provides the emission signal from neutral quantum dots with thermal-charge traps. The third and fourth terms concern the photoluminescence intensity of trion states created in charged nanocrystals. The fifth term describes emission from neutral and charged biexcitons states.

The ratios $\tau_{rad,X}/\tau_{rad,bX}$, $\tau_{rad,X}/\tau_{rad,bX_-}$, $\tau_{rad,X}/\tau_{rad,bX_+}$, $\tau_{rad,X}/\tau_{rad,X_-}$ and $\tau_{rad,X}/\tau_{rad,X_+}$ are set, respectively, to 4, 6, 6, 2 and 2, according to the statistical model of non-interacting electrons and holes, which provides results in good agreement with the available experimental data in CdSe/CdS core/shell

nanocrystals. [53] Nanocrystals with hot-charge trap states do not contribute to the photoluminescence signal. The amplitude of the long-lived emission is generated in trap-free neutral quantum dots n_0 can be expressed as:

$$A_x = k_{sc} \left[\sum_{m=1}^{\infty} p(m, N) \right] n_0 = k_{sc} \left[\sum_{m=1}^{\infty} p(m, N) \right] (1 - n_- - n_+ - n_{th} - n_h)$$
(B.2)

The statistical factor takes into account that electron-hole pair states with $m \geq 2$ nonradiatively relax to the single-exciton state and thus also contribute to the long-decaying signal. At low pulse intensities (N<0.03 excitons per dot), experimental data show that only the long-lived single- exciton emission was detected ($A_0 \cong A_X$) and the photoluminescence signal scales linearly with the injected electron-hole pairs.

Populations n_i are assessed from equations A.1 and A.2 as follows. Firstly, linear fits to experimental data are performed to assess the scaling factor k_{sc} for each experimental photoluminescence series. For $t > \tau_{bX} = 0.41$ns, the photoluminescence signal can be safely ascribed to radiative recombination of neutral and charged excitons alone, as the lifetimes of charged biexcitons as well as neutral and charged multiexcitons are shorter than τ_{bX} . We therefore determine the trion photoluminescence intensity $PL_{X_{-,+}}(t)$ by fitting the photoluminescence spectrum at time t=0.6 ns after laser pulse. The amplitude of trion photoluminescence contribution, $A_{X_{-,+}}$ is then obtained through the equation:$PL_{X_{-,+}}(t) = A_{X_{-,+}} e^{-t/\tau_{X_{-,+}}}$, with t=0.6 ns.

The steady-state population of the charged nanocrystal state n_- and n_+ are derived from the linear equation:

$$A_{X_{-,+}} = k_{sc} \frac{\tau_X}{\tau_{X_{-,+}}} \left[\sum_{m=1}^{\infty} p(m, N) \right] n_{-,+}$$
(B.3)

This relation results from the fact that negative trions can be created directly or indirectly via Auger relaxation of charged multiexciton states (m$\geq$2).

Once the total population of charged nanocrystals is known, linear equation B.2is used to assess the total population $n_t = n_h + n_{th}$ of trap states. From the knowledge of n_t and the experimental value of the prompt photoluminescence response A_0, we finally determine n_h and n_{th} by using linear equation B.1 and $n_t = n_h + n_{th}$.

Appendix C

Determination of the fraction of photoexcited electrons that thermalize in the lowest conduction band.

Here we briefly describe the calculations for determining of the fraction of photoexcited electrons that thermalize in the lowest conduction band. For n_{eh}= 1.6 × 10^{20} cm^{-3}, the probability, p_e, that the lowest conduction band state (involved in the optical transition at the optical gap E_g) was filled by thermalized photoexcited electrons is assessed from the PB signal (t=9 ns) via the equation $p_e = -\Delta A(E_g)/A(E_g)$. This number should be compared with the expected one, $p_{e,th}$, in the case that all photoexcited electrons were thermalized in the conduction band, i.e., in absence of electron trapping mechanisms. In order to determine $p_{e,th}$, we use the following model.

As nanocrystals synthesized at T_j=170 °C are very large and retain the electronic properties of bulk Bi_2S_3 , we consider a cubic nanocrystal of very large volume V. We assume that the number of excited electrons per each ribbon,
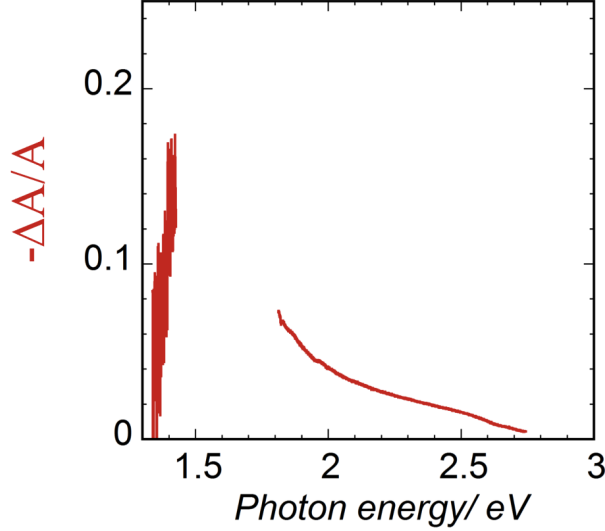
Figure C.1: *Relative variation of the optical absorbance, recorded at t=9 ns after excitation, as a function of the photon energy. Photoexcited electron density $n_e = 1.6 \times 10^{20} cm^{-3}$.*

$N_{e,r}$, is equal to the total number of excited electrons in the nanocrystal, $N_{e,r} = n_{eh}V$ ($n_{eh} = 1.6 \times 10^{20} cm^{-3}$), divided by the number of ribbons forming the nanocrystal. The average electron density per unit length is then calculated as $n_{e,r} = N_{e,r}/ < L >_D = 1.0 \times 10^8 cm^{-1}$.

We assume that the electron population is thermalized in the one-dimensional conduction band, characterized by an electron effective mass $m_e^* = 0.6 m_e$, at the lattice temperature T=300 K. According to the Fermi's statistics, the probability that an electron occupies the lowest energy state of the conduction band is $p_{e,th}$=0.47. Figure C.1 shows $-\Delta A(E)/A(E)$ as a func-

tion of the photon energy E; for E= E_g, -ΔA(Eg)/A(Eg)$\sim$0.15. Bearing in mind that the PB is still increasing at t=9 ns after excitation [the time at which we have assessed -ΔA(Eg)/A(Eg)], we conclude that at least a fraction $p_e/p_{e,th} = [-\delta A(Eg)/A(Eg)]/p_{e,th} \sim 0.32$ of photoexcited electrons were thermalized in the lowest conduction band.

Acknowledgments

List of Figures

Bibliography

[1] M. Faraday, "The bakerian lecture: experimental relations of gold (and other metals) to light," *Philosophical Transactions of the Royal Society of London*, vol. 147, pp. 145–181, 1857.

[2] E. R. Leite and C. Ribeiro, *Crystallization and growth of colloidal nanocrystals.* Springer, 2012.

[3] M. Saba, M. Aresti, F. Quochi, M. Marceddu, M. A. Loi, J. Huang, D. V. Talapin, A. Mura, and G. Bongiovanni, "Light-induced charged and trap states in colloidal nanocrystals detected by variable pulse rate photoluminescence spectroscopy," *ACS nano*, vol. 7, no. 1, pp. 229–238, 2012.

[4] D. V. Talapin, R. Koeppe, S. Götzinger, A. Kornowski, J. M. Lupton, A. L. Rogach, O. Benson, J. Feldmann, and H. Weller, "Highly emissive colloidal cdse/cds heterostructures of mixed dimensionality," *Nano Letters*, vol. 3, no. 12, pp. 1677–1681, 2003.

[5] M. Marceddu, M. Saba, F. Quochi, A. Lai, J. Huang, D. V. Talapin, A. Mura, and G. Bongiovanni, "Charged excitons, auger recombination

and optical gain in cdse/cds nanocrystals," *Nanotechnology*, vol. 23, no. 1, p. 015201, 2012.

[6] B. G. Streetman and S. Banerjee, *Solid state electronic devices*, vol. 4. Prentice Hall New Jersey, 2000.

[7] V. I. Klimov, *Semiconductor and metal nanocrystals: synthesis and electronic and optical properties*. CRC Press, 2003.

[8] Y. Yin and A. P. Alivisatos, "Colloidal nanocrystal synthesis and the organic–inorganic interface," *Nature*, vol. 437, no. 7059, pp. 664–670, 2004.

[9] A. Rogach, *Semiconductor Nanocrystal Quantum Dots: Synthesis, Assembly, Spectroscopy and Applications*. Springer, 1st ed ed., 2010.

[10] D. V. Talapin, J.-S. Lee, M. V. Kovalenko, and E. V. Shevchenko, "Prospects of colloidal nanocrystals for electronic and optoelectronic applications," *Chemical reviews*, vol. 110, no. 1, pp. 389–458, 2009.

[11] M. Nirmal, B. Dabbousi, M. Bawendi, J. Macklin, J. Trautman, T. Harris, and L. Brus, "Fluorescence intermittency in single cadmium selenide nanocrystals," *Nature*, vol. 383, no. 6603, pp. 802–804, 1996.

[12] K. Shimizu, R. Neuhauser, C. Leatherdale, S. Empedocles, W. Woo, and M. Bawendi, "Blinking statistics in single semiconductor nanocrystal quantum dots," *Physical Review B*, vol. 63, no. 20, p. 205316, 2001.

[13] J. J. Peterson and T. D. Krauss, "Fluorescence spectroscopy of single lead sulfide quantum dots," *Nano letters*, vol. 6, no. 3, pp. 510–514, 2006.

[14] S. Wang, C. Querner, M. D. Fischbein, L. Willis, D. S. Novikov, C. H. Crouch, and M. Drndic, "Blinking statistics correlated with nanoparticle number," *Nano letters*, vol. 8, no. 11, pp. 4020–4026, 2008.

[15] P. Spinicelli, S. Buil, X. Quelin, B. Mahler, B. Dubertret, and J.-P. Hermier, "Bright and grey states in cdse-cds nanocrystals exhibiting strongly reduced blinking," *Physical review letters*, vol. 102, no. 13, p. 136801, 2009.

[16] C. H. Crouch, O. Sauter, X. Wu, R. Purcell, C. Querner, M. Drndic, and M. Pelton, "Facts and artifacts in the blinking statistics of semiconductor nanocrystals," *Nano letters*, vol. 10, no. 5, pp. 1692–1698, 2010.

[17] M. Ye and P. C. Searson, "Blinking in quantum dots: The origin of the grey state and power law statistics," *Physical Review B*, vol. 84, no. 12, p. 125317, 2011.

[18] M. A. Osborne and S. F. Lee, "Quantum dot photoluminescence activation and decay: Dark, bright, and reversible populations in zns-capped cdse nanocrystals," *Acs Nano*, vol. 5, no. 10, pp. 8295–8304, 2011.

[19] E. A. Riley, C. M. Hess, and P. J. Reid, "Photoluminescence intermittency from single quantum dots to organic molecules: Emerging

themes," *International journal of molecular sciences*, vol. 13, no. 10, pp. 12487–12518, 2012.

[20] X. Brokmann, E. Giacobino, M. Dahan, and J. Hermier, "Highly efficient triggered emission of single photons by colloidal nanocrystals," *Applied Physics Letters*, vol. 85, no. 5, pp. 712–714, 2004.

[21] B. Mahler, P. Spinicelli, S. Buil, X. Quelin, J.-P. Hermier, and B. Dubertret, "Towards non-blinking colloidal quantum dots," *Nature materials*, vol. 7, no. 8, pp. 659–664, 2008.

[22] Y. Chen, J. Vela, H. Htoon, J. L. Casson, D. J. Werder, D. A. Bussian, V. I. Klimov, and J. A. Hollingsworth, ""giant" multishell cdse nanocrystal quantum dots with suppressed blinking," *Journal of the American Chemical Society*, vol. 130, no. 15, pp. 5026–5027, 2008.

[23] P. Spinicelli, B. Mahler, S. Buil, X. Quélin, B. Dubertret, and J.-P. Hermier, "Non-blinking semiconductor colloidal quantum dots for biology, optoelectronics and quantum optics," *ChemPhysChem*, vol. 10, no. 6, pp. 879–882, 2009.

[24] X. Wang, X. Ren, K. Kahen, M. A. Hahn, M. Rajeswaran, S. Maccagnano-Zacher, J. Silcox, G. E. Cragg, A. L. Efros, and T. D. Krauss, "Non-blinking semiconductor nanocrystals," *Nature*, vol. 459, no. 7247, pp. 686–689, 2009.

[25] W. Qin, R. A. Shah, and P. Guyot-Sionnest, "Cdses/zns alloyed nanocrystal lifetime and blinking studies under electrochemical control," *ACS nano*, vol. 6, no. 1, pp. 912–918, 2011.

[26] A. L. Efros and M. Rosen, "Random telegraph signal in the photolumi-nescence intensity of a single quantum dot," *Physical Review Letters*, vol. 78, no. 6, p. 1110, 1997.

[27] D. E. Gomez, J. van Embden, P. Mulvaney, M. J. Fernée, and H. Rubinsztein-Dunlop, "Exciton- trion transitions in single cdse–cds core–shell nanocrystals," *Acs Nano*, vol. 3, no. 8, pp. 2281–2287, 2009.

[28] J. Zhao, G. Nair, B. R. Fisher, and M. G. Bawendi, "Challenge to the charging model of semiconductor-nanocrystal fluorescence inter-mittency from off-state quantum yields and multiexciton blinking," *Physical review letters*, vol. 104, no. 15, p. 157403, 2010.

[29] S. Rosen, O. Schwartz, and D. Oron, "Transient fluorescence of the off state in blinking cdse/cds/zns semiconductor nanocrystals is not governed by auger recombination," *Physical review letters*, vol. 104, no. 15, p. 157404, 2010.

[30] Z. Xu and M. Cotlet, "Photoluminenscence blinking dynamics of col-loidal quantum dots in the presence of controlled external electron traps," *Small*, vol. 8, no. 2, pp. 253–258, 2012.

[31] J. Müller, J. Lupton, A. Rogach, J. Feldmann, D. Talapin, and H. Weller, "Monitoring surface charge migration in the spectral dy-namics of single cdse/ cds nanodot/nanorod heterostructures," *Physical Review B*, vol. 72, no. 20, p. 205339, 2005.

[32] R. Verberk, A. M. van Oijen, and M. Orrit, "Simple model for the power-law blinking of single semiconductor nanocrystals," *Physical Review B*, vol. 66, no. 23, p. 233202, 2002.

[33] D. E. Gómez, J. van Embden, J. Jasieniak, T. A. Smith, and P. Mulvaney, "Blinking and surface chemistry of single cdse nanocrystals," *Small*, vol. 2, no. 2, pp. 204–208, 2006.

[34] A. Issac, C. von Borczyskowski, and F. Cichos, "Correlation between photoluminescence intermittency of cdse quantum dots and self-trapped states in dielectric media," *Physical Review B*, vol. 71, no. 16, p. 161302, 2005.

[35] P. A. Frantsuzov and R. Marcus, "Explanation of quantum dot blinking without long-lived trap hypothesis," *arXiv preprint cond-mat/0505604*, 2005.

[36] J. Tang and R. Marcus, "Mechanisms of fluorescence blinking in semiconductor nanocrystal quantum dots," *The Journal of chemical physics*, vol. 123, no. 5, pp. 054704–054704, 2005.

[37] V. Klimov, A. Mikhailovsky, D. McBranch, C. Leatherdale, and M. Bawendi, "Quantization of multiparticle auger rates in semiconductor quantum dots," *Science*, vol. 287, no. 5455, pp. 1011–1013, 2000.

[38] S. L. Sewall, R. R. Cooney, K. E. Anderson, E. A. Dias, D. Sagar, and P. Kambhampati, "State-resolved studies of biexcitons and surface trapping dynamics in semiconductor quantum dots," *The Journal of chemical physics*, vol. 129, no. 8, pp. 084701–084701, 2008.

[39] M. Jones, S. S. Lo, and G. D. Scholes, "Quantitative modeling of the role of surface traps in cdse/cds/zns nanocrystal photoluminescence decay dynamics," *Proceedings of the National Academy of Sciences*, vol. 106, no. 9, pp. 3011–3016, 2009.

[40] C. Galland, Y. Ghosh, A. Steinbrück, M. Sykora, J. A. Hollingsworth, V. I. Klimov, and H. Htoon, "Two types of luminescence blinking revealed by spectroelectrochemistry of single quantum dots," *Nature*, vol. 479, no. 7372, pp. 203–207, 2011.

[41] A. A. Cordones, T. J. Bixby, and S. R. Leone, "Evidence for multiple trapping mechanisms in single cdse/zns quantum dots from fluorescence intermittency measurements over a wide range of excitation intensities," *The Journal of Physical Chemistry C*, vol. 115, no. 14, pp. 6341–6349, 2011.

[42] S. J. Kern, K. Sahu, and M. A. Berg, "Heterogeneity of the electron-trapping kinetics in cdse nanoparticles," *Nano letters*, vol. 11, no. 8, pp. 3493–3498, 2011.

[43] A. V. Malko, Y.-S. Park, S. Sampat, C. Galland, J. Vela, Y. Chen, J. A. Hollingsworth, V. I. Klimov, and H. Htoon, "Pump-intensity- and shell-thickness-dependent evolution of photoluminescence blinking in individual core/shell cdse/cds nanocrystals," *Nano letters*, vol. 11, no. 12, pp. 5213–5218, 2011.

[44] N. Durisic, A. G. Godin, D. Walters, P. Grütter, P. W. Wiseman, and C. D. Heyes, "Probing the "dark" fraction of core–shell quantum dots by

ensemble and single particle ph-dependent spectroscopy," *ACS nano*, vol. 5, no. 11, pp. 9062–9073, 2011.

[45] A. A. Cordones, T. J. Bixby, and S. R. Leone, "Direct measurement of off-state trapping rate fluctuations in single quantum dot fluorescence," *Nano letters*, vol. 11, no. 8, pp. 3366–3369, 2011.

[46] P. Kambhampati, "Hot exciton relaxation dynamics in semiconductor quantum dots: radiationless transitions on the nanoscale," *The Journal of Physical Chemistry C*, vol. 115, no. 45, pp. 22089–22109, 2011.

[47] T. D. Krauss and J. J. Peterson, "Quantum dots: A charge for blinking," *Nature Materials*, vol. 11, no. 1, pp. 14–16, 2011.

[48] L. A. Padilha, I. Robel, D. C. Lee, P. Nagpal, J. M. Pietryga, and V. I. Klimov, "Spectral dependence of nanocrystal photoionization probability: the role of hot-carrier transfer," *ACS nano*, vol. 5, no. 6, pp. 5045–5055, 2011.

[49] J. A. McGuire, M. Sykora, I. Robel, L. A. Padilha, J. Joo, J. M. Pietryga, and V. I. Klimov, "Spectroscopic signatures of photocharging due to hot-carrier transfer in solutions of semiconductor nanocrystals under low-intensity ultraviolet excitation," *ACS nano*, vol. 4, no. 10, pp. 6087–6097, 2010.

[50] M. Califano, "Off-state quantum yields in the presence of surface trap states in cdse nanocrystals: The inadequacy of the charging model to explain blinking," *The Journal of Physical Chemistry C*, vol. 115, no. 37, pp. 18051–18054, 2011.

[51] O. Schwartz, R. Tenne, J. M. Levitt, Z. Deutsch, S. Itzhakov, and D. Oron, "Colloidal quantum dots as saturable fluorophores," *ACS nano*, vol. 6, no. 10, pp. 8778–8782, 2012.

[52] M. Saba, S. Minniberger, F. Quochi, J. Roither, M. Marceddu, A. Gocalinska, M. V. Kovalenko, D. V. Talapin, W. Heiss, A. Mura, *et al.*, "Exciton–exciton interaction and optical gain in colloidal cdse/cds dot/rod nanocrystals," *Advanced Materials*, vol. 21, no. 48, pp. 4942–4946, 2009.

[53] V. Klimov, J. McGuire, R. Schaller, and V. Rupasov, "Scaling of multiexciton lifetimes in semiconductor nanocrystals," *Physical Review B*, vol. 77, no. 19, p. 195324, 2008.

[54] D. B. Tice, M. T. Frederick, R. P. Chang, and E. A. Weiss, "Electron migration limits the rate of photobrightening in thin films of cdse quantum dots in a dry n2 (g) atmosphere," *The Journal of Physical Chemistry C*, vol. 115, no. 9, pp. 3654–3662, 2011.

[55] D. P. Shepherd, K. J. Whitcomb, K. K. Milligan, P. M. Goodwin, M. P. Gelfand, and A. Van Orden, "Fluorescence intermittency and energy transfer in small clusters of semiconductor quantum dots," *The Journal of Physical Chemistry C*, vol. 114, no. 35, pp. 14831–14837, 2010.

[56] C. Wang, B. L. Wehrenberg, C. Y. Woo, and P. Guyot-Sionnest, "Light emission and amplification in charged cdse quantum dots," *The Journal of Physical Chemistry B*, vol. 108, no. 26, pp. 9027–9031, 2004.

[57] M. Califano, A. Franceschetti, and A. Zunger, "Lifetime and polarization of the radiative decay of excitons, biexcitons, and trions in cdse nanocrystal quantum dots," *Physical Review B*, vol. 75, no. 11, p. 115401, 2007.

[58] D. Oron, M. Kazes, I. Shweky, and U. Banin, "Multiexciton spectroscopy of semiconductor nanocrystals under quasi-continuous-wave optical pumping," *Physical Review B*, vol. 74, no. 11, p. 115333, 2006.

[59] A. Franceschetti and A. Zunger, "Optical transitions in charged cdse quantum dots," *Physical Review B*, vol. 62, no. 24, p. R16287, 2000.

[60] L.-W. Wang, M. Califano, A. Zunger, and A. Franceschetti, "Pseudopotential theory of auger processes in cdse quantum dots," *Physical review letters*, vol. 91, no. 5, pp. 564041–564044, 2003.

[61] X. Ji, D. Copenhaver, C. Sichmeller, and X. Peng, "Ligand bonding and dynamics on colloidal nanocrystals at room temperature: the case of alkylamines on cdse nanocrystals," *Journal of the American Chemical Society*, vol. 130, no. 17, pp. 5726–5735, 2008.

[62] E. Conca, M. Aresti, M. Saba, M. F. Casula, F. Quochi, G. Mula, D. Loche, M. R. Kim, L. Manna, A. Corrias, *et al.*, "Charge separation in pt-decorated cdse@ cds octapod nanocrystals," *Nanoscale*, 2013.

[63] M. D. Archer, A. J. Nozik, *et al.*, *Nanostructured and photoelectrochemical systems for solar photon conversion.* Imperial College Press London, 2008.

[64] E. H. Sargent, "Colloidal quantum dot solar cells," *Nature Photonics*, vol. 6, no. 3, pp. 133–135, 2012.

[65] P. V. Kamat, "Quantum dot solar cells. the next big thing in photovoltaics," *The Journal of Physical Chemistry Letters*, vol. 4, no. 6, pp. 908–918, 2013.

[66] M. Graetzel, R. A. Janssen, D. B. Mitzi, and E. H. Sargent, "Materials interface engineering for solution-processed photovoltaics," *Nature*, vol. 488, no. 7411, pp. 304–312, 2012.

[67] L. Carbone and P. D. Cozzoli, "Colloidal heterostructured nanocrystals: Synthesis and growth mechanisms," *Nano Today*, vol. 5, no. 5, pp. 449–493, 2010.

[68] A. Rogach, "Semiconductor nanocrystal quantum dots: synthesis, assembly, spectroscopy and applications, 2008."

[69] A. Vaneski, A. S. Susha, J. Rodríguez-Fernández, M. Berr, F. Jäckel, J. Feldmann, and A. L. Rogach, "Hybrid colloidal heterostructures of anisotropic semiconductor nanocrystals decorated with noble metals: synthesis and function," *Advanced Functional Materials*, vol. 21, no. 9, pp. 1547–1556, 2011.

[70] C. A. Grimes, O. K. Varghese, and S. Ranjan, *Light, water, hydrogen: the solar generation of hydrogen by water photoelectrolysis*. Springer, 2008.

[71] M. G. Walter, E. L. Warren, J. R. McKone, S. W. Boettcher, Q. Mi, E. A. Santori, and N. S. Lewis, "Solar water splitting cells," *Chemical reviews*, vol. 110, no. 11, pp. 6446–6473, 2010.

[72] Y. Tachibana, L. Vayssieres, and J. R. Durrant, "Artificial photosynthesis for solar water-splitting," *Nature Photonics*, vol. 6, no. 8, pp. 511–518, 2012.

[73] R. Van de Krol and M. Grèatzel, *Photoelectrochemical hydrogen production*, vol. 102. Springer, 2012.

[74] D. J. Milliron, S. M. Hughes, Y. Cui, L. Manna, J. Li, L.-W. Wang, and A. P. Alivisatos, "Colloidal nanocrystal heterostructures with linear and branched topology," *Nature*, vol. 430, no. 6996, pp. 190–195, 2004.

[75] H. Li, A. G. Kanaras, and L. Manna, "Colloidal branched semiconductor nanocrystals: State of the art and perspectives," *Accounts of chemical research*, 2013.

[76] S. Deka, K. Miszta, D. Dorfs, A. Genovese, G. Bertoni, and L. Manna, "Octapod-shaped colloidal nanocrystals of cadmium chalcogenides via "one-pot" cation exchange and seeded growth," *Nano letters*, vol. 10, no. 9, pp. 3770–3776, 2010.

[77] M. R. Kim, K. Miszta, M. Povia, R. Brescia, S. Christodoulou, M. Prato, S. Marras, and L. Manna, "Influence of chloride ions on the synthesis of colloidal branched cdse/cds nanocrystals by seeded growth," *ACS nano*, vol. 6, no. 12, pp. 11088–11096, 2012.

[78] R. Brescia, K. Miszta, D. Dorfs, L. Manna, and G. Bertoni, "Birth and growth of octapod-shaped colloidal nanocrystals studied by electron tomography," *The Journal of Physical Chemistry C*, vol. 115, no. 41, pp. 20128–20133, 2011.

[79] T. Mokari, E. Rothenberg, I. Popov, R. Costi, and U. Banin, "Selective growth of metal tips onto semiconductor quantum rods and tetrapods," *Science*, vol. 304, no. 5678, pp. 1787–1790, 2004.

[80] T. Mokari, C. G. Sztrum, A. Salant, E. Rabani, and U. Banin, "Formation of asymmetric one-sided metal-tipped semiconductor nanocrystal dots and rods," *Nature Materials*, vol. 4, no. 11, pp. 855–863, 2005.

[81] A. E. Saunders, I. Popov, and U. Banin, "Synthesis of hybrid cds-au colloidal nanostructures," *The Journal of Physical Chemistry B*, vol. 110, no. 50, pp. 25421–25429, 2006.

[82] S. E. Habas, P. Yang, and T. Mokari, "Selective growth of metal and binary metal tips on cds nanorods," *Journal of the American Chemical Society*, vol. 130, no. 11, pp. 3294–3295, 2008.

[83] L. Amirav and A. P. Alivisatos, "Photocatalytic hydrogen production with tunable nanorod heterostructures," *The Journal of Physical Chemistry Letters*, vol. 1, no. 7, pp. 1051–1054, 2010.

[84] M. Berr, A. Vaneski, A. S. Susha, J. Rodríguez-Fernández, M. Doblinger, F. Jackel, A. L. Rogach, and J. Feldmann, "Colloidal cds nanorods decorated with subnanometer sized pt clusters for photo-

catalytic hydrogen generation," *Applied Physics Letters*, vol. 97, no. 9, pp. 093108–093108, 2010.

[85] A. Figuerola, M. v. Huis, M. Zanella, A. Genovese, S. Marras, A. Falqui, H. W. Zandbergen, R. Cingolani, and L. Manna, "Epitaxial cdse-au nanocrystal heterostructures by thermal annealing," *Nano letters*, vol. 10, no. 8, pp. 3028–3036, 2010.

[86] M. J. Berr, A. Vaneski, C. Mauser, S. Fischbach, A. S. Susha, A. L. Rogach, F. Jäckel, and J. Feldmann, "Delayed photoelectron transfer in pt-decorated cds nanorods under hydrogen generation conditions," *Small*, vol. 8, no. 2, pp. 291–297, 2012.

[87] H. Baida, D. Mongin, D. Christofilos, G. Bachelier, A. Crut, P. Maioli, N. Del Fatti, and F. Vallée, "Ultrafast nonlinear optical response of a single gold nanorod near its surface plasmon resonance," *Physical review letters*, vol. 107, no. 5, p. 057402, 2011.

[88] D. Mongin, E. Shaviv, P. Maioli, A. Crut, U. Banin, N. Del Fatti, and F. Vallée, "Ultrafast photoinduced charge separation in metal–semiconductor nanohybrids," *ACS nano*, vol. 6, no. 8, pp. 7034–7043, 2012.

[89] B. P. Khanal, A. Pandey, L. Li, Q. Lin, W. K. Bae, H. Luo, V. I. Klimov, and J. M. Pietryga, "Generalized synthesis of hybrid metal–semiconductor nanostructures tunable from the visible to the infrared," *ACS nano*, vol. 6, no. 5, pp. 3832–3840, 2012.

[90] E. Shaviv, O. Schubert, M. Alves-Santos, G. Goldoni, R. Di Felice, F. Vallee, N. Del Fatti, U. Banin, and C. Sönnichsen, "Absorption properties of metal–semiconductor hybrid nanoparticles," *ACS nano*, vol. 5, no. 6, pp. 4712–4719, 2011.

[91] H. Schlicke, D. Ghosh, L.-K. Fong, H. L. Xin, H. Zheng, and A. P. Alivisatos, "Selective placement of faceted metal tips on semiconductor nanorods," *Angewandte Chemie International Edition*, vol. 52, no. 3, pp. 980–982, 2013.

[92] S. M. Kim, S. J. Lee, S. H. Kim, S. Kwon, K. J. Yee, H. Song, G. A. Somorjai, and J. Y. Park, "Hot carrier-driven catalytic reactions on pt–cdse–pt nanodumbbells and pt/gan under light irradiation," *Nano letters*, vol. 13, no. 3, pp. 1352–1358, 2013.

[93] J. Müller, J. Lupton, P. Lagoudakis, F. Schindler, R. Koeppe, A. Rogach, J. Feldmann, D. Talapin, and H. Weller, "Wave function engineering in elongated semiconductor nanocrystals with heterogeneous carrier confinement," *Nano letters*, vol. 5, no. 10, pp. 2044–2049, 2005.

[94] D. Steiner, D. Dorfs, U. Banin, F. Della Sala, L. Manna, and O. Millo, "Determination of band offsets in heterostructured colloidal nanorods using scanning tunneling spectroscopy," *Nano letters*, vol. 8, no. 9, pp. 2954–2958, 2008.

[95] M. G. Lupo, F. Della Sala, L. Carbone, M. Zavelani-Rossi, A. Fiore, L. Lüer, D. Polli, R. Cingolani, L. Manna, and G. Lanzani, "Ultrafast

electron- hole dynamics in core/shell cdse/cds dot/rod nanocrystals," *Nano letters*, vol. 8, no. 12, pp. 4582–4587, 2008.

[96] E. Yoskovitz, G. Menagen, A. Sitt, E. Lachman, and U. Banin, "Nanoscale near-field imaging of excitons in single heterostructured nanorods," *Nano letters*, vol. 10, no. 8, pp. 3068–3072, 2010.

[97] M. G. Lupo, F. Scotognella, M. Zavelani-Rossi, G. Lanzani, L. Manna, and F. Tassone, "Band-edge ultrafast pump–probe spectroscopy of core/shell cdse/cds rods: assessing electron delocalization by effective mass calculations," *Physical Chemistry Chemical Physics*, vol. 14, no. 20, pp. 7420–7426, 2012.

[98] L. T. Kunneman, M. Zanella, L. Manna, L. D. Siebbeles, and J. M. Schins, "Mobility and spatial distribution of photoexcited electrons in cdse/cds nanorods," *The Journal of Physical Chemistry C*, vol. 117, no. 6, pp. 3146–3151, 2013.

[99] N. J. Borys, M. J. Walter, J. Huang, D. V. Talapin, and J. M. Lupton, "The role of particle morphology in interfacial energy transfer in cdse/cds heterostructure nanocrystals," *Science*, vol. 330, no. 6009, pp. 1371–1374, 2010.

[100] E. Shafran, N. J. Borys, J. Huang, D. V. Talapin, and J. M. Lupton, "Indirect exciton formation due to inhibited carrier thermalization in single cdse/cds nanocrystals," *The Journal of Physical Chemistry Letters*, vol. 4, no. 4, pp. 691–697, 2013.

[101] C. She, G. W. Bryant, A. Demortière, E. V. Shevchenko, and M. Pelton, "Controlling the spatial location of photoexcited electrons in semiconductor cdse/cds core/shell nanorods," *Physical Review B*, vol. 87, no. 15, p. 155427, 2013.

[102] D. Polli, L. Luer, and G. Cerullo, "High-time-resolution pump-probe system with broadband detection for the study of time-domain vibrational dynamics," *Review of Scientific Instruments*, vol. 78, no. 10, pp. 103108–103108, 2007.

[103] F. Scotognella, K. Miszta, D. Dorfs, M. Zavelani-Rossi, R. Brescia, S. Marras, L. Manna, G. Lanzani, and F. Tassone, "Ultrafast exciton dynamics in colloidal cdse/cds octapod shaped nanocrystals," *The Journal of Physical Chemistry C*, vol. 115, no. 18, pp. 9005–9011, 2011.

[104] M. RosaáAntognazza *et al.*, "Steady-state photoinduced absorption of cdse/cds octapod shaped nanocrystals," *Physical Chemistry Chemical Physics*, vol. 13, no. 33, pp. 15326–15330, 2011.

[105] A. K. Rath, M. Bernechea, L. Martinez, F. P. G. de Arquer, J. Osmond, and G. Konstantatos, "Solution-processed inorganic bulk nanoheterojunctions and their application to solar cells," *Nature Photonics*, vol. 6, no. 8, pp. 529–534, 2012.

[106] Z. Wang, S. Qu, X. Zeng, J. Liu, F. Tan, L. Jin, and Z. Wang, "Influence of interface modification on the performance of polymer bi2s3 nanorods bulk heterojunction solar cells," *Applied Surface Science*, vol. 257, no. 2, pp. 423–428, 2010.

[107] G. Konstantatos, L. Martinez, A. Stavrinadis, S. Higuchi, S. L. Diedenhofen, M. Bernechea, and K. Tajima, "Hybrid solution-processed bulk heterojunction solar cells based on bismuth sulfide nanocrystals," *Physical Chemistry Chemical Physics*, 2013.

[108] Q. Guo, H. W. Hillhouse, and R. Agrawal, "Synthesis of cu2znsns4 nanocrystal ink and its use for solar cells," *Journal of the American Chemical Society*, vol. 131, no. 33, pp. 11672–11673, 2009.

[109] J. Puthussery, S. Seefeld, N. Berry, M. Gibbs, and M. Law, "Colloidal iron pyrite (fes2) nanocrystal inks for thin-film photovoltaics," *Journal of the American Chemical Society*, vol. 133, no. 4, pp. 716–719, 2010.

[110] Y. Wu, C. Wadia, W. Ma, B. Sadtler, and A. P. Alivisatos, "Synthesis and photovoltaic application of copper (i) sulfide nanocrystals," *Nano letters*, vol. 8, no. 8, pp. 2551–2555, 2008.

[111] C. Wadia, A. P. Alivisatos, and D. M. Kammen, "Materials availability expands the opportunity for large-scale photovoltaics deployment," *Environmental Science & Technology*, vol. 43, no. 6, pp. 2072–2077, 2009.

[112] J. Tang and A. P. Alivisatos, "Crystal splitting in the growth of bi2s3," *Nano letters*, vol. 6, no. 12, pp. 2701–2706, 2006.

[113] L. Cademartiri, R. Malakooti, P. G. O'Brien, A. Migliori, S. Petrov, N. P. Kherani, and G. A. Ozin, "Inside cover: Large-scale synthesis of ultrathin bi2s3 necklace nanowires (angew. chem. int. ed. 20/2008),"

Angewandte Chemie International Edition, vol. 47, no. 20, pp. 3652–3652, 2008.

[114] G. Konstantatos, L. Levina, J. Tang, and E. H. Sargent, "Sensitive solution-processed bi2s3 nanocrystalline photodetectors," *Nano letters*, vol. 8, no. 11, pp. 4002–4006, 2008.

[115] H.-C. Liao, M.-C. Wu, M.-H. Jao, C.-M. Chuang, Y.-F. Chen, and W.-F. Su, "Synthesis, optical and photovoltaic properties of bismuth sulfide nanorods," *CrystEngComm*, vol. 14, no. 10, pp. 3645–3652, 2012.

[116] C. E. Patrick and F. Giustino, "Structural and electronic properties of semiconductor-sensitized solar-cell interfaces," *Advanced Functional Materials*, vol. 21, no. 24, pp. 4663–4667, 2011.

[117] G. Xiao, Q. Dong, Y. Wang, Y. Sui, J. Ning, Z. Liu, W. Tian, B. Liu, G. Zou, and B. Zou, "One-step solution synthesis of bismuth sulfide (bi2s3) with various hierarchical architectures and their photoresponse properties," *RSC Advances*, vol. 2, no. 1, pp. 234–240, 2012.

[118] L. Shi, D. Gu, W. Li, L. Han, H. Wei, B. Tu, and R. Che, "Synthesis of monodispersed ultrafine bi2s3 nanocrystals," *Journal of Alloys and Compounds*, vol. 509, no. 38, pp. 9382–9386, 2011.

[119] M. IBANEZ, P. GUARDIA, A. SHAVER, D. CADAVID, J. ARBIOL, J. R. MORANTE, and A. CABOT, "Growth kinetics of asymmetric bi2s3 nanocrystals: Size distribution focusing in nanorods," *Journal of physical chemistry. C*, vol. 115, no. 16, pp. 7947–7955, 2011.

[120] J. S. Owen, J. Park, P.-E. Trudeau, and A. P. Alivisatos, "Reaction chemistry and ligand exchange at cadmium- selenide nanocrystal surfaces," *Journal of the American Chemical Society*, vol. 130, no. 37, pp. 12279–12281, 2008.

[121] S. Shen, Y. Zhang, L. Peng, B. Xu, Y. Du, M. Deng, H. Xu, and Q. Wang, "Generalized synthesis of metal sulfide nanocrystals from single-source precursors: size, shape and chemical composition control and their properties," *CrystEngComm*, vol. 13, no. 14, pp. 4572–4579, 2011.

[122] R. Malakooti, L. Cademartiri, Y. Akçakir, S. Petrov, A. Migliori, and G. A. Ozin, "Shape-controlled bi2s3 nanocrystals and their plasma polymerization into flexible films," *Advanced Materials*, vol. 18, no. 16, pp. 2189–2194, 2006.

[123] D. J. Riley, J. P. Waggett, and K. U. Wijayantha, "Colloidal bismuth sulfide nanoparticles: a photoelectrochemical study of the relationship between bandgap and particle size," *Journal of Materials Chemistry*, vol. 14, no. 4, pp. 704–708, 2004.

[124] V. I. Klimov, *Nanocrystal quantum dots*. CRC Press Boca Raton, FL, 2010.

[125] I. J. Kramer, L. Levina, R. Debnath, D. Zhitomirsky, and E. H. Sargent, "Solar cells using quantum funnels," *Nano letters*, vol. 11, no. 9, pp. 3701–3706, 2011.

[126] J. Tang, H. Liu, D. Zhitomirsky, S. Hoogland, X. Wang, M. Furukawa, L. Levina, and E. H. Sargent, "Quantum junction solar cells," *Nano letters*, vol. 12, no. 9, pp. 4889–4894, 2012.

[127] V. Calzia, G. Malloci, G. Bongiovanni, and A. Mattoni, "Electronic properties and quantum confinement in bi2s3 ribbon-like nanostructures," *The Journal of Physical Chemistry C*, vol. 117, no. 42, pp. 21923–21929, 2013.

[128] R. Caracas and X. Gonze, "First-principles study of the electronic properties of a2b3 minerals, with a= bi, sb and b= s, se," *Physics and chemistry of minerals*, vol. 32, no. 4, pp. 295–300, 2005.

[129] I. J. Kramer and E. H. Sargent, "Colloidal quantum dot photovoltaics: a path forward," *ACS nano*, vol. 5, no. 11, pp. 8506–8514, 2011.

[130] J. P. Clifford, G. Konstantatos, K. W. Johnston, S. Hoogland, L. Levina, and E. H. Sargent, "Fast, sensitive and spectrally tuneable colloidal-quantum-dot photodetectors," *Nature Nanotechnology*, vol. 4, no. 1, pp. 40–44, 2008.

[131] E. Sargent, "Solution-processed infrared optoelectronics: Photovoltaics, sensors, and sources," *Selected Topics in Quantum Electronics, IEEE Journal of*, vol. 14, no. 4, pp. 1223–1229, 2008.

[132] P. Nagpal and V. I. Klimov, "Role of mid-gap states in charge transport and photoconductivity in semiconductor nanocrystal films," *Nature communications*, vol. 2, p. 486, 2011.

[133] P. Stadler, B. R. Sutherland, Y. Ren, Z. Ning, A. Simchi, S. M. Thon, S. Hoogland, and E. H. Sargent, "Joint mapping of mobility and trap density in colloidal quantum dot solids," *ACS Nano*, 2013.

[134] P. Kambhampati, "Unraveling the structure and dynamics of excitons in semiconductor quantum dots," *Accounts of chemical research*, vol. 44, no. 1, pp. 1–13, 2010.

[135] J. I. Saari, E. A. Dias, D. Reifsnyder, M. M. Krause, B. R. Walsh, C. B. Murray, and P. Kambhampati, "Ultrafast electron trapping at the surface of semiconductor nanocrystals: Excitonic and biexcitonic processes," *The Journal of Physical Chemistry B*, vol. 117, no. 16, pp. 4412–4421, 2012.

[136] O. Voznyy, "Mobile surface traps in cdse nanocrystals with carboxylic acid ligands," *The Journal of Physical Chemistry C*, vol. 115, no. 32, pp. 15927–15932, 2011.

[137] O. Voznyy, D. Zhitomirsky, P. Stadler, Z. Ning, S. Hoogland, and E. H. Sargent, "A charge-orbital balance picture of doping in colloidal quantum dot solids," *ACS nano*, vol. 6, no. 9, pp. 8448–8455, 2012.

[138] R. Suarez, P. Nair, and P. V. Kamat, "Photoelectrochemical behavior of bi2s3 nanoclusters and nanostructured thin films," *Langmuir*, vol. 14, no. 12, pp. 3236–3241, 1998.

[139] A. Cantarero, J. Martinez-Pastor, A. Segura, and A. Chevy, "Excitonic absorption and urbach's tail in bismuth sulfide single crystals," *Applied Physics A*, vol. 45, no. 2, pp. 125–132, 1988.

[140] C. Murray, D. Norris, and M. G. Bawendi, "Synthesis and characterization of nearly monodisperse cde (e= sulfur, selenium, tellurium) semiconductor nanocrystallites," *Journal of the American Chemical Society*, vol. 115, no. 19, pp. 8706–8715, 1993.

[141] Y. Wang, A. Suna, W. Mahler, and R. Kasowski, "Pbs in polymers. from molecules to bulk solids," *The Journal of chemical physics*, vol. 87, p. 7315, 1987.

[142] A. Lipovskii, E. Kolobkova, V. Petrikov, I. Kang, A. Olkhovets, T. Krauss, M. Thomas, J. Silcox, F. Wise, Q. Shen, *et al.*, "Synthesis and characterization of pbse quantum dots in phosphate glass," *Applied physics letters*, vol. 71, no. 23, pp. 3406–3408, 1997.

[143] G. Pellegrini, G. Mattei, and P. Mazzoldi, "Finite depth square well model: Applicability and limitations," *Journal of applied physics*, vol. 97, no. 7, pp. 073706–073706, 2005.

[144] L. E. Brus, "Electron–electron and electron-hole interactions in small semiconductor crystallites: The size dependence of the lowest excited electronic state," *The Journal of chemical physics*, vol. 80, p. 4403, 1984.

[145] A. EFROS and A. EFROS, "Interband absorption of light in a semiconductor sphere," *SOVIET PHYSICS SEMICONDUCTORS-USSR*, vol. 16, no. 7, pp. 772–775, 1982.

[146] P. Larson, V. Greanya, W. Tonjes, R. Liu, S. Mahanti, and C. Olson, "Electronic structure of bi2x3(x= s, se, t) compounds: Comparison of

theoretical calculations with photoemission studies," *Physical review B*, vol. 65, no. 8, p. 085108, 2002.

[147] M. R. Filip, C. E. Patrick, and F. Giustino, "Gw quasiparticle band structures of stibnite, antimonselite, bismuthinite, and guanajuatite," *Physical Review B*, vol. 87, no. 20, p. 205125, 2013.

[148] G. Bongiovanni and J. Staehli, "Properties of the electron-hole plasma in gaas-(ga, al) as quantum wells: The influence of the finite well width," *Physical Review B*, vol. 39, no. 12, p. 8359, 1989.

[149] W. Ma, J. M. Luther, H. Zheng, Y. Wu, and A. P. Alivisatos, "Photovoltaic devices employing ternary pbs x se1-x nanocrystals," *Nano letters*, vol. 9, no. 4, pp. 1699–1703, 2009.

[150] D. Zhitomirsky, M. Furukawa, J. Tang, P. Stadler, S. Hoogland, O. Voznyy, H. Liu, and E. H. Sargent, "N-type colloidal-quantum-dot solids for photovoltaics," *Advanced Materials*, vol. 24, no. 46, pp. 6181–6185, 2012.

[151] A. H. Ip, S. M. Thon, S. Hoogland, O. Voznyy, D. Zhitomirsky, R. Debnath, L. Levina, L. R. Rollny, G. H. Carey, A. Fischer, *et al.*, "Hybrid passivated colloidal quantum dot solids," *Nature nanotechnology*, 2012.